2022-12-01

Impact Of Agricultural Practices On The Consumptive Water Use Of Irrigated Annual And Perennial Crops Of Northern Mexico And The U.s. Southwest.

Orlando Ramirez-Valle
University of Texas at El Paso

IMPACT OF AGRICULTURAL PRACTICES ON THE CONSUMPTIVE WATER USE OF IRRIGATED ANNUAL AND PERENNIAL CROPS OF NORTHERN MEXICO AND THE U.S. SOUTHWEST.

ORLANDO RAMIREZ-VALLE

Doctoral Program in Environmental Science and Engineering

APPROVED:

_____
Hugo A. Gutiérrez-Jurado Ph.D., Chair

_____
Alex Mayer Ph.D.

_____
Hernán A. Moreno Ph.D.

_____
Enrico A. Yépez-González Ph.D.

_____
Agustín Breña- Naranjo Ph.D.

_____
Stephen Crites, Ph. D.
Dean of Graduate School

IMPACT OF AGRICULTURAL PRACTICES ON THE CONSUMPTIVE WATER USE OF IRRIGATED ANNUAL AND PERENNIAL CROPS OF NORTHERN MEXICO AND THE U. S. SOUTHWEST.

by

Orlando Ramirez-Valle

THESIS

Present to the Faculty of the Graduate School of

The University of Texas at El Paso

in partial fulfillment

of the requirements

of the Degree of

DOCTOR OF PHILOSOPHY

Doctoral Program Environmental Science and Engineering

The University of Texas at El Paso

December 2022

Acknowledgments

This significant achievement in my academic preparation would not have been possible without the support of the following institutions: Instituto Nacional de Investigaciones Forestales, Agrícolas y Pecuarias (INIFAP), both Mexico's Consejo Nacional de Ciencia y Tecnología (CONACyT), and the University of Texas System for a CONTEX scholarship, and the National Science Foundation and the Critical Zone Network through the Drylands Critical Zone project. All of these institutions and programs provided me with the financial support and facilities to successfully carry out my research and complete my academic program. In addition, I want to express my gratitude to my advisor, Dr. Hugo A. Gutiérrez-Jurado, for guiding and encouraging me to develop skills for working on some of the most pressing environmental issues of drylands with repercussions in the productive sectors of social and economic importance. I also want to thank my committee members Dr. Enrico A. Yépez, Dr. Alex Mayer, Dr. Hernán Moreno, and Dr. Agustín Breña-Naranjo, for their valuable comments and continuous support during the development of this research. I also want to express my gratitude to Dr. Craig Tweedie and Dr. Lina Hamdan for her academic advice and support within the PhD ESE program, and the UTEP Department of Earth, Environmental & Resources Sciences (DEERS) staff (Dr. Annette Veilleux, Cynthia Salas Santoyo and Carlos Montana) for helping me navigate through the many bureaucratic procedures needed to carry out my research. Special thanks go to Dr. Jim Kubicki and the DEERS Scholarship Committee for providing me with financial assistance to complete my work. Also, I want to thank my family for their unconditional support and understanding during difficult times, in addition to thanking the friendship of those I met in this beautiful educational institution (class, laboratory and field partners); thank you for your valuable support.

Abstract

In drylands, crop water use varies considerably where high temperatures and limited water availability constraints farming activities, and irrigation planning is essential for the efficient water use and long-term sustainability of agriculture. However, despite dwindling water supplies and the looming threat of more frequent and intense droughts, low-efficient irrigation (e.g., furrow and flooding) continues to be the most widely used method for water delivery into agricultural parcels. Transitioning into more sustainable agriculture requires knowledge of the period of productive vs. unproductive crop water use during the agricultural cycle. I developed a method using satellite images for partitioning evapotranspiration (ET_a) into Evaporation (E_v) and Transpiration (T_r). The method was named Partitioning of Evapotranspiration Through Vegetation Index (PETVI). I verified the E_v and T_r estimates with independently measured ET_a using Eddy Covariance (EC_{ET}), satellite-derived ET from the METRIC algorithm, point measurements of Ev using the Maximum Entropy Production (MEP) method, and Ev and Tr obtained from EC_{ET} using the underlying Water Use Efficiency (uWUE) method. We tested this approach on an experimental wheat plot in Mexico. Once I had validated PETVI, I used it in an agricultural valley located in Cuauhtémoc, Chihuahua, in a cornfield under three irrigation schemes (furrow, sprinkler, and drip), I also used PETVI in a pecan orchard located in the south of Texas to quantify the productive and unproductive water use. In all cases unproductive water use by the crops occur in the early season, due to a long-time interval between the first irrigation and the planting or resprouting of the crops. Because groundwater supplies early season irrigation, shortening the time between the first irrigation and planting or resprouting would decrease the total consumptive water use in these crops.

Table of Contents

Acknowledgments iii

Abstract iv

1 Chapter 1. Introduction 1

2 Chapter 2. Assessing the productive (Transpiration) and unproductive (Evaporation) consumptive water use in agriculture by Partitioning Evapotranspiration Through Vegetation Indices (PETVI) 6

2.1 Introduction 6

2.2 Materials and Methods 8

2.2.1 Study site 8

2.2.2 Data and Methods 10

2.2.3 Meteorological data 10

2.2.4 Eddy Covariance Evapotranspiration measurement (EC) 11

2.2.5 Remote sensing data 12

2.2.6 Sentinel-2 data pre-processing 13

2.2.7 METRIC data 15

2.2.8 Multispectral high spatial resolution images from Unmanned Aerial Vehicle Surveys 16

2.2.9 Development of the Partitioning Evapotranspiration through Vegetation Indices algorithm (PETVI) 17

2.2.10 Transpiration using Basal crop Coefficient (K_{cb}) and Vegetation Fraction (F_c) 20

2.2.11 Evapotranspiration from METRIC. 23

2.2.12 Reference evapotranspiration 24

2.2.13 Partitioning Evapotranspiration 24

2.2.14 Evapotranspiration from the Maximum Entropy Production Model (MEP-ET) 25

2.2.15 Underlying Water Use Efficiency (*uWUE*) model 26

2.3 Results 27

2.3.1 Climatology 27

2.3.2 Dynamics of Evapotranspiration during the growing cycle. 28

2.3.3 Performance of Evapotranspiration Models 30

2.3.4 Evapotranspiration from Eddy covariance (ET_{EC}), Evapotranspiration from METRIC algorithm (ET_M). 30

2.3.5 Performance of Transpiration models. 32

2.3.6 Transpiration from uWUE as reference method.....32

2.3.7 Performance of Transpiration from PETVI and ET_{EC} - Ev_{MEP} 33

2.3.8 Performance of PETVI transpiration using high-resolution images ($T_{r\ PETVI(HR)}$)...35

2.3.9 Evaporation.....38

2.3.10 Evaporation MEP (E_v-*MEP*) & Evaporation PETVI (E_v-*PETVI*) 38

2.3.11 Spatial analysis of the evaporation and transpiration dynamics with high and moderate spatial resolution imagery.....42

2.3.12 Evaporation and Transpiration using *PETVI* method and high-resolution UAV imagery. 42

2.3.13 Evaporation and Transpiration using PETVI method and Sentinel 2 images. 43

2.3.14 Water balance at the plot scale 48

2.4 Discussion 51

2.4.1 PETVI depends on the vegetation index 51

2.4.2 Partitioning of water flux using two digital products Sentinel 2 and UAV images 52

2.4.3 Crop water use changes at different phenological stages 53

2.4.4 Environmental conditions and dynamics of water transfer and soil moisture....54

2.4.5 PETVI Soil Evaporation 56

2.4.6 Utility of PETVI method 57

2.4.7 Tracking the water balance during the agricultural cycle....58

2.5 Conclusion 60

2.6 References 62

3 Chapter 3. Assessment of Irrigation Efficiencies of An Agricultural Valley with An Over-Exploited Aquifer Using the PETVI Method. 77

3.1 Introduction 77

3.1.1 Background and historical evolution of water resources in the Cuauhtémoc valley 80

3.2 Materials and Methods 83

3.2.1 Study site 83

3.2.2 Data 85

3.2.3 Meteorological data 85

3.2.4 Remote sensing data 85

3.2.5 Sentinel-2 data 86

3.2.6 METRIC data 88

3.2.7 Methods 89

3.2.8 Crop coefficient and basal crop coefficient. 89

3.2.9 Basal crop coefficient (K_{cb}) from NDVI and transpiration (T_r) 91

3.2.10 Reference evapotranspiration (ET0) 93

3.2.11 Evapotranspiration from METRIC 94

3.2.12 Partitioning Evapotranspiration 95

3.3 Results 96

3.3.1 Dynamics of Evapotranspiration (ET_a) during the growing cycle in furrow-irrigated fields. 96

3.3.2 Dynamics of Evapotranspiration (ET_a) during the growing cycle in sprinkler-irrigated fields. 98

3.3.3 Dynamics of Evapotranspiration (ET_a) during the growing cycle in drip-irrigated fields. 100

3.3.4 Relative contribution of the Evaporation (E_v) component into total Evapotranspiration (ET_a). 102

3.3.5 Impact of agricultural practices at the basin level 103

3.3.6 The behavior of soil evaporation during the interval between pre-sowing irrigation and sowing date in the six observation plots 107

3.3.7 Impact of irrigation operation on water balance at parcel scale 108

3.4 Discussion 111

3.4.1 Comparison of the observed efficiencies in three irrigation systems. 111

3.4.2 Effect on the different types of irrigation in the partition of the water balance. ... 113

3.4.3 Non-productive water use (beginning or end of the agricultural cycle) 114

3.4.4 Impact of agricultural practices on water use at the basin-scale (potential savings) 117

3.5 Conclusion 120

3.6 References 122

4 Chapter 4. Quantifying productive vs. unproductive water use in a pecan orchard under flood irrigation and different soil textures 131

4.1 Introduction 131

4.2 Materials and Methods 135

4.2.1 Study site 135

4.2.2 Data 137

4.2.3 Remote sensing data 137

4.2.4 METRIC data: 137

4.2.5 Sentinel-2 (S-2) images 138

4.2.6 Reference evapotranspiration ET_0 from (gridMET). 138

4.2.7 Lidar cloud points 138

4.3 Methods 139

4.3.1 Vegetation fraction (*Fv*) 140

4.3.2 Transpiration using Basal crop Coefficient (K_{cb}) 141

4.3.3 Evapotranspiration from METRIC. 142

4.3.4 Partitioning Evapotranspiration 144

4.4 Results 145

4.4.1 Evapotranspiration dynamics during the agricultural cycle 145

4.4.2 Evolution of the water balance components in the orchard during the growing season. 149

4.4.3 Analysis of canopy height and soil texture distribution. 152

4.4.4 Effect of soil texture on transpiration dynamics during the agricultural cycle. 154

4.4.5 Effect of soil texture on evaporation dynamics during the agricultural cycle. 157

4.5 Discussion 159

4.5.1 Dynamics of evapotranspiration during the agricultural cycle. 159

4.5.2 Productive and unproductive water use during different stages of the agricultural cycle. 160

4.5.3 Effect of soil texture on partitioning ET fluxes of a pecan orchard. 161

4.5.4 Implications of the information on the productive and unproductive use of water for sustainable management of an orchard with two water sources. 163

4.6 Conclusion 164

4.7 References 166

Chapter 5. Conclusion 175

5 Appendix 180

6 Vita 181

List of Tables

Table 2.1 Images selected from S-2 with their main characteristics; Granule ID, sensing date, and clouds cover percentage. 14

Table 2.2 Images selected from Landsat 7 and 8 with their main characteristics Granule ID, sensing date, and clouds cover percentage. 15

Table 2.3 I Average daily transpiration (T_r) at each phenological stage in mm day^{-1}……..…55

Table 3.1 Characteristics of S-2 Images processed on GEE 86

Table 3.2 Characteristics of Landsat images processed on GEE 88

List of Figures

Figure 2.1) Location of the study area in northwestern Mexico, the study site represented by a blue dot, b) Aerial image of the Experimental parcel showing the location of the Eddy Covariance system (EC) denoted by the red star with its footprint (reddish oval)and the location of 5 soil moisture sensors (blue dots) 30 cm depth distributed within the footprint of the EC. 10

Figure 2.2 Representation of the phenological evolution of the crop and its corresponding crop coefficient represented by a solid black line (K_c) throughout the growing season as comprised of basal crop coefficient (K_{cb}) green solid line, and the soil crop coefficient (K_e) yellow dashed line. 19

Figure 2.3 Flow diagram for estimating the evapotranspiration partitioning on productive water (Tr) versus unproductive water (Ev) through the partitioning evapotranspiration through vegetation index (PETVI) method. The input variables shown in yellow (from top to bottom) are S-2 images with a temporal resolution of 5 days and spatial resolution of 10 m., Meteorological data from the weather stations, and evapotranspiration (ET_a) images from the METRIC algorithm. The blue squares show the calculation of the complementary variables to partition evapotranspiration (ET_a). The green squares show the last step of the calculations; transpiration (T_r) is calculated as the product of the K_{cb} times ET_0, and K_c times ET_0 to calculate ET_a. Evaporation (Ev) is the residual between ET_a end T_r. 20

Figure 2.4 Environmental conditions during the observation period from February 2 to April 9, 2019. In panel a), the orange line indicates the daily average air temperature, and the dashed blue line denotes the vapor pressure deficit (VPD). The black line in panel b) represents the net radiation (Rn). Panel c) represents the wind speed. The blue bars in panel d) represent precipitation

in mm dia^{-1}, and the red line denotes Evapotranspiration (ET, mm dia^{-1}) measured by the Eddy covariance system.....28

Figure 2.5 a) Phenological stages of wheat in the study area: (S) sowing, (Fi) flowering initiation, (Ts) Terminal spikelet, (Fn) First node, (H) Heading, (An) Anthesis, and (Pm), Physiological maturity; b) Evolution of NDVI during the agricultural cycle (black line); c) Evapotranspiration (ET) and transpiration (T_r) time series calculated using observation data and different methods: T_{rPETVI} (blue line), ET_{METRIC} (red dashed line), ET_{MEP} (green line), ET_{EC} (purple line) $T_{r\ uWUE}$ (black dashed line). Black arrows pointing up show times of irrigation events) 30

Figure 2.6 a) Time series of ET from the EC system (solid line), and the METRIC method (dotted line); b) scatter diagram comparing the measured (ET_{EC}) and estimated (ET_{METRIC}) evapotranspiration in the experimental plot; the red line shows the slope of the function, the dotted line shows the 1:1 relation of the linear regression. 31

Figure 2.7 The 95th quantile regression using the half-hourly growing season data (between February 2 and 20) for our site to estimate uWUEp and b) the linear regression using half-hourly data for March 21 to estimate uWUEa for this day. The uWUa/uWUEp determines the T/ET ratio. The intercept was set to zero for both quantile and linear regressions.....33

Figure 2.8 a) Transpiration time series obtained with the underlying water use efficiency method (uWUE; blue line), as residual from Eddy covariance Evapotranspiration and soil evaporation calculated with Maximum Entropy Production (ET_{EC} - Ev_{MEP}; red dashed line), and with the PETVI method ($T_{r\ PETVI}$; yellow line); b) Scatter plot of the transpiration calculated with the uWUE method (x-axis) and $T_{r\ PETVI}$ and Tr ET_{EC}-Ev_{MEP} (y-axis); c) Taylor diagram displaying the correlation coefficient, standard deviation and root means square difference between the modeled transpirations (Tr ET_{EC}-Ev_{MEP} (red circle) and $T_{r\ PETVI}$ (blue diamond)) and the reference

transpiration ($T_{r\,uWUE}$ (black circle)); green dashed lines represent the root mean square difference (RMSD) in mm.....35
Figure 2.9 a) transpiration time series calculated with the underlying water use efficiency (uWUE; blue line) method, as residual from Evapotranspiration from Eddy covariance system and soil evaporation from the Maximum Entropy Production method ($T_r = ET_{EC}$-Ev_{MEP}; r red dashed line), and with the proposed PETVI method using S-2 images ($T_{r\ PETVI}$; yellow line), and high spatial resolution images ($T_{r\ PETVI(HR)}$; purple line); b) scatter plot comparing $T_{r\,PETVI}$ (blue diamond), $T_{r\ PETVI(HR)}$ (cyan squares), and Tr ET_{EC}-Ev_{MEP} (red circles) versus reference data from the uWUE model; c) taylor diagram displaying the correlation coefficient, standard deviation and root mean square difference between the modeled transpirations (T_r ET_{EC}-Ev_{MEP} (red circle), $T_{r\ PETVI}$ (blue diamond), $T_{r\ PETVI(HR)}$ (cyan squares)) and the reference transpiration ($T_{r\,uWUE}$ (black circle)); green dashed lines represent the root mean square difference (RMSD) in mm.....37
Figure 2.10 a) Soil evaporation time series calculated with the uWUE method (blue line), as the residual of the Evapotranspiration from the METRIC algorithm (ET_M) and transpiration through the PETVI method (T_{rPETVI}; dashed red line), and from the Maximum entropy pro production model (Ev_{MEP}; yellow line); b) scatter plot of the reference evaporation obtained from the uWUE against the evaporation calculated with the Ev-MEP (red circles), and the Ev_{PETVI} (blue diamond); c) Taylor diagram displaying the correlation coefficient, standard deviation and root mean square difference between the modeled evaporations (Ev ET_{EC}-Tr_{MEP} (red circle), Ev $_{PETVI}$ (blue diamond), and the reference evaporation (Ev $_{uWUE}$ (black circle)); green dashed lines represent the root mean square difference (RMSD) in mm. 39
Figure 2.11 a) Soil evaporation time series calculated with underlying water use efficiency (uWUE; blue line) as residual from Evapotranspiration from Eddy covariance system and

transpiration using uWUE, and soil evaporation with the proposed PETVI method using S-2images (red dashed line), and Ev-$_{MEP}$ (yellow line), and high spatial resolution images Ev $_{PETVI(HR)}$ b) scatter plot comparing Ev$_{PETVI}$ (blue diamond), EvMEP (red circles), Ev $_{PETVI(HR)}$ (cyan squares), versus reference data from the uWUE model; c) Taylor diagram displaying the correlation coefficient, standard deviation, and root mean square difference between the modeled evaporation (Ev$_{PETVI}$ ET$_{EC}$-Tr$_{PETVI}$ (blue diamond), Ev$_{MEP}$ (red circle), Ev $_{PETVI(HR)}$ (cyan squares)) and the reference evaporation (Ev $_{uWUE}$ (black circle)); green dashed lines represent the root mean square difference (RMSD) in mm.....41

Figure 2.12 Spatial distribution of evaporation (Ev) in mm day-1 as a residual of ET$_{EC}$ - $_{Tr\ PETVI(HR)}$; transpiration (Tr) in mm day^{-1}, and the probability density functions (PDFs) for Ev and T$_r$ for a) February 15, 2019; b) February 23, 2019; c) March 02, 2019; d) March 15, 2019; e) March 23, 2019; and f) March 28, 2019. 43

Figure 2.13 Spatial analysis of Ev as a residual of ET$_{METRIC}$ - T$_{rPETVI}$ using S-2 images with spatial resolution of 10 m per pixel for 6 dates within the observation period (panels a to d). Subpanels 1,2 and 3 show the spatial patterns on Ev, T$_r$ and their probability density functions (PDFs) within the experimental plot respectively. Subpanels 1,2, and 3 show the spatial patterns on Ev, T$_r$ and their probability density functions (PDFs) within the experimental plot respectively.....45

Figure 2.14 Effects of spatial resolution (5 cm per pixel and 10 m per pixel) on Ev and T$_r$ (in mm day- 1) calculated from PETVI; a) and b) show UAV derived images from March 23, 2019 and March 28, 2019 respectively; c) and d) show S-2 derived images on March 23, 2019 and March 28, 2019, respectively. Subpanels 1,2, and 3 show the spatial patterns on E$_v$, T$_r$ and their probability density functions (PDFs) within the experimental plot respectively.....47

Figure 2.15 a) Temporal dynamics of Evapotranspiration (ETa) from METRIC (dashed red line) and Transpiration (Tr) from PETVI (blue line); b) water inputs at the experimental site showing irrigation (blue bars) and rainfall events (red bars); c) cumulative Evaporation (Ev, red line) and Transpiration (T_r, green line); d) time series of the surface water balance (inputs - outputs); e) dynamics of soil moisture content (red line) during the observation period where the dashed black line indicates the absence of data before and after the observation period; f) proportion of rainfall and irrigation on the plot; g) proportion of T_r, Ev and runoff or percolation on the plot.....50
Figure 3.1 Conceptual model (not to scale) of the Cuauhtémoc aquifer recharge rate, pumping, and phreatic levels evolution versus the drilling and pumping costs from the beginning of the agriculture activity in the basin (periods 1-3), the actual situation (period 3) and a hypothetical and desirable sustainable future (periods 4 and 5). 82
Figure 3.2 a) Show the state of Chihuahua Mexico; b) General view of the Bustillos Lagun Basin delimited by mountains represented by the black line forming a closed basin with its central part forming a large valley. The agricultural plots are shown in a light green color within the basin, making up ~ 80% of the basin's surface. The observation plots distributed in the farming valley are shown. The parcels were labeled as F-1, F- 2 for furrow irrigation, represented by small yellow squares; S-1, S-2 for sprinkler irrigation sites, represented by yellow; and D-1, D-2 for drip irrigation sites, represented by red triangles, standard weather stations are represented by black triangles. White dots represent the main population centers. In addition, three bodies of water are displayed, one in the north, one in the south, and a larger one that serves important ecological needs called the Laguna de Bustillos in the southwestern part of the basin that has following dimensions: 16 km long and 8 km wide at its maximum capacity.....84

Figure 3.3 shows the scheme of the crop coefficient curve (K_c), represented by the black line; the evaporation coefficient curve (K_e), represented by the yellow dashed line. Moreover, the green line represents the basal crop coefficient curve (K_{cb}); the vertical dashed lines represent the crop growth stages 91

Figure 3.4 workflow to estimate the variables needed in the PETVI method. This workflow diagram shows the input variables from left to right with yellow squares. Here are the required S-2 images, meteorological data, and ET_a images from Landsat using METRIC algorithms. In the center of the flow diagram are the basic calculations and procedures. Finally, in the green boxes are represented the results at the daily scale of T_r, ET_a, and last but not less significantly, the evaporation as residual from the subtraction of the T_r of ET_a. 95

Figure 3.5 Hydrological fluxes in observation parcels with furrow irrigation system for sites F-1 and F-2. (a, e) showing the behavior of Evapotranspiration [ET mm d^{-1}; orange line], and Transpiration [T mm d-1; blue line]. Soil evaporation is shown as a shaded orange region. The black dashed line shows the basal crop coefficient; (b, f) show the main water inputs to the parcel; effective rainfall [mm; orange bars], and irrigation events [mm; blue bars]; (c, g) show the cumulative Transpiration [mm; blue line] and Evaporation [mm; orange line], the dashed horizontal lines indicate the absence of analysis at the end of the cycle; (d, h) show the surface water balance (P-ET [mm]) at the plot scale, the dashed line indicates the absence of analysis in the final of the period and the dashed vertical lines in orange show the planting and harvest dates. 97

Figure 3.6 Hydrological fluxes in observation parcels with sprinkler irrigation systems for sites S-1 and S-2. (a, e) showing the behavior of Evapotranspiration [ET mm d^{-1}; orange line], and Transpiration [T mm d^{-1}; blue line]. Soil evaporation is shown as a shaded orange region. The

black dashed line shows the basal crop coefficient; (b, f) show the main water inputs to the parcel; effective rainfall [mm; orange bars], and irrigation events [mm; blue bars]; (c, g) show the cumulative Transpiration [mm; blue line] and Evaporation [mm; orange line], the dashed horizontal lines indicate the absence of analysis at the end of the cycle; (d, h) show the surface water balance (P-ET [mm]) at the plot scale, the dashed line indicates the absence of analysis in the final of the period and the dashed vertical lines in orange show the planting and harvest dates. 99

Figure 3.7 Hydrological fluxes in observation parcels with drip irrigation systems for sites D-1 and D-2. (a, e) showing the behavior of Evapotranspiration [ET mm d^{-1}; orange line], and Transpiration [T mm d^{-1}; blue line]. Soil evaporation is shown as a shaded orange region. The black dashed line shows the basal crop coefficient; (b, f) show the main water inputs to the parcel; effective rainfall [mm; orange bars], and irrigation events [mm; blue bars]; (c, g) show the cumulative Transpiration [mm; blue line] and Evaporation [mm; orange line], the dashed horizontal lines indicate the absence of analysis at the end of the cycle; (d, h) show the surface water balance (P-ET [mm]) at the plot scale, the dashed line indicates the absence of analysis in the final of the period and the dashed vertical lines in orange show the planting and harvest dates.....101

Figure 3.8 Evaporation ratio (E_v/ET) displaying the contribution of soil evaporation (E_v) to the total Evapotranspiration (ET). a) and b) show the E_v/ET in the sites with furrow irrigation (F-1 and F-2); c) and d) show the E_v/ET relationship in the parcel with sprinkler irrigation systems (S-1 and S-2); e) and f) show the E_v/ET in the parcels using drip irrigation. The blue line shows the evolution of E_v/ET during the observation period. The light orange shaded area shows the period when groundwater was used for irrigation, and the blue-shaded regions shows the period when water came from rainfall. 103

Figure 3.9 Extrapolation analysis of the impact of the agricultural practices at basin scale; a) average behavior of the furrow irrigation based on F-1, and F-2; b) average behavior of the sprinkler irrigation based on S-1 and S-2; c) average behavior of drip irrigation based on D-1 and D-2. In all panels the two bars on the left show the average values considering current operation efficiencies, while the right-side bars show the theoretical water use considering the maximum theoretical efficiency for those irrigation systems.....106
Figure 3.10 Cumulative soil evaporation and the period between pre-sowing irrigation and the sowing date for: sprinkler irrigated parcels S-1 (black dashed line) and S-2 (black line); furrow irrigated parcels F-1 (red dashed line) and F-2 (red line); drip irrigated parcels D-1 (blue dashed line) and D-2 (blue line). Bottom, middle, and top points on each line represent 25, 50, and 75 % of the cumulative soil evaporation. 108
Figure 3.11Water balance in the observation plots. a) main water inputs (red color is rainwater and blue is groundwater); b) water input proportion (in %) of rainwater and groundwater; c) use of water by the transpiration component; d) outflow of water from the system due to soil evaporation (light orange), evaporation of rainwater intercepted by the canopy (yellow), and evaporation of irrigation water intercepted by the canopy (purple color); e) runoff or percolation; f) proportion of water outputs (in %) by each component. 110
Figure 3.12 Water management scenarios at the basin scale; a) average of current water management; b) potential savings with irrigation systems operating at theoretical efficiencies; c) potential savings by reducing time intervals between pre-sowing irrigation and planting date..120
Figure 4.1 General location of the experimental site; a) Texas State highlighting the Rio Grande (blue line) and the experimental site (red dot); b) experimental plot (red square) and location of a piezometer (yellow dot) and two sample areas representative of fine soil textures (PF; orange

square) and coarse soil textures (PC; green square). The blue line shows the location of the Rio Grande River 900 m south of the center of the orchard. 136
Figure 4.2 General shape of the crop coefficient (K_c) in a pecan orchard represented by a black line; the orange dashed line shows the hypothetical trajectory of the evaporation coefficient (K_e), and the green line characterizes the basal crop coefficient (K_{cb}). The vertical dashed lines delimit the main crop growth stages. 140
Figure 4.3 Diagram to estimate the variables needed in the PETVI method. This workflow diagram shows the input variables from left to right with yellow squares. Here are the required S-2 images, meteorological data, and ET_a images from Landsat using METRIC algorithms. In the center of the flow diagram are the basic calculations and procedures. Finally, in the green boxes are represented the results at the daily scale of T_r, ET_a, and last but not less significantly, the evaporation as residual from the subtraction of the T_r of ET_a. 144
Figure 4.4 a), b), and c) time series of the mean evapotranspiration (ET_a), transpiration (T_r) and soil evaporation (E_v) for the orchard (WP), the coarse grained soil area (PC) and the fine grained soil area (PF) respectively; shaded red and blue lines show the variability of the ET_a and T_r respectively with +/- one standard deviation; d) shows the water inputs to the orchard from irrigation events (blue bars) and rainfall events (red bars); e, f, g) show the cumulative E_v (red) and cumulative T_r (blue) for WP, PC and PF respectively; h) time series of the surface water balance (SWC); i) proportion of water inputs as percentage of irrigation (blue) and rainfall (red); and j, k, l) proportion of water output components (T_r in blue, Storage in yellow and E_v in red) in percentage for the WP, PC and PF respectively. 148
Figure 4.5 Water balance components in between irrigation events; a) water inputs from irrigation (blue bars), and rainfall (red bars); b), c) and d) show the averages of transpiration (T_r) evaporation

(Ev) and (ΔS) respectively, for the whole orchard (WP; dark green), the Pecan Coarse area (PC; light green), and the Pecan Fine area (PF; yellow). 151

Figure 4.6 Spatial distribution of LiDAR-derived canopy height (CH) for each tree in the Pecan Orchard; black arrows depict the transects of the profiles showing the variability in CH from P1 to P5 in (b); areas of fine texture soil are shown in gray color; CH varies from 0 (white) to 11.3 m (green); b) Canopy height distribution across each profile (P1 to P5) increasing in distance from north to south; c) box plots showing the distribution of CH values for each profile and separated by soil texture where PF is fine texture soil, and PC is coarse texture soil. 153

Figure 4.7 Transpiration (T_r) spatial patterns in the orchard for periods in between irrigation events and their probability density functions (PDF) for the coarse textured (PC; pink shaded), and fine textured (PF; blue shaded) soils. 156

Figure 4.8 Evaporation (E_v) spatial pattern in the orchard for periods in between irrigation events and their probability density functions (PDF) for the coarse textured (PC; pink shaded), and fine textured (PF; blue shaded) soils. 158

Figure 5.1 Transpiration (Tr) time series obtained with the underlying water use efficiency method (uWUE; blue line); red line represent the Tr calculated using NDVI, transpiration calculated using EVI, and the Tr using MSAVI; b) Scatter plot of the transpiration calculated with the uWUE method (x-axis) and $T_{r\ NDVI}$, $T_{r\ EVI}$ and $T_{r\ MSAVI}$ (y-axis); c) Taylor diagram displaying the correlation coefficient, standard deviation and root means square difference between the modeled transpirations ($T_{r\ NDVI}$ (blue diamond), $T_{r\ EVI}$ (red circle) and $T_{r\ MSAVI}$ (green square)) and the reference transpiration ($T_{r\ uWUE}$ (black circle)); green dashed lines represent the root mean square difference (RMSD) in mm.....180

Chapter 1. Introduction

In arid and semiarid regions, comprising nearly 30% of the land in the world, water scarcity, and highly inefficient agricultural irrigation practices represent significant obstacles for achieving sustainable food production systems (Wang et al., 2007; Ma et al., 2021). Naturally, drylands are susceptible to large climatic fluctuations and sustained high temperatures for extended periods. Those conditions drive high evapotranspiration rates and make crops highly sensitive to slight environmental changes (Krol et al., 2007). It is well documented that arid and semi-arid regions frequently experience years of below-average rainfall and continuous and severe droughts (Bhering et al., 2021). These naturally occurring phenomena directly impact the agricultural industry and other water-using sectors resulting in multiple social and environmental challenges (Perry, 2011; Huang et al., 2021). In addition, multiple factors such as population growth, land-use changes, agricultural and urban expansion, and overexploitation of surface and groundwater reservoirs driven by a warming climate and recurrent drought spells are compromising the sustainability of dryland food production (Zhang et al., 2017).

The circumstances above described, have steadily risen water demands, while water reservoirs continue to dwindle, threatening the long-term social and economic viability of populated drylands worldwide. Therefore, arid and semi-arid areas of the world are facing more complex problems than ever in accessing freshwater (Fallatah et al., 2019), and pervasive, highly inefficient irrigation practices in agriculture are putting further stress on freshwater supplies. For instance, in intensive dryland agriculture, irrigation using water from reservoirs is essential for maintaining productivity (Portmann et al., 2010; Biemans et al., 2011). However, this agricultural practices are subject to the sizeable hydrological variability that prevails in arid and semi-arid areas

(i.e irrigation depleting groundwater). Groundwater in these locations is a limited resource, and in many instances, at current extraction and recharge rates, it has turned into a non-renewable water source (Bierkens & Wada, 2019). Despite its limited or non-renewable nature, groundwater has played an essential role in transforming vast arid ecosystems into prosperous croplands (Turner et al., 2019). Indeed, global agriculture has been labeled as the largest user of groundwater, with about ~70% of global water consumption (Rost et al., 2008; Wallace, 2000).

Consequently, agriculture is considered the major contributor to the decrease in this water source (Lan et al., 2021). For example, recent studies on the footprint of large aquifers found that northwestern Mexico, the United States High Plains, North Arabia, the Persian, Upper Ganges, and North China plains' aquifers are in a condition of generalized stress (Gleeson et al., 2012). In all these areas, aquifer stress is mainly attributed to groundwater use by agricultural production, while other socio-economic sectors, including urban water supply and industry, are increasingly competing for that water (de Frutos Cachorro et al., 2021). Considering that about 50% of the world's population currently depends on groundwater to meet its drinking water needs (Kumar et al., 2020), competition for this resource is expected to continue growing between all sectors (Huang et al., 2021).

Globally, water depletion rates doubled during the 1960 to 2000 period, particularly in areas with intensive agricultural production (Wada et al., 2010). Because arid and semiarid areas are prone to experience severe and prolonged droughts, the use of groundwater to supplement or replace surface water irrigation in agricultural activities will continue to grow, and with it, the decline of water availability and quality in aquifers (Famiglietti & Rodell, 2013). For these reasons, there is an urgent need to improve water use efficiency in these regions, which inevitably involves improving irrigation practices in agriculture. In advanced economies and countries with strong

support for the modernization of agricultural practices, switching from furrow to sprinkler or drip irrigation can improve the water use efficiency of agricultural activities. However, in developing countries, changing irrigation techniques requires significant economic investments that are not within reach of most farmers and governments. The above is one of the biggest obstacles to sustainable food production systems in developing countries, particularly in semi-arid regions, where it can lead to the abandonment of croplands and food shortages (António dos Anjos & Cabral, 2021).

In Mexico, large portions of the territory on the north and central high plains are susceptible to frequent and intense droughts due to their location between both the Sierra Madre Oriental and Sierra Madre Occidental Mountain ranges, creating a rain-shadow effect from moisture influxes of the Gulf of Mexico and the Pacific Ocean respectively (Roy et al., 2021). For that reason, surface water reservoirs dwindle during meteorological droughts, and groundwater extraction is used to compensate for the surface water deficit (Magaña et al., 2021). Mexico has 60% of the territory in semiarid environments (Montecillo-Cedillo., 2016). Thus, intensive agricultural activities in these locations frequently resort to groundwater sources for irrigating crops. This has triggered an urgent and severe problem of aquifer overexploitation throughout most groundwater basins in northern Mexico. Overexploitation of an aquifer occurs when water extraction rates exceed those of the natural and/or induced recharge. Many areas of Mexico's arid north and central High Plains are experiencing sustained overexploitation of aquifers on which large urban centers rely for their water supply (Arreguín et al., 2010). For instance, in 2018, Mexico's National Water Commission (CONAGUA) reported that 72 of the 106 overexploited aquifers in Mexico are located in the north and high plains (CONAGUA, 2011). This represents an urgent concern because 50.6 % of the

water used in the country comes from overexploited aquifers, where agriculture is the primary water user (CONAGUA, 2011).

Considering all the issues described above, improving water use in agricultural practices is urgently needed. To do this, a better understanding of the periods in which water delivered to the crops is used productively, would inform . When is the water delivered to crops being used by the plants and when and how much is being lost to the atmosphere? These are the questions that constitute the core of the motivation for the studies conducted in this dissertation. The works contained in this document are organized as follows: in Chapter 2, I describe a method developed to partition evapotranspiration (ET_a) of well-watered crops into its two components: evaporation (E_v) and transpiration (T_r). The work was carried out in an experimental plot located in northwest Mexico, where winter wheat was grown and fed with flood irrigation. The experimental plot was instrumented with meteorological and soil moisture sensors, and an Eddy Covariance station to measure gas exchanges between the crop and the atmosphere. The method developed uses vegetation indices and satellite-derived ET_a values from the *LandSat* platform. The method was named ***Partitioning of Evapotranspiration Through Vegetation Index*** (PETVI) and was tested and validated with independent measurements of ET, E_v and T_r. After building confidence in the resulting T_r and E_v data produced, various analyses of the crop water balance and water usage were performed to evaluate its water use efficiency and the effect of spatial resolution of the input data on the correct estimation of those variables. In Chapter 3, I used the PETVI method to evaluate the water use efficiencies of different irrigation schemes (furrow, sprinkler, and drip) in an agricultural valley in northern Mexico with maize production that relies for its water supplies on an overexploited aquifer. For this chapter, I redefined the concept of water use efficiency to consider only the productive water use based on the relationship between the transpiration of the

crop and the total water delivered to the plot. I then used the PETVI method to evaluate the periods in which productive and unproductive water use occurs and how current agricultural practices have an impact on the total consumptive water use in the agricultural valley. In Chapter 4, I used the PETVI method in a pecan orchard in west Texas, to investigate the impacts of the properties of the soil, tree canopy development, and flood irrigation on the productive and unproductive water use of the orchard, following the seasonal dynamics of soil evaporation and tree transpiration after each irrigation event. A final fifth chapter offers a synthesis of the main findings of these works while addressing future work to improve the method's performance and its application under different scenarios and spatial scales.

Chapter 2. Assessing the productive (Transpiration) and unproductive (Evaporation) consumptive water use in agriculture by Partitioning Evapotranspiration Through Vegetation Indices (PETVI)

2.1 Introduction

In arid and semiarid regions, comprising nearly 30% of the land in the world, water scarcity, and highly inefficient agricultural irrigation practices represent major obstacles for achieving sustainable food production systems (Wang et al., 2007; Ma et al., 2021). Naturally, drylands are susceptible to large climatic fluctuations and sustained high temperatures for extended periods of time. Those conditions drive high potential evapotranspiration rates and make crops highly sensitive to slight environmental changes (Krol et al., 2007). It is well documented that arid and semi-arid regions frequently experience years of below-average rainfall and continuous and severe droughts (Bhering et al., 2021). In those regions, these naturally occurring phenomena directly impact the agricultural industry together with all other water-using sectors resulting in multiple social and environmental challenges (Perry, 2011; Huang et al., 2021). Furthermore, other factors such as population growth, land-use changes, agricultural and urban expansion, and overexploitation of surface and groundwater reservoirs driven by a warming climate and recurrent drought spells, are compromising the sustainability of dryland food production (Zhang et al., 2017).

Under these scenarios, there is an urgent need to promote water conservation practices such as enhancing (diminishing) the productive (unproductive) use of water in agriculture to help relieve the current pressure on water resources in arid zones. Reducing the water use footprint in agriculture, known as consumptive water, remains challenging. Consumptive water use is all the water lost during the agricultural cycle to the atmosphere through a process known as

evapotranspiration. This process can be separated into two components: evaporation (from soil, or open water bodies) and transpiration. In agricultural practices, evaporation is expected to occur at various stages: 1) during systematic pre-sowing irrigation to raise soil water content and ensure germination of annual crops or off-season early irrigation to flush salts from the soils' root zones and to refill the soil column with water for the regrowth of perennial crops; 2) during and after each irrigation events from the ponding water on the surface and the moisture in the upper soil layers that are most exposed to the wind and sun; 3) after each rainfall event from the water intercepted by the crops as well as the processes described in the previous point. As the growing season of the crop advances, both the plants' water requirements and the microclimatic conditions on the crops' soils change, and with it, the relative proportion of water that is consumed as transpiration for biomass production (i.e. productive water) and evaporation (i.e. unproductive water). In most instances, the relative or absolute magnitude of those productive and unproductive waters comprising the crops' consumptive water use are not known, measured or estimated. Knowing the magnitudes of these components and how they change over time in response to both climatic conditions and water management can help improve irrigation practices for water conservation and yield optimization. Reducing the unproductive water use of the crops' water footprint, especially early in the season, should lead to higher water use efficiency of crops in semi-arid and arid regions where water resources are depleting, and intensive agriculture is under constant stress.

Another problem faced by areas with intensive agricultural activity is using primarily low-efficiency irrigation systems with a lack of data-based water management practices. For example, in Mexico, some of the largest irrigation districts are located in the country's arid and semi-arid northern regions, where frequent and severe droughts can lead to significant reductions in

cultivated land, large losses in food production and economic hardship for communities relying on agricultural activities (Ojeda-Bustamante et al., 2007). Where systematic pre-sowing irrigation prevails ~30 days before the planting date, irrigation practices favor unproductive water use (evaporation). In these periods, there is still no vegetative activity, so the high evaporation rate is one of the critical factors causing water losses, especially in semi-arid areas (Banihabib et al., 2018). In addition, inefficient irrigation systems such as furrow irrigation and long parcels favor water losses as evaporation, runoff, and deep percolation (i.e. infiltration beyond the root zone). For these reasons, improving irrigation practices that increase the efficient use of water is urgently needed.

This work aims to develop and test an accessible methodology for partitioning evapotranspiration in croplands using vegetation indices (*PETVI*) during an agricultural cycle and assess its applicability in determining the productive and unproductive use of water at the plot that could be used to improve water conservation practices. To accomplish this goal, the specific objectives of this work are: (1) to evaluate the resulting T_r and Ev terms from the partitioning of ET_a from the *PETVI* model against various independent estimates of evaporation and transpiration using established approaches; and (2) to assess the utility of the ET partitioning at the plot scale for identifying the periods at which irrigation can be improved for water conservation.

2.2 Materials and Methods

2.2.1 Study site

The study was carried out at the Experimental Center for Technology Transfer (CETT, from its acronym in Spanish), an experimental site station owned and managed by the Sonoran Institute of Technology (ITSON, for its acronym in Spanish) located in the Yaqui Valley, in

Northwest Mexico (27.37º N latitude and -109.91º W longitude; see Figure 2.1). The climate in the Yaqui Valley is classified as semi-arid (Bsh according to Köppen classification) with a mean annual precipitation of 317 mm, most of which occurs between July and September (Méndez-Barroso et al., 2008). Irrigated winter wheat (*Triticum durum*, cv. CIRNO), the dominant crop in the region, is grown during the winter-spring cycle (November through May), followed by maize (*Zea mays*) and safflower (*Carthamus tinctorius*) (Meisner, 1992). Most of the region's soils are vertisols with less than 1% organic matter (Lobell et al., 2002). The experimental plot was located within the CETT facilities and covered an area of approximately 0.44 hectares (52 x 85 meters). Winter wheat was planted on December 19, 2018, following the wheat production practices in the region (Aquino-Mercado, 1998). Wheat planting was done 34 days after pre-planting irrigation using a seeding arrangement of three rows (separated by 15 centimeters) within an 80-cm bed with a seed density of 100 kg ha^{-1} and placed to a depth of 8 centimeters. Because soil moisture was not adequate for sowing in some parts of the plot, additional light irrigation was applied immediately after planting to ensure seedling emergence. Three additional irrigations were used at different crop stages. The observation period was performed during the key phenological development stages of the crop (February 2 to April 9)

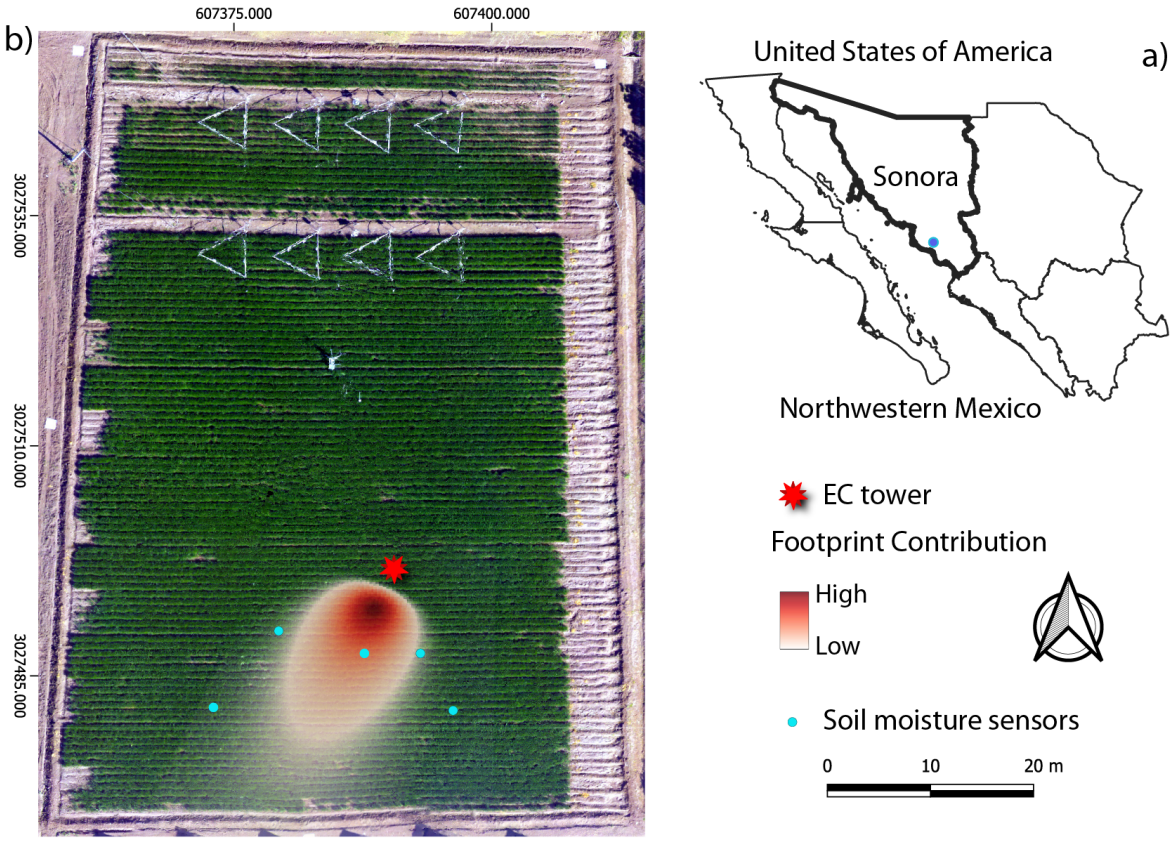

Figure 2.1) Location of the study area in northwestern Mexico, the study site represented by a blue dot, b) Aerial image of the Experimental parcel showing the location of the Eddy Covariance system (EC) denoted by the red star with its footprint (reddish oval)and the location of 5 soil moisture sensors (blue dots) 30 cm depth distributed within the footprint of the EC.

2.2.2 Data and Methods

2.2.3 Meteorological data

Meteorological data was collected from February 2 to April 9 from a standard weather station installed at 2.5 m within the experimental site. Observations were carried out at 5 second intervals and averaged every 30 minutes. Air temperature [°C] and relative humidity [%] were

measured using a Campbell Scientific CS-215 sensor (Campbell Scientific, Logan, UT, USA); net radiation (net shortwave and net longwave radiation [W m^{-2}]) was measured using a Kipp & Zonen NR Lite-2 net radiometer (OTT Hydromet, Delft, Netherlands). In contrast, precipitation [mm] was measured using a Texas electronics TE-525MM automatic tipping bucket rain gauge (Texas Electronics Inc., Dallas, TX, USA). A Campbell Scientific CR6 datalogger (Campbell Scientific, Logan, UT, USA) was used to record the meteorological data. The 30 min data was averages (ex., air temperature, relative humidity) or accumulated (ex., radiation, and rainfall) to obtain daily values.

2.2.4 Eddy Covariance Evapotranspiration measurement (EC)

An Eddy Covariance system (EC) was used to measure turbulent exchange fluxes of water, carbon, and energy between the experimental plot and the atmosphere from February 2 through April 9, 2019. The EC system consisted of a LI-COR LI-7500A open-path infrared gas analyzer (LI-COR biogeosciences, Lincoln, NE, USA) to measure at a high-frequency rate (10-Hz) the fluctuations in water and CO_2 concentrations and a Gill Windmaster Pro 3D-ultrasonic anemometer (Gill Instruments, Lemington, UK) to measure the three vector components of wind velocity (u, v, and w) at high frequencies. The meteorological instruments and the EC system were installed on a 3-m tall tripod. The EC system and the net radiometer were installed two meters above the surface. In contrast, the temperature-relative humidity sensor and the tipping-bucket rain gauge were installed at the upper end of the tripod (3-m). The footprint area captured by the EC system was calculated using a two-dimensional footprint model (Kljun et al., 2015) and enclosed a small 20-meter-wide domain southwest of the instruments (Figure 1). Volumetric water content [%] was obtained from a monitoring network of 5 soil moisture sensors (Campbell CS616, Logan,

UT, USA) deployed at different locations throughout the experimental plot. Soil moisture sensor rods were inserted perpendicular to the surface and captured the average water content of the top 30 cm profile of the soil. Sensors were calibrated prior to field installation using a linear fit model obtained from the relation between probe output frequency or period (microseconds) and gravimetric soil water content in the laboratory using soil from the area. Soil moisture readings from the network were recorded with a Campbell CR1000 datalogger (Campbell Scientific, Logan, UT, USA), averaging and storing data every 30-minutes.

Integrated 30-minute fluxes of CO_2, sensible (H [W m^{-2}]) and latent heat (λE [W m^{-2}]), and evapotranspiration (ET [mm]) were estimated from the raw high-frequency data using the processing tool EddyPro version 6.2.1 (LI-COR biogeosciences, Lincoln, NE, USA). Fluxes corrections were performed within EddyPro and included double rotation correction for Gill anemometers, spike removal, low-pass and high-pass filtering, and density corrections for air temperature and relative humidity fluctuations (Burba and Anderson, 2010). Quality control of the corrected 30-minute fluxes was performed by applying the flagging system developed by Mauder and Foken (2006), followed by removal of fluxes collected during rainfall events and below a friction velocity (u*) threshold of 0.29 ms^{-1}. Finally, CO_2, energy, and ET flux outliers were removed by eliminating those fluxes that were two-standard deviations above and below flux mean.

2.2.5 Remote sensing data

For the evapotranspiration partition process, we used remote sensing data available from three main sources: (1) Sentinel-2 hyperspectral imagery to calculate vegetation indices and the fraction of vegetation and soil cover at the plot (Defourny et al., 2019; Dimitrov et al., 2019; Xue

& Su, 2017); (2) Landsat derived ET from the METRIC algorithm (Allen et al., 2007); (3) high-resolution hyperspectral images taken using an unmanned aerial vehicle (UAV). The following subsections describe in detail each of these remote-sensing data products.

2.2.6 Sentinel-2 data pre-processing

Sentinel-2 is a constellation of 2 polar-orbiting satellites with a variable revisiting time depending on latitude, producing multispectral images with a 10 m spatial resolution. We acquired Sentinel-2 (*S2*) top-of-atmosphere reflectance (TOA) data from November 2018 to May 2019 (Table 2.1). Specifically, we used bands in the near-infrared (~0.84 μm wavelength) and the red (~ 0.66 μm central wavelength) portion of the electromagnetic spectrum (Huete et al., 2002) to create a time series of the Normalized Difference Vegetation Index (*NDVI*) for monitoring vegetation dynamics (Martínez & Gilabert, 2009) during the crop growth cycle. We processed all S-2 images in the Google Earth Engine (*GEE*) online platform. S-2 images in *GEE* have been atmospherically corrected (Zhang et al., 2019).

Table 2.1 Images selected from S-2 with their main characteristics; Granule ID, sensing date, and clouds cover percentage.

Granule ID	sensing date	Clouds percentage*
L1C_T12RXR_A008747_20181108T175835	2018-11-08	0
L1C_T12RXR_A017727_20181113T180219	2018-11-13	0
L1C_T12RXR_A018013_20181203T180113	2018-12-03	0
L1C_T12RXR_A018156_20181213T180605	2018-12-13	0
L1C_T12RXR_A018299_20181223T175737	2018-12-23	0
L1C_T12RXR_A009462_20181228T180308	2018-12-28	14
L1C_T12RXR_A018442_20190102T175731	2019-01-02	2
L1C_T12RXR_A009605_20190107T180358	2019-01-07	15
L1C_T12RXR_A018728_20190122T180402	2019-01-22	60
L1C_T12RXR_A009891_20190127T175854	2019-01-27	0.14
L1C_T12RXR_A010177_20190216T175907	2019-02-16	0
L1C_T12RXR_A010320_20190226T180543	2019-02-26	11.7
L1C_T12RXR_A019443_20190313T175842	2019-03-13	6.9
L1C_T12RXR_A010606_20190318T180200	2019-03-18	0.49
L1C_T12RXR_A019586_20190323T175719	2019-03-23	0
L1C_T12RXR_A010749_20190328T175739	2019-03-28	0
L1C_T12RXR_A010892_20190407T180036	2019-04-07	0
L1C_T12RXR_A019872_20190412T175958	2019-04-12	1.4

L1C_T12RXR_A011178_20190427T180043	2019-04-27	34
L1C_T12RXR_A011321_20190507T180044	2019-05-07	10
L1C_T12RXR_A020301_20190512T180340	2019-05-12	12
L1C_T12RXR_A011607_20190527T180038	2019-05-27	0

* information from metadata quality indicator.

2.2.7 METRIC data

The "Mapping Evapotranspiration at high Resolution with Internalized Calibration" (*METRIC*) product is available from Earth Engine Evapotranspiration Flux (*EEFlux*) website (https://eeflux-level1.appspot.com/) (Allen et al., 2007; Allen et al., 2015; Allen et al., 2011; Wan et al., 2021), was used to retrieve ET_a for our study period. We use ET_a from both Landsat 7 and 8 missions selecting the best available images. To obtain the highest temporal resolution and best data quality, we inspected all images within the study period and selected those without clearer cloud issues for our study site (Table 2.2).

Table 2.2 Images selected from Landsat 7 and 8 with their main characteristics Granule ID, sensing date, and clouds cover percentage.

Granule ID	sensing date	Cloud percentage
LE70340412018314EDC00	2018-11-10	0
LC80340412018322LGN00	2018-11-18	19
LE70340412018346EDC00	2018-12-12	70
LC80340412018354LGN00	2018-12-20	0

LE70340412018362EDC00	2018-12-28	23
LE70340412019013EDC00	2019-01-13	0
LC80340412019021LGN00	2019-01-21	8
LC80340412019037LGN00	2019-02-06	76
LE70340412019077EDC00	2019-03-18	1
LC80340412019085LGN00	2019-03-26	45
LE70340412019093EDC00	2019-04-03	0
LC80340412019101LGN00	2019-04-11	0
LE70340412019109EDC00	2019-04-19	43
LC80340412019117LGN00	2019-04-27	4
LC80340412019133LGN00	2019-05-13	0
LE70340412019141EDC00	2019-05-21	0

2.2.8 Multispectral high spatial resolution images from Unmanned Aerial Vehicle Surveys

A 3DR Solo quadcopter (3DRobotics Inc., San Diego, CA, USA), hereinafter referred to as unmanned aerial vehicle (*UAV*), equipped with a Mapir Survey-2 multi-spectral camera (MAPIR Inc., San Diego, CA, USA) and Pixhawk 2.0 autonomous flight controller (Ardupilot development team) was used to obtain high spatial resolution images at different times during the wheat growing season. Ground sample distance (*GSD*) was ~7 cm per pixel. *UAV* flight routine

was programmed for a flight speed of 5 m/s, an altitude of 20 m with and a side/forward overlap of 70% to ensure highest image quality. The MAPIR Survey-2 camera has a dual band-filter that captures reflected light in the red (660 nm) and near infrared (870 nm) regions with a resolution of 16 MP and a focal length of 23 mm. To ensure a good image mosaic, the camera was set to 2-second shooting intervals, a shutter speed of 1/500 seconds, an ISO value of 50, and a focal aperture of f/2.8. Camera was calibrated before each flight using a calibration ground target that consisted of four targets with known reflectance value. Image alignment, Normalized Difference Vegetation Index (*NDVI*) calculation, and orthophotos generation were performed in Agisoft Metashape v1.6. A total of 6 *NDVI*-orthophotos were acquired from February 15 to March 28, 2019. All images were taken around local noon to avoid shading issues and maximize illumination. UAV-based *NDVI* orthophotos were uploaded into the *GEE* platform to estimate the basal crop coefficient (K_{cb}).

2.2.9 Development of the Partitioning Evapotranspiration through Vegetation Indices algorithm (PETVI)

We propose a method to estimate the water exchange between cropland and the atmosphere that allows inferring the amounts of water transferred to the atmosphere by the plants and those that are evaporated directly from the soil. The approach takes into consideration the prevailing meteorological conditions in the area and the energy balance of the parcel, and it is based on a combination of the dual crop coefficient method to calculate *ET* (Allen et al., 2007) and an energy balance algorithm such as geeSEBAL (Laipelt et al., 2021). Figure 2.2 shows the criterion and the components of the crop coefficient (K_c) considered in our approach, which is represented by a curve that has the same shape as the phenological evolution of the crop. This K_c comprises two

coefficients: the evaporation coefficient (K_e) and the basal crop coefficient (K_{cb}). Typically, the K_e at the beginning of the crop cycle is higher, especially if the soil is wetted by irrigation or rain. It decreases as the soil dries or is covered by vegetation. On the other hand, K_{cb} has an inverse relationship to K_e; K_{cb} values are low at the beginning of the season because it represents the proportion of active vegetation transpiring, which is minimal early in the season. However, K_{cb} increases with crop development and reaches its maximum value when the crop reaches its full development. K_c is usually estimated using a lysimeter or relating crop height and meteorological variables (Ko et al., 2009). However, these measurements are not always recorded in the field, but it is possible to infer them from independent estimates of *ET* using the relationship $K_c = ET_a/ET_0$ (Allen et al., 1998). Discrete daily values of ET_a can be derived from energy balance algorithms using satellite imagery and meteorological data (e.g. geeSEBAL, Laipelt et al., 2021; eeMETRIC, Allen et al., 2011). Although the K_c function can vary in response to year-to-year variations in climate conditions and availability of water, for most crops, the shape has been widely studied and therefore is well known, and it can be reconstructed by simple linear interpolation from a few values distributed throughout the growing season (Allen et al., 2007; Duchemin et al., 2006; Kumar Gontia et al., 2010). On the other hand, the shape of the K_{cb} function can be tracked by following the phenology of the crop using a vegetation index, such as the *NDVI*. In other words, K_{cb} can be inferred using satellite-derived vegetation indices. It is also worth noting that in a well-watered crop, the phenology of the vegetation shows a smooth curve, and potential issues of spurious values on the vegetation indices can be easily discarded by removing outliers and interpolation in between satellite images to obtain daily vegetation index values can be performed. In summary, this technique is based on well-documented methods for quantifying crops' water

needs by following their phenological activity during their growth cycle (Allen and Pereira, 2009; Pôças et al., 2015; Paço et al., 2014; Ran et al., 2017; Allen et al., 2007).

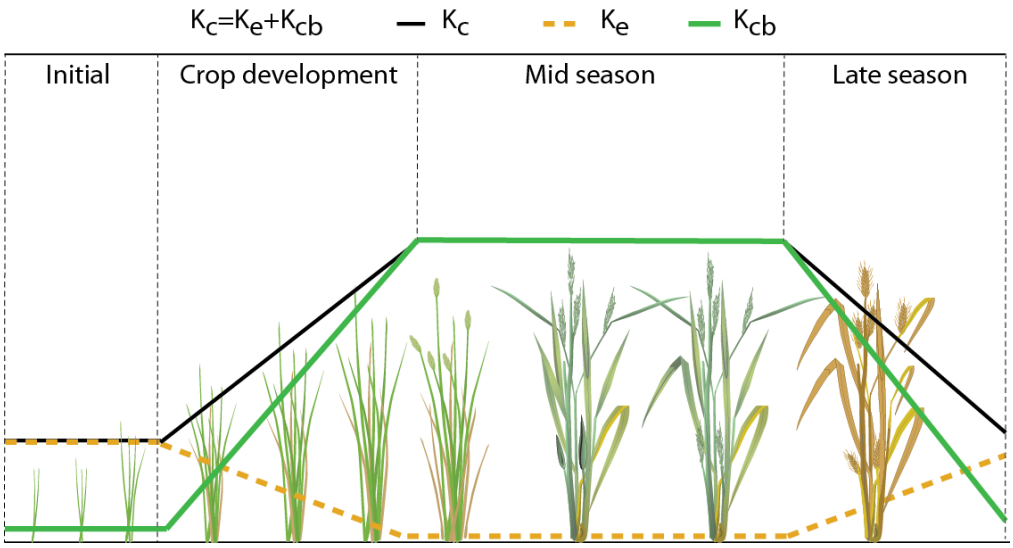

Figure 2.2 Representation of the phenological evolution of the crop and its corresponding crop coefficient represented by a solid black line (K_c) throughout the growing season as comprised of basal crop coefficient (K_{cb}) green solid line, and the soil crop coefficient (K_e) yellow dashed line.

Figure 2.3 shows the flow diagram of the algorithm developed for partitioning evapotranspiration through the vegetation index (*PETVI*) method. The yellow boxes represent the main inputs (from top to bottom: *S-2* images, daily micrometeorological variables, and Landsat 7 and 8 data), the blue boxes show the calculations, and the green boxes show the outputs. Following the schematic, first, *NDVI* values are calculated from *S-2* images and rescaled into basal crop coefficient (K_{cb}) using equation 4. Detailed description of each process in Figure 3 is described in the following subsections.

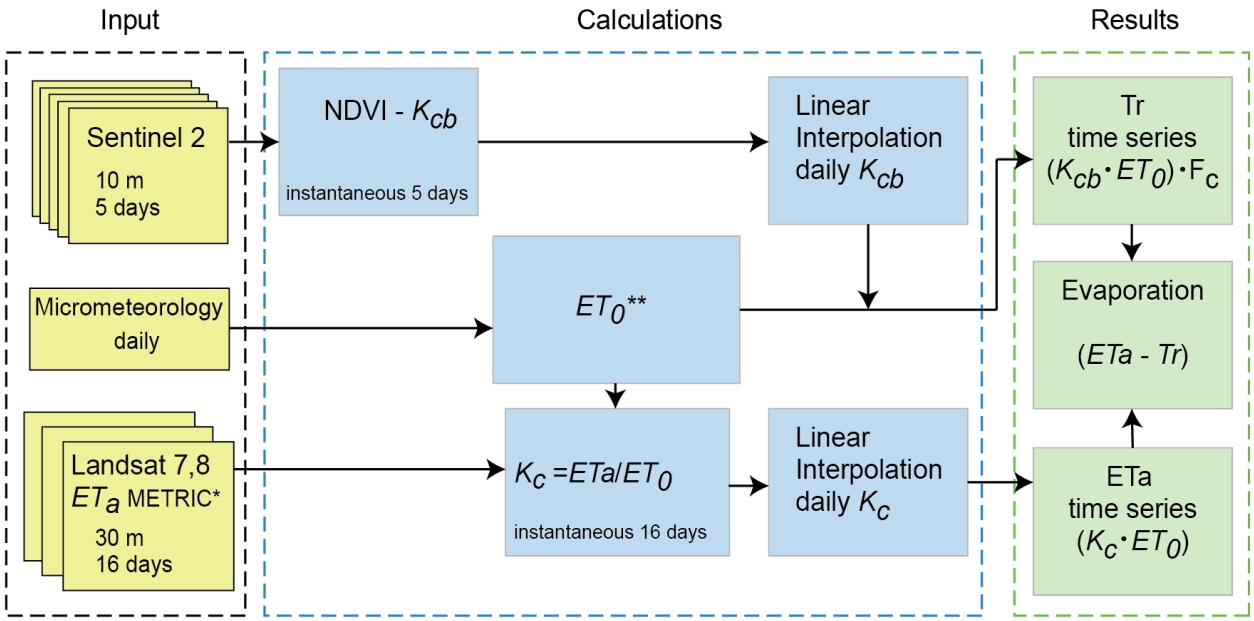

**Allen et al., 2007; ** Penman-Monteith, Allen et al., 1998.*

Figure 2.3 Flow diagram for estimating the evapotranspiration partitioning on productive water (Tr) versus unproductive water (Ev) through the partitioning evapotranspiration through vegetation index (PETVI) method. The input variables shown in yellow (from top to bottom) are S-2 images with a temporal resolution of 5 days and spatial resolution of 10 m., Meteorological data from the weather stations, and evapotranspiration (ET_a) images from the METRIC algorithm. The blue squares show the calculation of the complementary variables to partition evapotranspiration (ET_a). The green squares show the last step of the calculations; transpiration (T_r) is calculated as the product of the K_{cb} times ET_0, and K_c times ET_0 to calculate ET_a. Evaporation (Ev) is the residual between ET_a end T_r.

2.2.10 Transpiration using Basal crop Coefficient (K_{cb}) and Vegetation Fraction (F_c)

We propose a method to estimate a daily basal crop coefficient (K_{cb}) using a vegetation index (*VI*) following the close relationship between *VI's* and crop development during the growing cycle, and the fact that they are in close correspondence with transpiration demands (Allen et al.,

2011; Glenn et al., 2008). To monitor vegetation growth dynamics, we calculated the normalized difference vegetation index (*NDVI*) using *S-2* imagery. The images were processed in the *GEE* platform (Gorelick et al., 2017; Kandekar et al., 2021) using bands 8 (near-infrared) and 4 (red). Before the analysis, the area of interest is defined inside *GEE* by loading a shapefile using the assets manager. For the calculation of *NDVI*, no cloudiness filter was performed on the images at this stage because sometimes an image may have a high percentage of cloudiness, but the study site may be free of clouds. Once *NDVI* values had been established for the days with available satellite observations, a quality control procedure was carried out to eliminate spurious values that may have been produced by contamination of the reflectance values in the satellite images from cirrus clouds or cloud shading. To do this, we plotted the *NDVI* time series and identified abnormal data values by locating unrealistic sudden drops of *NDVI* that depart from the normal evolution of the vegetation cycle; we eliminated data values from those dates to generate a clean time series. After that procedure, instantaneous K_{cb} values were calculated from the *NDVI* time series by rescaling the *NDVI* values to the seasonally maximum possible K_c reported for that particular crop using the equation for the vegetation cover fraction (Schüttemeyer et al., 2007; Allen et al., 1998; Hunsaker et al., 2005):

$$K_{cb} = 1.15 * \frac{NDVI - NDVI_{min}}{NDVI_{max} - NDVI_{min}} \quad (1).$$

In our study we used $NDVI_{min}$ = 0.10, $NDVI_{max}$ = 0.75 and a maximum value of 1.15 for the wheat crop coefficient (K_c). The maximum value of K_c represents an upper limit of evaporation and transpiration from a cultivated area. It is assigned to reflect the crop's surface limitations in using the available energy to transfer water directly from the soil or through the plant to the atmosphere. K_c max ranges from about 1.05 to 1.30 when using the grass reference ET_0: (Allen et al., 1998). Drerup et al., 2017, used the same K_c value to calculate wheat's basal crop coefficient

(K_{cb}) at an experimental site in Hanninghof, Germany. Another study by Ko et al., 2009 in Uvalde, Texas, found maximum K_c values of 1.15 during three irrigation seasons using lysimeter measurements, coinciding with those used by Allen et al., 1998. Because the K_{cb} function of a well-watered crop should follow a relatively smooth trajectory, daily K_{cb} values can be obtained by linearly interpolating between the satellite-derived values, producing a daily time series of K_{cb}. During the growing cycle of the crop one of the most important variables changing the proportion of evaporation to transpiration is the evolution of the vegetation fractional cover F_c. As F_c grows, the area of exposed bare soil decreases reducing the direct evaporation of soil moisture, while the vegetation demand of water increases and with it the fraction of ET that becomes transpiration. To account for this process, we calculated F_c through the entire growing cycle with two methods: 1) using an unmixing model to separate the different land cover types (soil, vegetation, and water) using the *S-2* images with vegetation and soil indices to determine manually the control points based on the known land surface cover (Vermuelen et al., 2021; Xu and Somers, 2021); and 2) using a linear relationship with *NDVI* from *S-2* following (Irmak et al., 2012) (Eq 2.). Both methods yielded very similar F_c values and we chose to use the NDVI linear relationship approach to maintain the simplicity of the method since unmixing models require training of endmembers for decomposing the spectral signal of the various land cover types diminishing the parsimony of the method.

$$F_c = \frac{NDVI - NDVI_{min}}{NDVI_{max} - NDVI_{min}} \quad \text{Eq. (2).}$$

The final form of the equation for T_r is then as follows:

$$T_r = K_{cb} * F_c * ET_0 = 1.15 * \left[\frac{NDVI - NDVI_{min}}{NDVI_{max} - NDVI_{min}}\right]^2 * ET_0 \quad \text{Eq. (3).}$$

2.2.11 Evapotranspiration from METRIC.

For our study period, we used ET_a data [mm day^{-1}] derived from the *METRIC* algorithm (Allen et al., 2007) using Landsat 7 and 8 missions (path 034 and row 040)1 with a spatial resolution of 30 m and temporal resolution of 16 days. The images were obtained from the *EEFLux* website https://eeflux-level1.appspot.com/ (Allen et al., 2007; Allen et al., 2015; Allen et al., 2011; Wan et al., 2021) and inspected manually to select those free of cloudiness for the study area. The images were uploaded into an image collection inside *GEE* with their respective metadata. Once the collection of images was created, a scene cut was made for the area of interest using a shapefile. Given the characteristics of the study, it was necessary to have daily ET_a values. However, linear interpolation of ET_a values is not possible due to their dependence on daily conditions in local weather that can vary substantially from day to day. To overcome this problem, we derived K_c values from the satellite-derived ET_a following the well-established relationship between the ratio of evapotranspiration and the reference Evapotranspiration (ET_0) from local weather data to K_c (Eq. 4).

$$K_c = \frac{ET_a}{ET_0} \qquad \text{Eq. (4).}$$

where K_c is the crop coefficient, ET_a is the daily evapotranspiration from *METRIC*, and ET_0 is the reference evapotranspiration. Using equation 4, we obtained the K_c daily values. With this approach, some dates with low ET_a can yield lower K_c values than those expected based on the crop phenological stage. Therefore, ET_a images obtained from the energy balance algorithm (i.e. *METRIC*) need to be previously calibrated by adjusting the K_c using the tabulated values and observations of the crop in the experimental site based on its phenological stage.

2.2.12 Reference evapotranspiration

Standard meteorological data collected every 30 minutes by a weather station installed within the study plot was used to estimate the reference evapotranspiration (ET_0) using the Penman-Monteith equation at a daily scale (Allen et al., 1998):

$$ET_0 = \frac{0.408\Delta(R_n - G) + \gamma\left(\frac{900}{T+273}\right)u_2(e_s - e_a)}{\Delta + \gamma(1 + 0.34u_2)} \quad \text{Eq. (5).}$$

where ET_0 is the reference evapotranspiration (mm day^{-1}), R_n is the net radiation (MJ m^2 day^{-1}), G is the heat flux density of the soil (MJ m^2 day^{-1}), T is the daily mean air temperature at 2 m height (° C), u_2 is the wind speed at 2 m height (m s^{-1}), e_s is the saturation vapor pressure (kPa), e_a is the real vapor pressure (kPa), Δ is the slope of the vapor pressure curve (kPa ° C^{-1}), γ is the psychrometric constant (kPa ° C^{-1}), and e_s-e_a is the saturation vapor pressure deficit (kPa).

2.2.13 Partitioning Evapotranspiration

The ET flux separation in evaporation (Ev) and transpiration (T_r) for the proposed approach was estimated as the residual of ET_a and T_r, similar to the FAO-56 dual crop coefficient method (Allen et al., 1998; Allen, 2000). Our approach diverges from previous versions of the dual crop coefficient method in the way we obtained daily values of T_r and ET_a, by using the smooth function of the phenology of a well-watered crop to obtain values for K_{cb} and K_c in between days were vegetation indices and satellite-derived ET_a observations are not available.

2.2.14 Evapotranspiration from the Maximum Entropy Production Model (MEP-ET)

In this study, we used the Maximum Entropy Production model of evapotranspiration (MEP-ET) (Wang and Bras, 2011) estimate point-scale soil evaporation directly in the experimental plot. The MEP-ET calculates soil evaporation (E) by solving the energy balance (eqn.1) simultaneously with sensible heat flux (H [W m^{-2}]) and ground heat flux (G [W m^2]) as follows:

$$R_n = E + H + G, \quad \text{Eq. (6)}$$

$$G = \frac{\beta(\sigma)}{\sigma} \frac{I_S}{I_0} H|H|^{-\frac{1}{6}}, \quad \text{Eq. (7)}$$

$$E = \beta(\sigma)H, \quad \text{Eq. (8)}$$

where R_n is the net radiation at the evaporating surface (W m^2), I_s and I_0 are the thermal inertia and "apparent thermal inertia" of the soil and air, respectively (W m^{-2} K^{-} s$^{1/2}$) [Wang and Bras, 2009], b(σ) is the reciprocal of the Bowen ratio [-] expressed as:

$$\beta(\sigma) = 6\left(\sqrt{1 + \frac{11}{36}\sigma} - 1\right), \quad \text{Eq. (9)}$$

where s is a dimensionless parameter characterizing the thermal-moisture state of the evaporating surface as a function of surface temperature (T_s [K]) and specific humidity (q_s [kg kg^{-1}]):

$$\sigma(T_s, q_s) = \frac{\lambda^2}{c_p R_v} \frac{q_s}{T_s^2}, \quad \text{Eq. (10)}$$

where l is the vaporization heat of liquid water [J kg^{-1}], c_p is the specific heat of air under constant pressure [J kg^{-1}], and R_v is the gas constant for water vapor [J K kg^{-1}]. For the derivation of equations 4 and 5 the reader is referred to the work of Wang and Bras (2011).

2.2.15 Underlying Water Use Efficiency (*uWUE*) model

The capacity to produce biomass through photosynthesis per unit of water consumed can be quantified through the Water Use Efficiency (WUE) at the plant/canopy, and ecosystem levels (Blum, 2005; Niu et al., 2011; Tang et al., 2014). Water consumption at the plot scale can be associated with stomatal, and stomatal/non-stomatal fluxes (Zhu et al., 2015; Drake et al., 2017). Therefore, if the water consumed is observed at the plant/canopy level (only stomatal behavior), it can be related to transpiration. In contrast, if it is observed at the plot or ecosystem level (stomatal/non-stomatal behaviors), it is related to evapotranspiration (Tang et al., 2014). The underlying Water Use Efficiency ($uWUE$) method developed by Zhou et al. (2016), based on a stomatal conductance model, establishes a maximum or potential (constant) Water Use Efficiency ($uWUEp$) that is related to the transpiration (T_r) during the growing season, and an averaged or apparent (periodically changing) Water Use Efficiency ($uWUEa$) that is related to evapotranspiration (ET), as follows:

$$uWUEp = \frac{GPP\sqrt{VPD}}{Tr} \quad \text{Eq. (11).}$$

$$uWUEa = \frac{GPP\sqrt{VPD}}{ET} \quad \text{Eq. (12).}$$

Where GPP is the gross primary production i.e. the amount of carbon fixed during photosynthesis by the ecosystem, and the VPD is the vapor-pressure deficit. Since GPP, VPD, and ET could be obtained from Eddy Covariance observations, the $uWUEp$ and $uWUEa$, are derived statistically from those variables time series using a 95-quantile (to capture the maximum transpiration response) and a mean linear regression method ($GPP\sqrt{VPD}$ over ET), respectively (Zhou et al., 2016). Thus, T_r/ET can be calculated by dividing $uWUEa$ to $uWUEp$:

$$Tr = \left(\frac{uWUEa}{uWUEp}\right) ET \qquad \text{Eq. (13).}$$

The $uWUE$ method has been used and evaluated in various ecosystems including croplands (Zhou et al., 2016; Zhou et al., 2018; Jiang et al., 2020; Chen et al., 2022).

2.3 Results

2.3.1 Climatology

The observed meteorological conditions during the crop's observation periods are shown in Figure 2.4. The daily average temperature was 16.8 °C, and the vapor pressure deficit (*VPD*) ranged between 0.36 to 1.88. Average net radiation during the observation period was 111.1 W $m^{-2,}$ with daily maximum values of net radiation (*Rn*) ~124.2 W m^{-2} until March 11, after which *Rn* steadily increased to a maximum of 179 Wm^{-2} on the last day of observation. The maximum wind speed was 2.56 m s^{-1} on February 7, and the average wind speed was 1.3 m s^{-1}. Three small rain events were recorded during the observation period. The maximum rainfall recorded was 0.7 mm day^{-1} on February 11. The total rainfall during the observation period was recorded at 1.3 mm,

showed minimum values of 0.88 and maximum values of 6.75 mm day^{-1}, and an average of 3.68 mm day^{-1}, with inflections that coincided with substantial decreases in *Rn*.

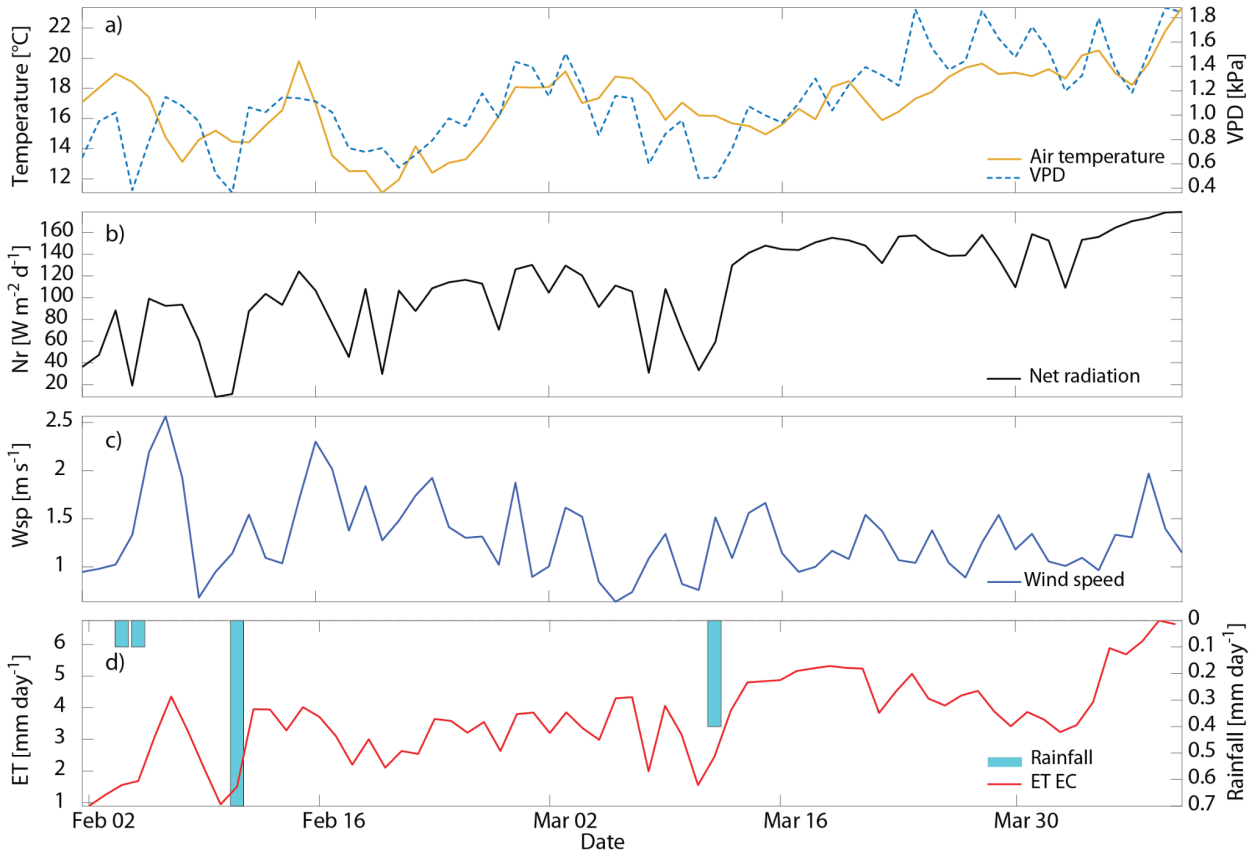

Figure 2.4 Environmental conditions during the observation period from February 2 to April 9, 2019. In panel a), the orange line indicates the daily average air temperature, and the dashed blue line denotes the vapor pressure deficit (VPD). The black line in panel b) represents the net radiation (Rn). Panel c) represents the wind speed. The blue bars in panel d) represent precipitation in mm dia^{-1}, and the red line denotes Evapotranspiration (ET, mm dia^{-1}) measured by the Eddy covariance system

2.3.2 Dynamics of Evapotranspiration during the growing cycle.

The phenological stages of the crop were measured on the field based on the day-after-sowing (*DAS*) method. The complete cycle for the wheat grown, from sowing (*So*) to physiological maturity (*Pm*), takes ~139 days. The *NDVI* closely tracked the trajectory of the phenological stages

during the observation period, with a steep rising limb at the start of tillering to reaching its maximum around F, and then slightly decreasing between grain filling to milk grain, after which a steep and steady decrease takes the *NDVI* values close to 0.19. At that stage, the plant has reduced its physiological activities significantly and, as a consequence, the water transfer rates from transpiration. The temporal dynamics of *ET* in the experimental plot also closely follow the trajectories of the *NDVI* and phenology of the crop in all estimates from the various methods employed (Figure 2.5 b); at the beginning of the crop establishment period, a considerable increment in *ET* from 0 to 3.4 mm day^{-1} occurred (observed from the METRIC derived ET). The *ET* rate decreased on February 6, reaching 0.04 mm $day^{-1,}$ after which it increased gradually, showing inflections at various times coinciding with the observed rainfall events (Figure 4). Except for a time in mid-December, large increases in *ET* are always observed a day after irrigation events. Notably, Figure 2.5 c) shows close agreement among the trajectory of three independent *ET* estimates (Eddy Covariance, METRIC, and MEP) and the T_r obtained from PETVI and the *uWUE* methods during the observation period, suggesting the majority of *ET* was coming from crop transpiration. After the last irrigation, the *ET* and Transpiration (T_r) showed similar values until April 11, then, *ET* and T_r started to diverge, suggesting the beginning of crop physiological maturity and a sustained decline in transpiration (T_r). Initially, the average transpiration rate in the first 58 days is 0.22 mm day^{-1} due to the presence of some weeds. After that, the transpiration values follow the same trajectory as the *ET*. The maximum recorded value of T_r was, 6.15 mm day^{-1}. As of April 11, the values started to decrease as a result of diminished vegetation activity when the crop reached physiological maturity, and its water use eventually approaches 0.

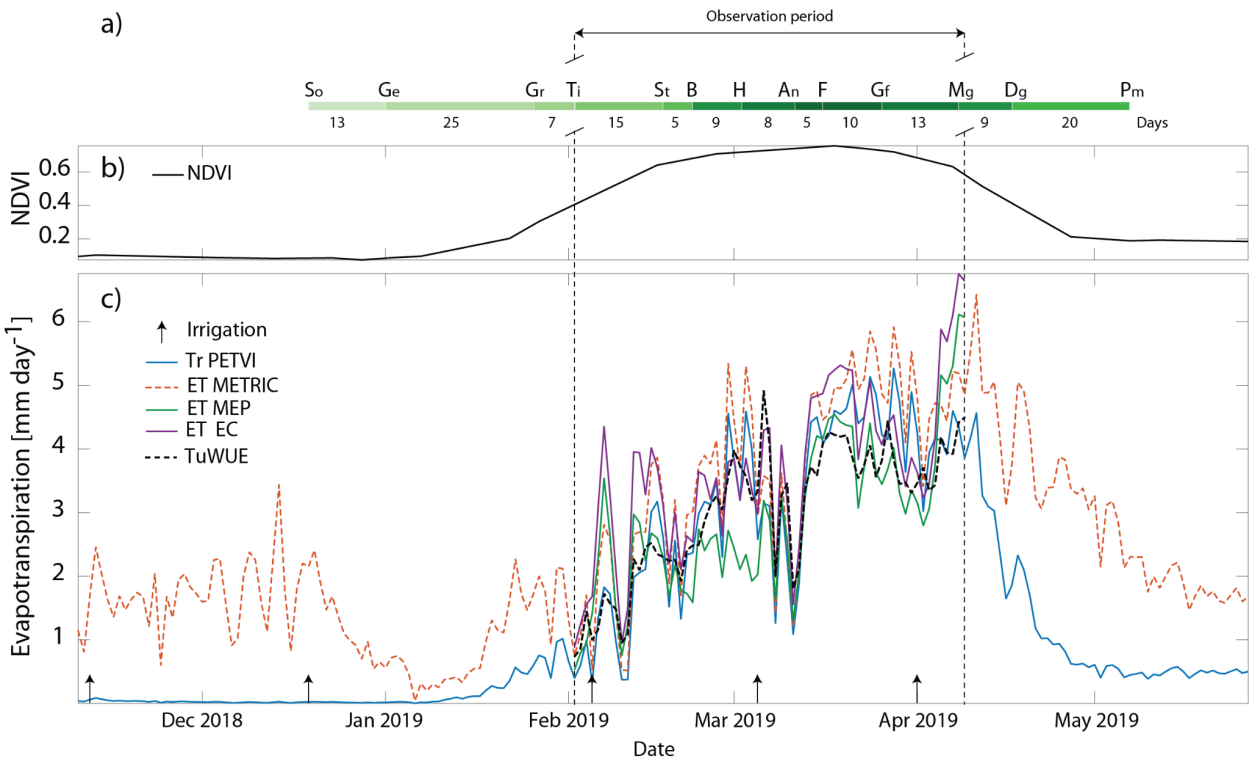

Figure 2.5 a) Phenological stages of wheat in the study area: (S) sowing, (Fi) flowering initiation, (Ts) Terminal spikelet, (Fn) First node, (H) Heading, (An) Anthesis, and (Pm), Physiological maturity; b) Evolution of NDVI during the agricultural cycle (black line); c) Evapotranspiration (ET) and transpiration (T_r) time series calculated using observation data and different methods: T_{rPETVI} (blue line), ET_{METRIC} (red dashed line), ET_{MEP} (green line), ET_{EC} (purple line) T_{ruWUE} (black dashed line). Black arrows pointing up show times of irrigation events)

2.3.3 Performance of Evapotranspiration Models

2.3.4 Evapotranspiration from Eddy covariance (ET_{EC}), Evapotranspiration from METRIC algorithm (ET_M).

The temporal evolution of ET measured with the Eddy Coviariance method (ET_{EC}), and the one estimated from *METRIC* (ET_M) are shown in figure 2.6 a). Minimum and maximum values of ET_{EC} during the growing period were 0.88 and 6.75 mm day^{-1} respectively while ET_M were 0.75 and 5.91 mm day^{-1}. Overall, both methods show a similar *ET* pattern diverging briefly on some

days. For example, ET_M overestimates ET_{EC} on February 28 and March 3, with an average difference between the observed and estimated value of 1.49 mm. On March 28, the difference between the ET_{EC} and the ET_M was 1.55 mm, with the largest discrepancy occurring on March 31 with 1.66 mm. In general when daily *ET* was below 5 mm day^{-1}, there is a good correlation between estimated and observed values, and the periods of maximum discrepancy occurred on days of large ET (>5mm). The cumulative *ET* of the observed values was 246.5 mm, while for the METRIC method was 244.9 mm. That is a difference of 1.6 mm during the observation period, providing confidence in the performance of the ET_M.

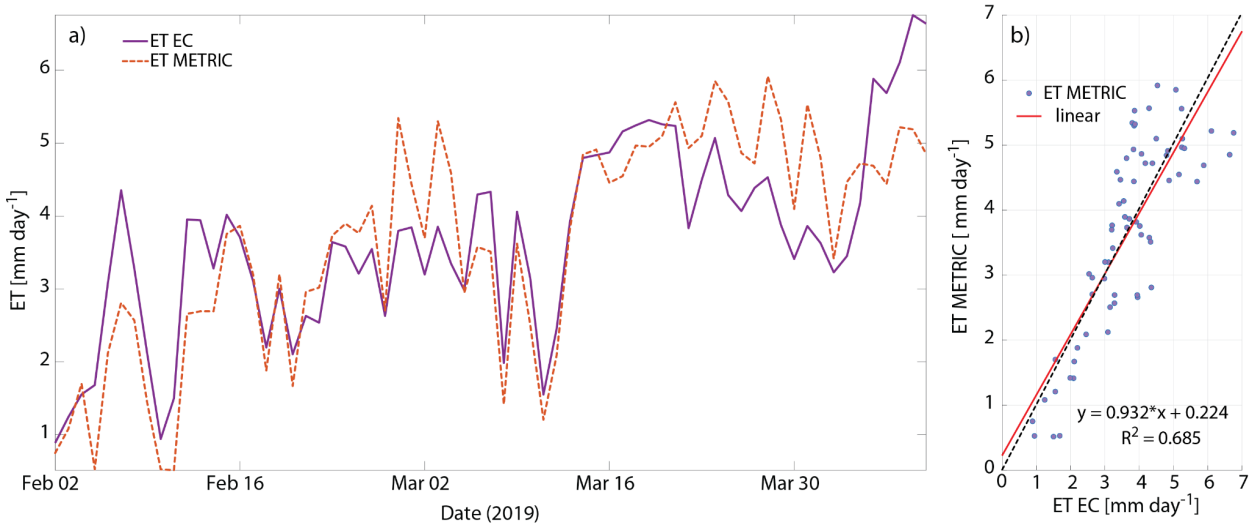

Figure 2.6 a) Time series of ET from the EC system (solid line), and the METRIC method (dotted line); b) scatter diagram comparing the measured (ET_{EC}) and estimated (ET_{METRIC}) evapotranspiration in the experimental plot; the red line shows the slope of the function, the dotted line shows the 1:1 relation of the linear regression.

2.3.5 Performance of Transpiration models.

2.3.6 Transpiration from uWUE as reference method

The performance of the uWUE method in obtaining accurate estimates of T_r relies on the correct estimation of the potential uWUE, which can be obtained during the period of fastest vegetation development. The *NDVI* data during the agricultural cycle used in this study show that the fastest growing period of this crop takes place between February 2 and 20 (Figure 2.5 b). Therefore, we take a sample for this period to determine the *uWUEp* through the slope of the 95th quantile regression between $GPP \cdot VPD^{0.5}$ and ET (Eq. 11). The slope indicated that *uWUEp* was $13.56\ g_C\ hpa^{0.5}/kg_{H2O}$ (Figure 2.5 a). By applying a linear regression (Eq. 12) to every daily data sample, we can determine the daily uWUEa for the entire time series (Figure 2.6 b). The daily uWUEa/uWUEp ratio determines the daily Tr/ET ratio for the period of observation. Finally, the half-hour ET data were accumulated to daily values, and applying the daily values of the T_r/ET ratio to the daily ET series we can obtain both the Tr and E daily time series (Figure 2.8 a and Figure 2.10 a).

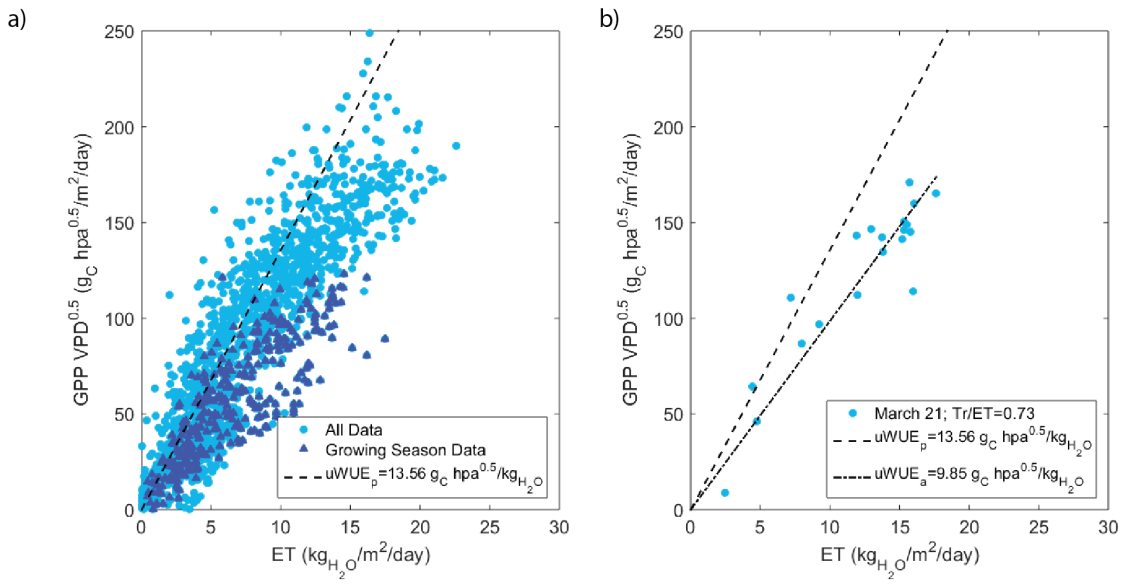

Figure 2.7 The 95th quantile regression using the half-hourly growing season data (between February 2 and 20) for our site to estimate uWUEp and b) the linear regression using half-hourly data for March 21 to estimate uWUEa for this day. The uWUa/uWUEp determines the T/ET ratio. The intercept was set to zero for both quantile and linear regressions.

2.3.7 Performance of Transpiration from PETVI and ET_{EC} - Ev_{MEP}

When evaluating the dynamics of transpiration during the observation period from the different methods employed, we took $T_{r\ uWUE}$ as the reference (i.e. closer to true value) to assess the performance of the T_r values using the *PETVI* method ($T_{r\ PETVI}$) and transpiration as a residual of ET_{EC} and Ev_{MEP} ($T_r = ET_{EC} - Ev_{MEP}$). The transpiration values calculated with the $ET_{EC} - Ev_{MEP}$ method ranged from 0.56 to 6.61 mm day^{-1}, while the $T_{r\ PETVI}$ values ranged from 0.39 to 5.26 mm day^{-1}, and the $T_{r\ uWUE}$ recorded values from 0.73 to 4.92 mm day^{-1}. The total amount of water transferred to the atmosphere by transpiration during the observation period using the $T_r ET_{EC\ -\ MEP}$ method was 237.9 mm., while for the $T_{r\ PETVI}$ method was 209.2 mm, and for the $T_{r\ uWUE}$ was 202.7 mm. The difference between the uWUE and the other approaches ranged between 35 mm and 6

mm for $T_r\ ET_{EC}$ - *MEP* and $T_{r\ PETVI,}$ respectively. Generally, the values calculated using $T_r\ ET_{EC\text{-}MEP}$ overestimate the values obtained using the *uWUE*, while the values estimated using *PETVI* are similar in magnitude to the values obtained using the *uWUE* method (Figure 2.8). All methods show similar trajectories of transpiration, increasing and decreasing together and as a result yield similar correlation coefficients (between 0.85 and .087; Figure 7.c). When the magnitude in the transpiration rate increases during the observation period, $T_{r\ PETVI}$ shows little dispersion relative to $T_{r\ uWUE}$ but maintains a high correlation coefficient of 0.87. $T_r ET_{EC}$ - Ev_{MEP} tends to overestimate $T_{r\ uWUE}$ at the beginning and at the end of the observation period (Figure 2.7 a,b). Intercomparison of the three T_r methods using a taylor diagram (Figure 2.7 c) show $T_{r\ PETVI}$ (blue diamond), closely agreeing with $T_{r\ uWUE,}$ with a root mean square difference (*RMSD*) of 0.66 mm day^{-1}, a correlation coefficient 0.87, and standard deviation of 1.21 mm day^{-1}, similar to the 1.04 mm day^{-1} standard deviation of $T_{r\ uWUE}$; on the other hand, $T_r\ ET_{EC}$ - Ev_{MEP} has a standard deviation of 1.13 mm day-1, a correlation coefficient of 0.85, and a *RMSD* of 0.69 mm day^{-1}. Summarizing, both transpiration estimation methods show large correlation coefficients, relatively small *RMSD (<0.7mm day^{-1})* and similar standard deviations relative to T_r *uWUE*.

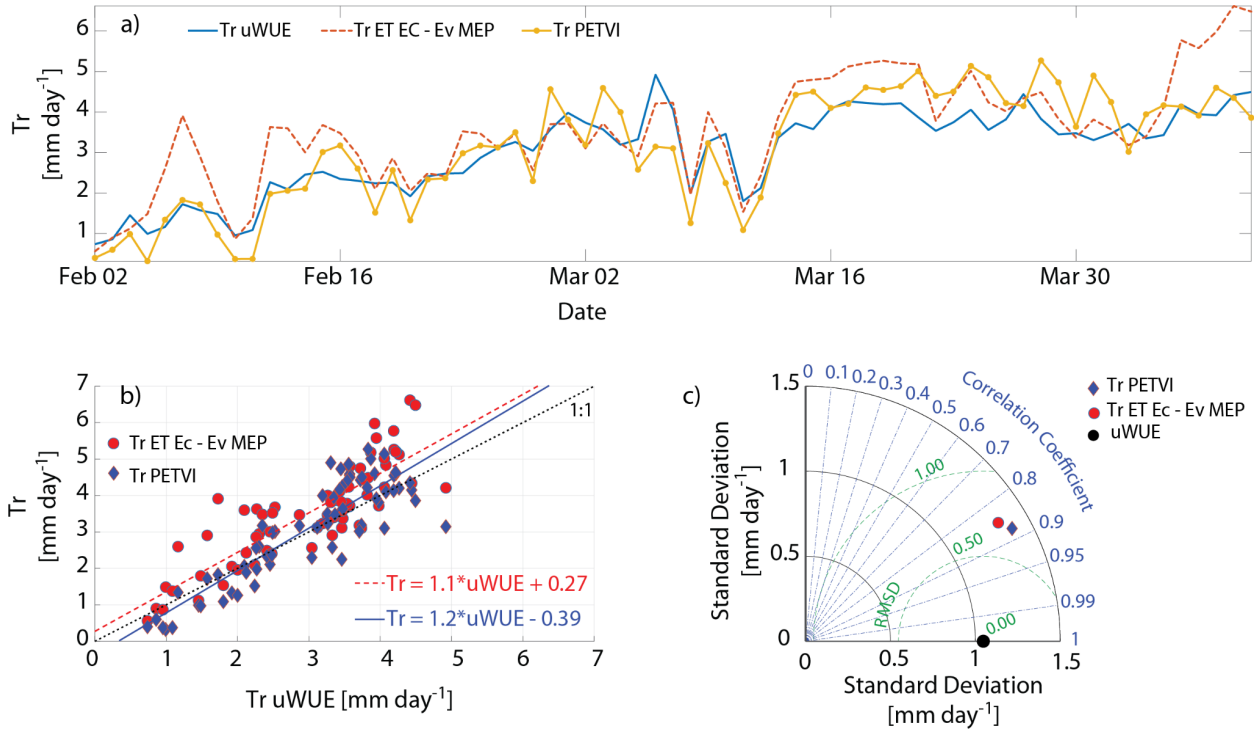

Figure 2.8 a) Transpiration time series obtained with the underlying water use efficiency method (uWUE; blue line), as residual from Eddy covariance Evapotranspiration and soil evaporation calculated with Maximum Entropy Production (ET_{EC} - Ev_{MEP}; red dashed line), and with the PETVI method ($T_{r\ PETVI}$; yellow line); b) Scatter plot of the transpiration calculated with the uWUE method (x-axis) and $T_{r\ PETVI}$ and Tr ET_{EC}-Ev_{MEP} (y-axis); c) Taylor diagram displaying the correlation coefficient, standard deviation and root means square difference between the modeled transpirations (Tr ET_{EC}-Ev_{MEP} (red circle) and $T_{r\ PETVI}$ (blue diamond)) and the reference transpiration ($T_{r\ uWUE}$ (black circle)); green dashed lines represent the root mean square difference (RMSD) in mm.

2.3.8 Performance of PETVI transpiration using high-resolution images ($T_{r\ PETVI(HR)}$)

In this work we evaluated if images of vegetation indices with higher spatial resolution can increase the precision in estimating transpiration at the sub-meter scale (<1m^2). To do this analysis, we obtained average transpiration rates with the *PETVI* method using drone images through a

buffer analysis of a 5 cm radius around the point where the instruments were installed to compare it to a point-scale estimate of T_r from the residuals of ET_{EC} and Ev_{MEP} . The temporal behavior of transpiration is shown in Figure 2.9, with the observation period of the drone images from February 15 to March 28, 2019. During the observation period, all methods follow the same trajectory with slight discrepancies among them at different times. $T_{r\ PETVI(HR)}$ ranged from a minimum of 1.19 mm day^{-1} and a maximum of 6.11 mm day^{-1}; with this method cumulative transpiration for the observation period was 161.57 mm. The $T_r\ ET_{EC}$-Ev_{MEP} ranged from 1.53 to 5.26 mm day^{-1}, and their cumulative values were recorded at 154.53 mm, while the $T_{r\ PETVI}$ ranged from 1.08 to 5.26 mm day^{-1}, and had cumulative transpiration of 144.69 mm. Finally, the transpiration from *uWUE* ranged from 1.80 to 4.92 mm day^{-1}, and the cumulative transpiration yielded a total of 138.76 mm for the observation period. The main differences among the methods can be observed in the maximum and cumulative values (Figure 2.8 b). Tr $_{PETVI(HR)}$ agrees well with the observed values when transpiration is less than 3.5 mm day^{-1}. As transpiration rates increase, there is more dispersion in the data from a tendency of the methods to overestimate $T_{r\ uWUE}$. On the other hand, $T_r\ ET_{EC}$-Ev_{MEP} shows a good correlation relative to $T_r\ uWUE$ (0.83). In this analysis $T_{r\ PETVI}$ using *S-2* images agrees well with the reference values ($T_{r\ uWUE}$), but similar to the other estimates the values begin to disperse after T_r>3.5 mm day^{-1}, although with a lower dispersion than $T_{r\ PETVI(HR)}$. A Taylor diagram shows an intercomparison between the observed values and modeled transpiration (Figure 2.8 c). The diagram shows $Tr\ ET_{EC}$-Ev_{MEP} agrees best with the reference values, displaying a standard deviation of 0.83 mm day^{-1}, and a *RMSD* of 0.54 mm day^{-1} and a correlation coefficient of 0.8; $T_{r\ PETVI}$ shows a standard deviation of 0.76 mm day^{-1}, an *RMSD* of 0.72 mm day^{-1}, and a correlation coefficient of 0.76; $T_{r\ PETVI(HR)}$ registered a standard deviation of

0.76 mm day^{-1}, a *RMSD* of 0.87 and correlation coefficient of 0.76. In this analysis all metrics show *Tr* ET_{EC}-Ev_{MEP} closer to the reference data.

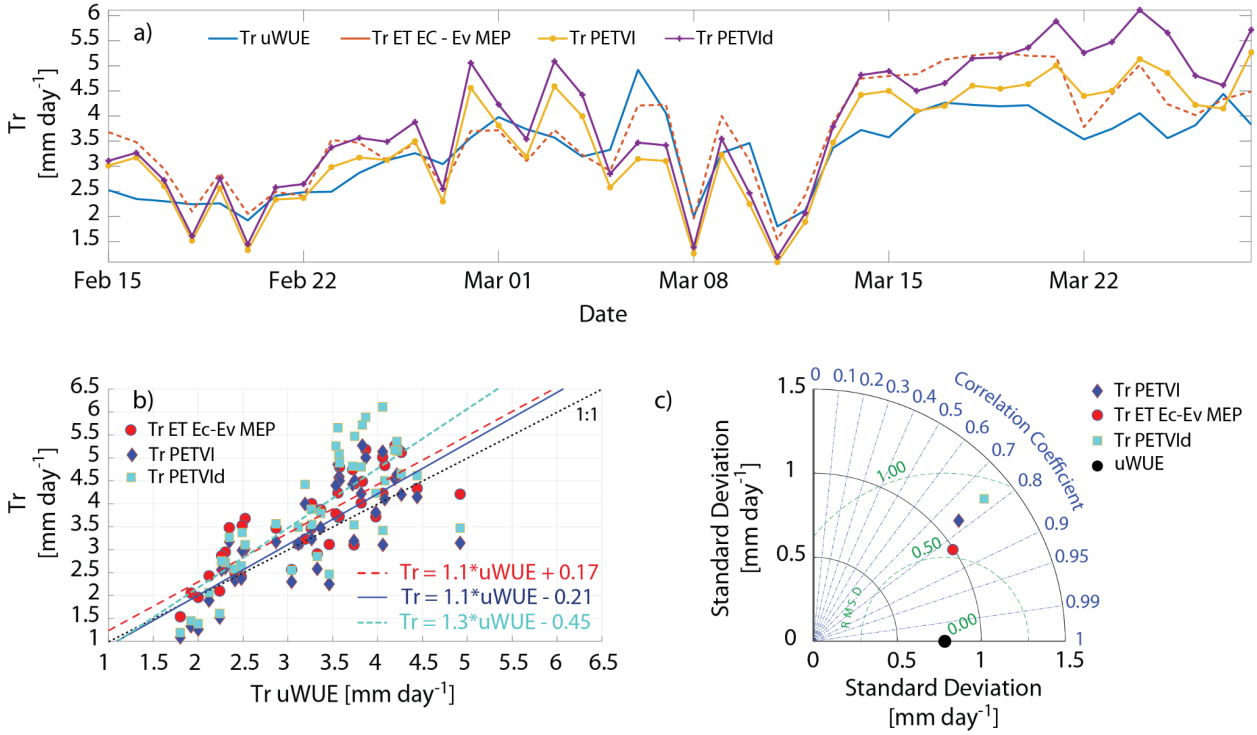

Figure 2.9 a) transpiration time series calculated with the underlying water use efficiency (uWUE; blue line) method, as residual from Evapotranspiration from Eddy covariance system and soil evaporation from the Maximum Entropy Production method (T_r = ET_{EC}-Ev_{MEP}; r red dashed line), and with the proposed PETVI method using S-2 images ($T_{r\ PETVI}$; yellow line), and high spatial resolution images ($T_{r\ PETVI(HR)}$; purple line); b) scatter plot comparing $T_{r\ PETVI}$ (blue diamond), $T_{r\ PETVI(HR)}$ (cyan squares), and Tr ET_{EC}-Ev_{MEP} (red circles) versus reference data from the uWUE model; c) taylor diagram displaying the correlation coefficient, standard deviation and root mean square difference between the modeled transpirations (T_r ET_{EC}-Ev_{MEP} (red circle), $T_{r\ PETVI}$ (blue diamond), $T_{r\ PETVI(HR)}$ (cyan squares)) and the reference transpiration ($T_{r\ uWUE}$ (black circle)); green dashed lines represent the root mean square difference (RMSD) in mm.

2.3.9 Evaporation

2.3.10 Evaporation MEP (E_v-*MEP*) & Evaporation PETVI (E_v-*PETVI*)

The behavior of soil evaporation estimated with the *MEP* method (Ev_{MEP}), as a residual of ET_{EC} - T_r *uWUE* (Ev_{uWUE}), and as a residual of ET_{METRIC} - T_{rPETVI} (Ev_{PETVI}) is shown in Figure 2.10. Initially, the three methods show relatively high evaporation values (in one case of up to 0.9 mm day^{-1}) due to a larger fraction of exposed soil and a smaller fraction of vegetation cover. The estimates from different methods show a slight separation among them at the beginning of the observation period from the 2nd to the 16th of February. This separation appears to be systematic between models. After this period the three evaporation estimates converge until the end of the observation period (April 5th) when Ev_{uWUE} separates from Ev_{MEP} and Ev_{PETVI}. This behavior can be observed in Figure 2.10 a, where both models, Ev_{MEP} and Ev_{PETVI} are consistently estimating soil evaporation of less than 0.15 mm day^{-1} while Ev_{uWUE} estimates grow to 0.43 mm day^{-1}. Figure 2.9 c shows a Taylor diagram comparing the standard deviation, correlation coefficients and *RMSD* of the reference values (*uWUE*) with those obtained from *PETVI* and Ev_{MEP}. Ev_{PETVI} standard deviation was recorded at 0.13 mm day^{-1}, with a correlation of 0.8, and RMSD of ~0.13 mm day^{-1}, the Ev_{MEP} standard deviation was 0.11 mm day^{-1}, had a correlation coefficient of 0.74 and a *RMSD* of 0.12 mm day^{-1}. Overall, the methods show reasonable agreement when considering the high correlation coefficients between Ev_{PETVI} and Ev_{MEP} with Ev_{uWUE} (the reference).

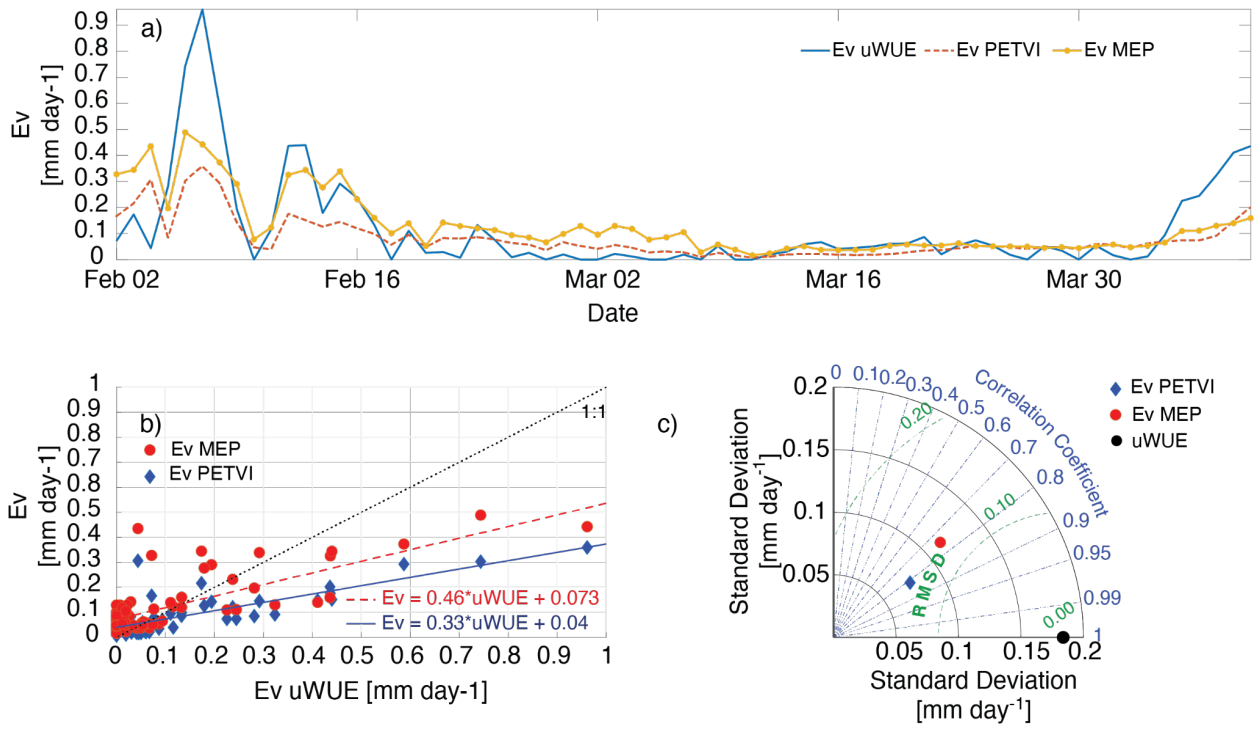

Figure 2.10 a) Soil evaporation time series calculated with the uWUE method (blue line), as the residual of the Evapotranspiration from the METRIC algorithm (ET_M) and transpiration through the PETVI method (T_{rPETVI}; dashed red line), and from the Maximum entropy pro production model (Ev_{MEP}; yellow line); b) scatter plot of the reference evaporation obtained from the uWUE against the evaporation calculated with the Ev-MEP (red circles), and the Ev_{PETVI} (blue diamond); c) Taylor diagram displaying the correlation coefficient, standard deviation and root mean square difference between the modeled evaporations (Ev ET_{EC}-Tr_{MEP} (red circle), Ev $_{PETVI}$ (blue diamond), and the reference evaporation (Ev $_{uWUE}$ (black circle)); green dashed lines represent the root mean square difference (RMSD) in mm.

The analysis of evaporation using high-resolution images shows the trajectory of soil evaporation, between reference values from the E_{vuWUE} method (Figure 2.11 a). The minimum E_v value was 0, the maximum 0.29 mm day^{-1}, and the cumulative E_v for the observation period was 1.99 mm. The evaporation through the Ev_{PETVI} method using *S-2* images, showed a minimum value of 0.007 and a maximum of 0.14 mm day^{-1}. The cumulative soil evaporation was recorded at 1.98

mm. Soil evaporation using the *MEP* method, the minimum value was 0.01, the maximum value is 0.33 mm day^{-1}, the cumulative values recorded using this method during this period was 3.55 mm, the *Ev using* high-resolution images (*Ev PETVId)* method, the minimum values were 0, and the maximum values were recorded at 0.17 mm day^{-1}, the cumulative soil evaporation during this period was 0.94 mm, the latest method recorded less water than other. Figure 2.11 b), shows the scatter plot to observe the pattern of three methods compared with reference values *uWUE*, in this panel, we can see that the *Ev-MEP* adjust best with respect to *uWUE* with a slope of 0.7, the *PETVI* method using *S-2* images and high-resolution images the slope are 0.36 a that detracts their performance. The above can be confirmed by the Taylor diagram, Figure 1.11 c) shows the statistical pattern to evaluate the performance of the three models used in this work. The standard deviation of the *Ev-PETVI* was 0.03 mm day$^{-1,}$ the *RMSD* was recorded at 0.044, and the correlation coefficient was 0.70, the soil evaporation from *Ev-MEP* the standard deviation was recorded at 0.05 mm day^{-1}, the *RMSD* was 0.045 their correlation coefficient was 0.70, and the performance of the using high-resolution images *Ev-PETVId* their performance decrease a little bit compared with the two methods described above. This confirms that during this period, the *Ev-MEP* agrees well concerning the reference values *uWUE*.

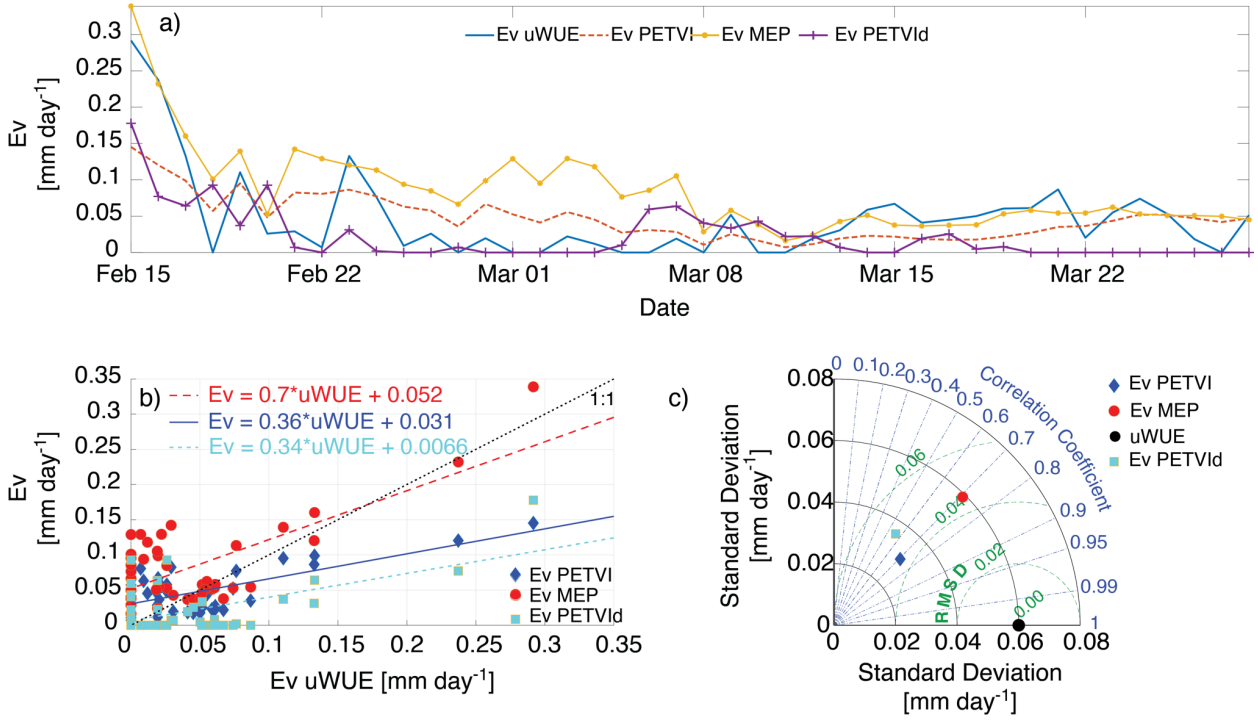

Figure 2.11 a) Soil evaporation time series calculated with underlying water use efficiency (uWUE; blue line) as residual from Evapotranspiration from Eddy covariance system and transpiration using uWUE, and soil evaporation with the proposed PETVI method using S-2images (red dashed line), and Ev-$_{MEP}$ (yellow line), and high spatial resolution images Ev $_{PETVI(HR)}$ b) scatter plot comparing Ev$_{PETVI}$ (blue diamond), EvMEP (red circles), Ev $_{PETVI(HR)}$ (cyan squares), versus reference data from the uWUE model; c) Taylor diagram displaying the correlation coefficient, standard deviation, and root mean square difference between the modeled evaporation (Ev$_{PETVI}$ ET$_{EC}$-Tr$_{PETVI}$ (blue diamond), Ev$_{MEP}$ (red circle), Ev $_{PETVI(HR)}$ (cyan squares)) and the reference evaporation (Ev $_{uWUE}$ (black circle)); green dashed lines represent the root mean square difference (RMSD) in mm.

2.3.11 Spatial analysis of the evaporation and transpiration dynamics with high and moderate spatial resolution imagery

2.3.12 Evaporation and Transpiration using *PETVI* method and high-resolution UAV imagery.

High-resolution images of vegetation indices used in *PETVI* produce detailed spatial patterns with high definition of the contrasting rates of evaporation (E_v) and transpiration (T_r) within the experimental plot. Figure 2.12, shows the evolution of the spatial variability of E_v and T_r with high resolution (5cm pixels) images during the growing season in the study site for the dates the UAV was flown. These images show an increasing (decreasing) proportion of pixels with T_r (E_v) as the crop develops and reaches its maximum cover on the last days of March. The images also show higher E_v on the northern portion of the plot, where vegetation cover took longer to develop. Probability density functions (PDFs) of the images (Figure 2.12.a3, b3, c3, d3, e3, and f3) show the ranges and distribution of T_r and E_v values for each scene. The PDFs show increases in T_r magnitudes as the crop developed, from a mean 4 mm day^{-1} in mid February to a 6 mm day^{-1} mean in late March, while E_v value ranges and means remain relatively constant throughout the season with the exception of the last image in March, where the distribution of soil evaporation concentrates below ~1 mm day^{-1} values. In all images the increases shown in the T_r rate of the PDFs appear to be directly proportional to increases in vegetation cover.

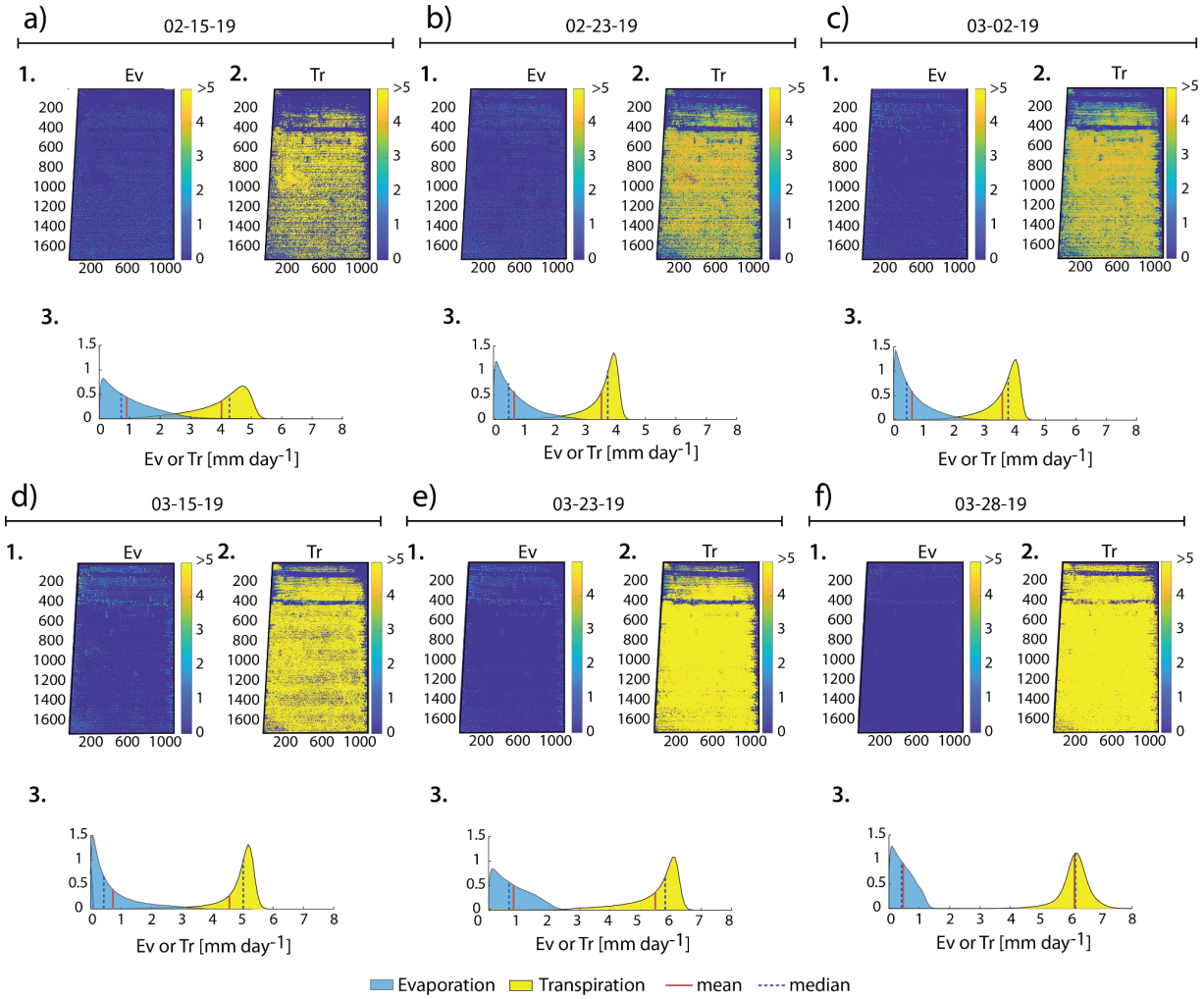

Figure 2.12 Spatial distribution of evaporation (Ev) in mm day-1 as a residual of ET_{EC} - $_{Tr\ PETVI(HR)}$*; transpiration (Tr) in mm day*$^{-1}$*, and the probability density functions (PDFs) for Ev and* T_r *for a) February 15, 2019; b) February 23, 2019; c) March 02, 2019; d) March 15, 2019; e) March 23, 2019; and f) March 28, 2019.*

2.3.13 Evaporation and Transpiration using PETVI method and Sentinel 2 images.

Satellite imagery with relatively high spatial (<30m) and temporal (<5 days) resolution can be useful for monitoring the evolution of vegetation growth cycles and particularly those of irrigated crops. In this work, we used satellite imagery for monitoring the *Ev* and T_r. using S-2

images and Landsat 7 and 8 derived ET_a. Similar to Figure 2.12, shows the evolution of the spatial variability of *Ev* and T_r during the growing season in the study site but in this case produced with S-2 imagery at 10m spatial resolution. Overall, the scenes in Figure 2.13 capture the same spatial patterns and magnitudes of T_r of those produced with the *UAV* generated imagery, where the northern region of the plot shows the lowest fluxes. However, and although E_v spatial patterns of S-2 are also similar to those of the *UAV*, their magnitudes and range of values differ; S-2 derived E_v shows higher means and a wider spread of soil evaporation than the higher resolution data throughout the whole observation period. For example, the mean E_v in early February was 1.25 mm day^{-1} with those values appearing in the north and south of the experimental site where the area has less vegetation cover than in the middle of the experimental site. 10 days later (February 26, 2019), the *Ev* mean was 1.32 mm day^{-1} and in mid March (18^{th}), soil evaporation increased relative to the earlier dates. At this time, the *Ev* recorded 1.92 mm day^{-1}. In the last date shown, (March 28, 2019), the mean *Ev* was 1.31 mm day^{-1}. It was also at this time when T_r showed the largest values during the study period; the mean T_r was 6.09 mm $day^{-1,}$ and coincidentally was the most frequent value as well.

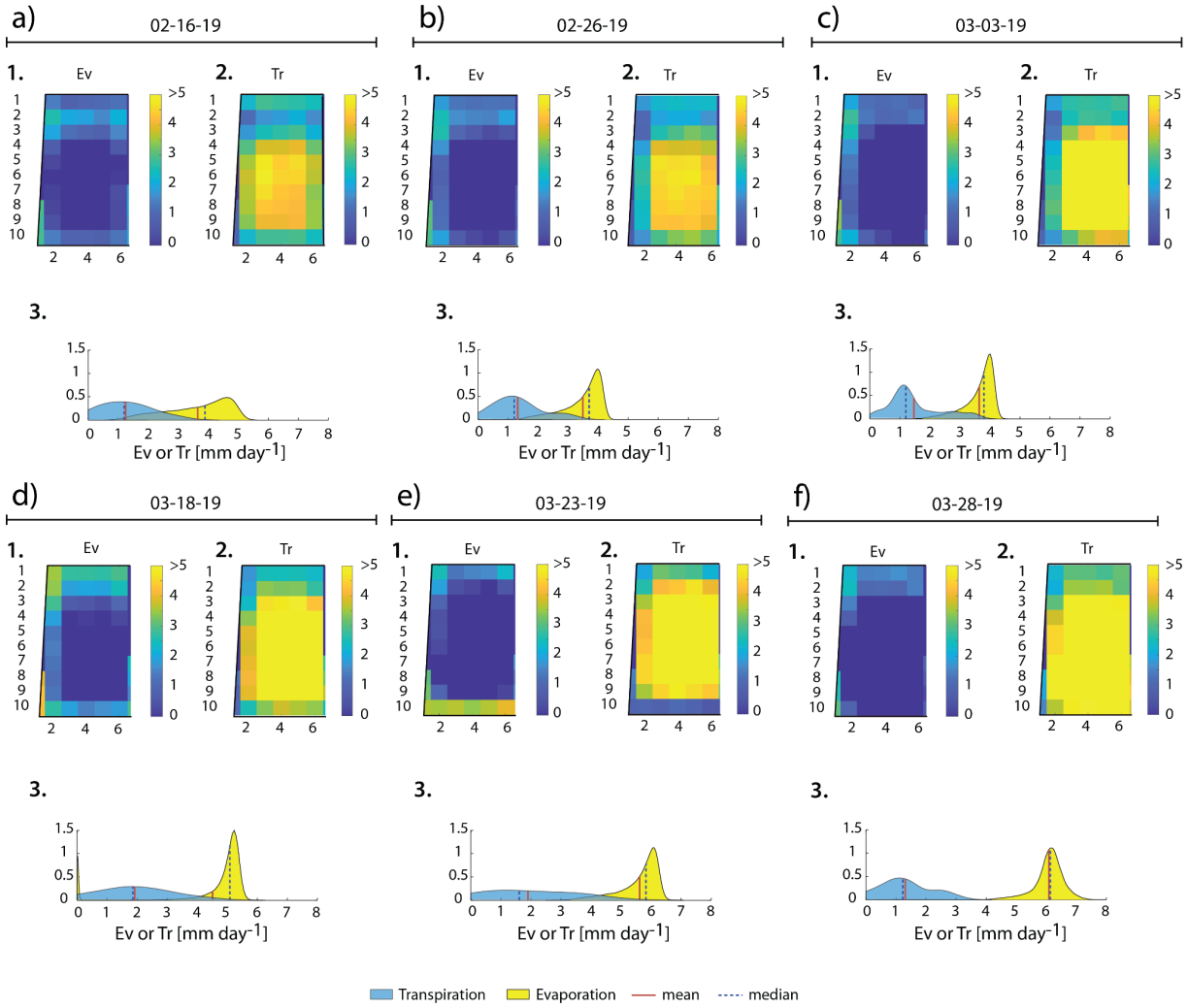

Figure 2.13 Spatial analysis of Ev as a residual of ET_{METRIC} - T_{rPETVI} using S-2 images with spatial resolution of 10 m per pixel for 6 dates within the observation period (panels a to d). Subpanels 1,2 and 3 show the spatial patterns on Ev, T_r and their probability density functions (PDFs) within the experimental plot respectively. Subpanels 1,2, and 3 show the spatial patterns on Ev, T_r and their probability density functions (PDFs) within the experimental plot respectively.

It has been shown that evaporation and transpiration from PETVI can be estimated at different spatial resolutions by changing the resolution of the input data on vegetation phenology and cover. However, to allow for a more direct comparison between spatial resolution products, we show in Figure 2.14 high (*UAV* 5 cm pixel) and moderate spatial resolution (S-2 10 m pixel)

E_v and T_r images and their PDFs for the only two coinciding dates for the images (i.e. 23 and 28 of March, 2019). The images on the 23 of March show relatively moderate evaporation areas in the north of the experimental site, but only the lower resolution image shows high evaporation values on the south side, stretching the distribution of Ev values on the PDF (Figure 2.13.c.3). Seven days later, the images on the 28th of March show a more similar E_v and T_r pattern, where moderate E_v values appear on the northern portion of the plot and in the left edges on the S-2 derived images but not on the southern edge anymore. Those differences in E_v between the high and moderate resolution images appear to be caused by contamination of the spectral signatures defining the vegetation indices on the southern and eastern edges of the plot, and are responsible for changing the means and distribution of E_v values between images. On the other hand, the means and ranges of T_r values between the *UAV* and S-2 derived images remain fairly similar for the two dates compared: the mean and median T_r values of the S-2-derived images were 5.62 and 5.86 mm day^{-1}, while the mean and median T_r of the *UAV*-derived images were 5.48 and 5.81 mm day^{-1} respectively.

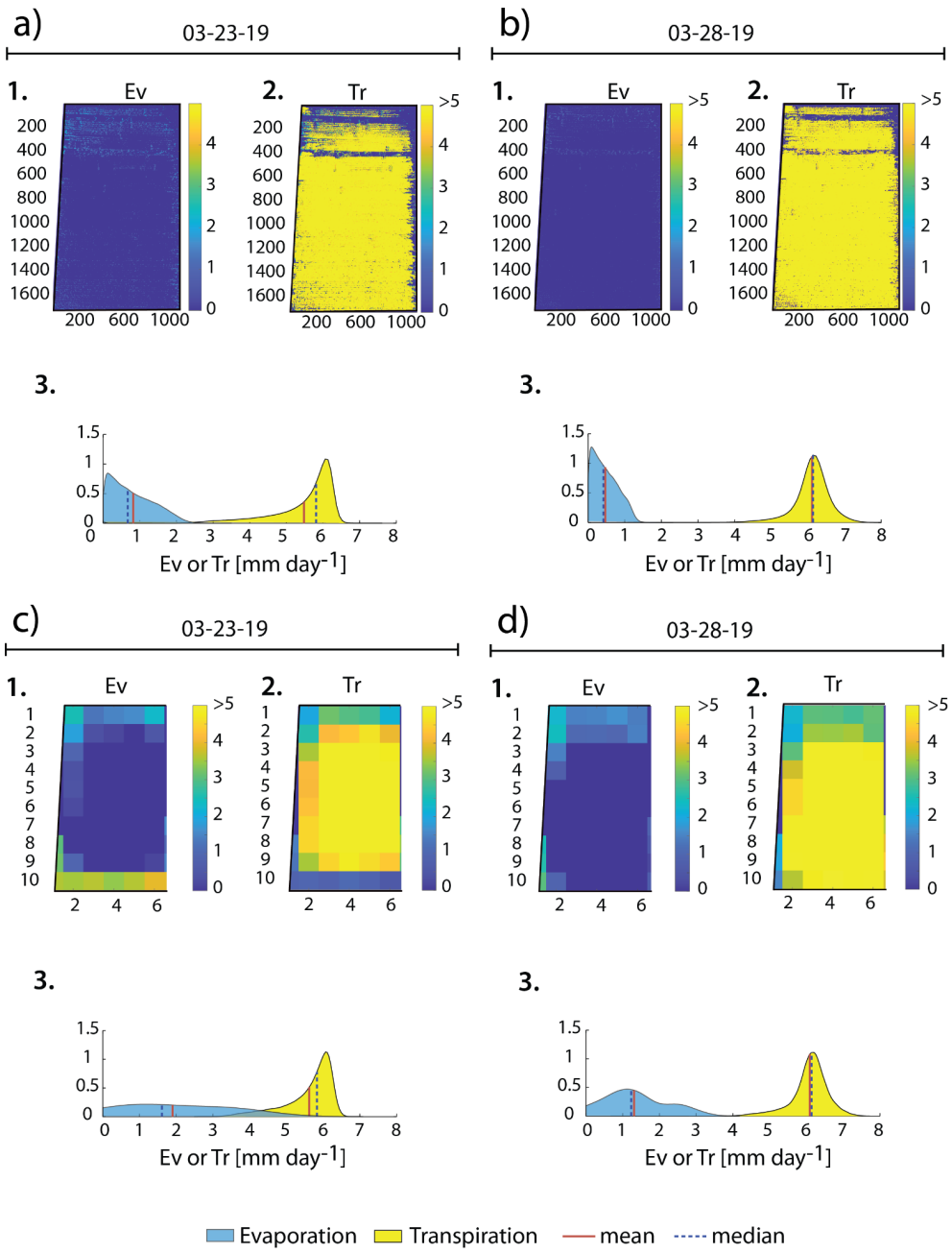

Figure 2.14 Effects of spatial resolution (5 cm per pixel and 10 m per pixel) on Ev and T_r (in mm day- 1) calculated from PETVI; a) and b) show UAV derived images from March 23, 2019 and March 28, 2019 respectively; c) and d) show S-2 derived images on March 23, 2019 and March 28, 2019, respectively. Subpanels 1,2, and 3 show the spatial patterns on E_v, T_r and their probability density functions (PDFs) within the experimental plot respectively.

2.3.14 Water balance at the plot scale

The surface water balance approach was applied to our study site to monitor the partition of water fluxes between the land surface and the atmosphere. The partition of ET_a into soil evaporation (Ev) and plant transpiration (T_r) is a requirement to understand carbon assimilation and water use by agro-ecosystems. As shown in figure 2.15 a) ET_a is almost all composed of soil evaporation at the beginning of crop cycle (December and January) due to scarce vegetation cover. However, T_r dominance started to switch in late January-early February, consequently steadily increasing the ratio T_r/ET_a until both crop development and ET_a reached its maximum seasonal values which occurred in Mid to late March. Conversely, when crop senescence started in mid-April, the rate of T_r values began to diminish, consequently, the ratio T_r/ET_a started to decrease. The minimum value of T_r during the crop cycle was 0.01 mm day^{-1} observed after planting, while the maximum value was 6.15 mm day^{-1} observed during the peak of vegetation development. During the observation period (February-April), T_r closely tracks the evolution of ET_a with the exception of the beginning of the agricultural cycle (mostly soil evaporation, E_v), with a cumulative value of 86.66 mm which represented the 39 % of the irrigated water returned to the atmosphere (unproductive water) while the remaining 61 % stored in the soil profile. The other period where evaporation comprises the majority of ET_a occurred from April 2 to May 20 when the crop was in transition between milk to dough grain and close to physiological maturity resulting in a decrease in crop water demand. Cumulative evaporation (E) during this phenological stage was 84 mm which is equivalent to 56 % of the water applied in the last auxiliary irrigation (April 5). Total ET_a during this analysis was 501 mm and ranged from 0.04 to 6.42 mm day^{-1} with an average of 2.51 mm day^{-1}. Cumulative rainfall during the crop cycle was 14.9 mm with three auxiliary irrigations. The evolution of productive water use (Transpiration, T_r) shows that most of these fluxes occurred

during two periods (Figure 2.15 c). The first period encompassed 102 days since planting through February 19 with a total of 75.9 mm of productive water use while the second period included the rest of the crop cycle with a cumulative T_r *of* 271 mm. One way to assess the efficiency of crop irrigation is by using the surface water balance approach that is shown in Figure 2.14 d. The pre-sowing irrigation (applied in November 2018) supplied water until the 1-m soil profile reached 146 mm of water content which was rapidly depleted to 91 mm in about 37 days. The irrigation at the sowing (applied in December 2018) increased water content until 159 mm with an additional water input from rainfall of 4.7 mm that was steadily depleted in about 48 days. Before the application of the first auxiliary irrigation, the water content was 116 mm, but after its application, the water on the 1-m soil profile increased to 265 mm and was steadily depleted during a period of 28 days. Before the application of the second auxiliary irrigation, the water content in the 30-cm soil profile was 183 mm, but after its application, the water content rapidly increased to 330 mm that was steadily depleted for 27 days. Finally, the water content before the third auxiliary irrigation was 200 mm and after its application water content increased up to 345 mm indicating that at the end of the study period, the system gains water. Soil moisture dynamics at 30-cm depth behaved similar to those observed at the 30-cm soil profile (Figure 15e). The water content before the first auxiliary irrigation was 44 mm but after its application water content increased to 105 mm and it steadily decreased during the following 28 days. A second auxiliary irrigation was applied and the water content increased to 103 mm, 28 days after the water content decreased until 48 mm at this time the last auxiliary irrigation was applied, and this increased the water content to 97 mm. Figure 2.14 f) and g) display the proportion of the different water balance components at the plot, showing that 98% of the water inputs came from irrigation and only 2% came from rainfall, that

40 % of the water delivered turned to T_r (productive water use) and 34% turned to E_v (unproductive water), while the remaining 27% of the left the plot as either runoff or percolation.

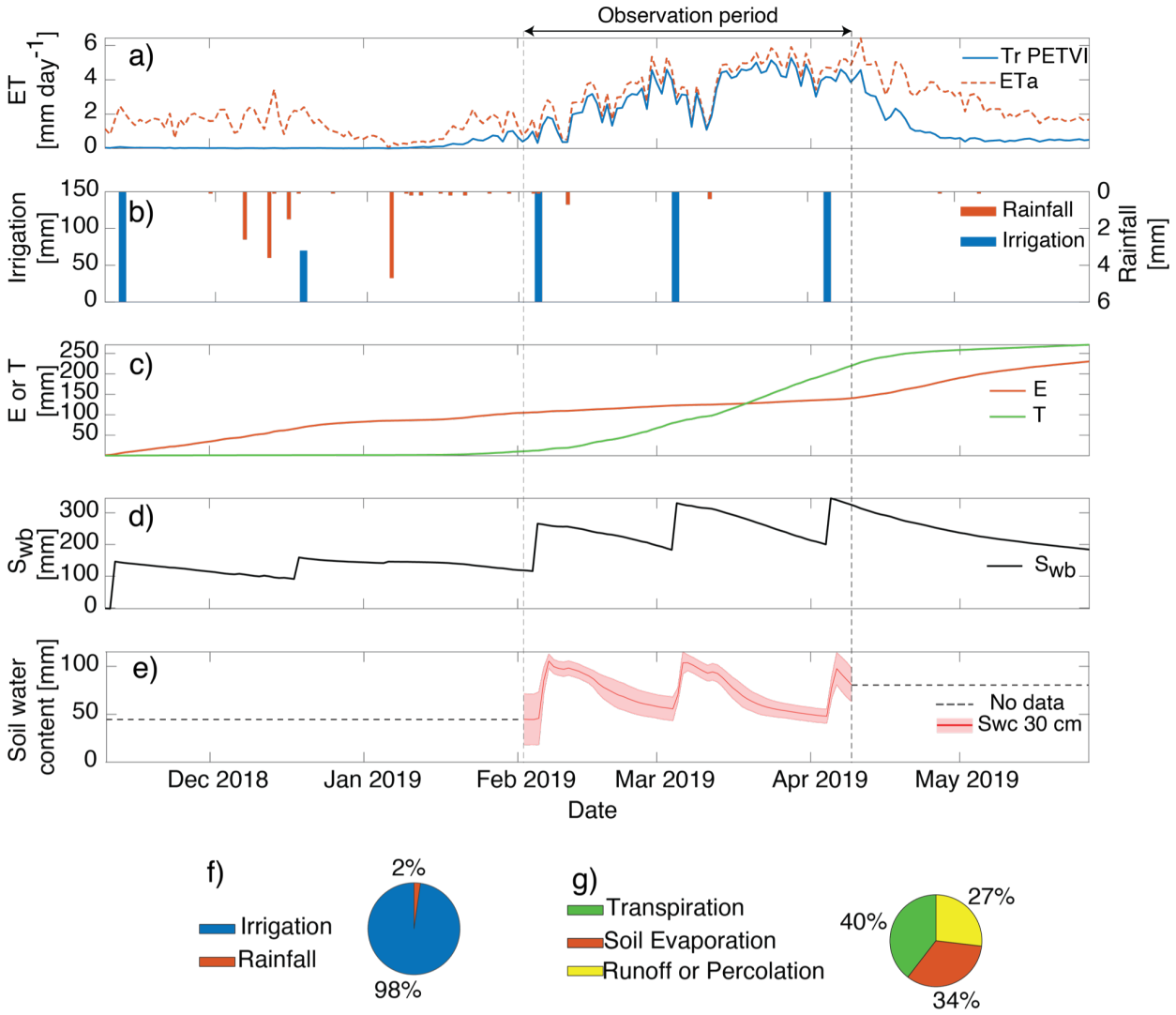

Figure 2.15 a) Temporal dynamics of Evapotranspiration (ETa) from METRIC (dashed red line) and Transpiration (Tr) from PETVI (blue line); b) water inputs at the experimental site showing irrigation (blue bars) and rainfall events (red bars); c) cumulative Evaporation (Ev, red line) and Transpiration (T_r, green line); d) time series of the surface water balance (inputs - outputs); e) dynamics of soil moisture content (red line) during the observation period where the dashed black line indicates the absence of data before and after the observation period; f) proportion of rainfall and irrigation on the plot; g) proportion of T_r, Ev and runoff or percolation on the plot.

2.4 Discussion

2.4.1 PETVI depends on the vegetation index

In our PETVI approach, we use a vegetation index to perform two functions: 1) to parameterize the development of the phenological evolution of the crop and its influence on its transpiration rates through the $K_{cb,}$, and 2) to estimate the vegetation fractional cover of the crop. Thus, the degree of uncertainty or accuracy on the resulting T_r estimates from *PETVI* and the evapotranspiration partitioning will depend on the performance of the chosen vegetation index to realize those two functions. To address those issues, we evaluated three vegetation indices to estimate K_{cb} and transpiration (T_r) using PETVI: the Normalized Difference Vegetation Index (*NDVI)*, the Modified Soil Adjusted Vegetation Index (*MSAVI*), and the Enhanced Vegetation Index (*EVI)*. When comparing the resulting T_r obtained with each index to the reference T_r from the underlying Water Use Efficiency method (*uWUE*), all three had similar performance; close to identical r^2 and slopes although *MSAVI*, had the lowest RMSD closely followed by *NDVI* and *EVI* (Figure A). In this work, we used *NDVI* to test and validate the T_r generated with PETVI for two reasons: 1) it showed a similar performance to the T_r calculated with *MSAVI*, and better performance than T_r from *EVI*, and 2) because from the three indices *NDVI* is the most widely used vegetation index (Huang et al., 2021), it is frequently available as a custom estimate from *UAV* imagery post-processing software and remote sensing data gateways and is the easiest index to obtain with ground measurements using handheld multispectral cameras (Kharrou et al., 2011). The *NDVI* has been used to calculate the cover fraction in various crops; Tenreiro et al., (2021) validated the cover fraction of 13 crops (including wheat) using *NDVI*, and their results showed good agreement between the fractional cover estimated using *NDVI* and the fractional cover

measured on the ground to calibrate hydrological models. Also, Goodwin et al., (2018) investigated estimating wheat yield using *NDVI* and vegetation fraction. They found a linear relationship between crop yield with increasing *NDVI* and cover fraction. On the other hand, Drerup et al., (2017) used *NDVI* to estimate K_{cb} in a wheat crop finding a close relationship between the increase in the *NDVI* value and a higher transpiration rate of the wheat. Similarly, Kharrou et al. (2011) used *NDVI* to derive K_{cb} and wheat crop cover fraction in a semi-arid region; their results suggest that incorporating NDVI to derive K_{cb} provides the opportunity to improve the water demands of the crop. The above-mentioned works, evidence the adequacy and robustness of *NDVI* in reflecting crop growth and fractional cover and provide confidence in its use within *PETVI*.

2.4.2 Partitioning of water flux using two digital products Sentinel 2 and UAV images

This study demonstrated the use of two images with different spatial resolutions to make the partitioning of Evapotranspiration: *UAV*-derived images, and Sentinel-2 images. High spatial resolution scenes used in croplands are helpful for accurately monitoring the water transfer from land surface to the atmosphere, and that has an important application in precision agriculture. Monitoring the productive and nonproductive water is essential to save water in agricultural practices. The estimation of soil evaporation in croplands using *UAV* images increases the accuracy of calculating the soil evaporation, and this is possible due to the more precise separation of the soil and vegetation and the reduction or elimination of edge effects. On the other hand, the calculated values using S-2 images keep the variability of the soil evaporation values due to edge effect and pixel mixing. The difference is due to the pixel size between *UAV* and Satellite images

(Mengmeng et al., 2017). This strengthens the behavior described in Figure 2.12. Where we can see the soil evaporation appear in the north and south sites of the experimental site. This pattern is due to the size of the pixels from S-2. At the same time, the *UAV* images show the little pixels that show soil evaporation on these two dates (March 23 and 28, 2019, Figure 2.12) due to vegetation cover being almost complete and reducing the soil exposure and evaporation (Nieto et al., 2019). However, both resolution images work well to estimate the T_r using the *PETVI* method, with *UAV* images showing a good correlation ($R^2 = 0.77$) between observed and measured data.

On the other hand, the calculation of T_r using the *PETVI* method and S-2 images show a correlation coefficient of 0.70. These values are comparable with those found by Hou et al., (2021) in which correlations around (R^2 0.84) of observed and estimated transpiration values using *UAV* thermal images compared with the eddy covariance system in desert conditions and two crops corn and soybean. We found that the values of mean T_r at the end of March were 6.14 mm using *UAV* images and 6.09 mm using S-2 images. These values can be compared with the maximum T_r values found by (Duchemin et al., 2006) at the end of March 2003 T_r values from 2 to 6 mm with a mean of 4.17 mm. Duchemin et al., attribute this variability to the different sowing dates on the study site. Satellite images such as those from S-2 can help us monitor large cropland areas at a low cost to monitor the trajectory of T_r to adjust irrigation scheduling and increase the efficiency of irrigation.

2.4.3 Crop water use changes at different phenological stages

The water used by the crop during the growing season increased gradually, modulated by the phenology stage and weather conditions. The initial trajectory of T_r is tightly coupled to the green-up of the vegetation. Our results (Table 3) yield comparable values to those of Gómez-Candón et

al. (2021) who studied a wheat crop using *UAV* images and an energy balance method to calculate the T_r values on three phenological stages as follows: at jointing the average T_r was 2.45 mm day^{-1}, anthesis T_r was 4.45 mm day^{-1}, and Grain filling T_r was recorded 5.47 mm day^{-1}. Discrepancies between this work and theirs can be attributed to different weather conditions and agronomic practices, but the overall trends of the values also closely follow the change of phenological stages. T_r from *PETVI* is based on following vegetation activity through a vegetation index based on chlorophyll reflectance, as a proxy for photosynthesis and transpiration. This can be affected by weather conditions, but also by soil water availability. During the observation period, T_r increased with each phenological stage until the milk grain stage, and then steadily decreased. During its upward trajectory, T_r shows some inflections (dips) associated to changes in the weather conditions and particularly to attenuation of the net radiation by rainfall and overcast conditions..

2.4.4 Environmental conditions and dynamics of water transfer and soil moisture

Plant transpiration is affected by environmental conditions and soil moisture. During the observation period, T_{rPETVI} using S-2 images and T_{rPETVI} using *UAV* images varied in the range 0.32 to 5.26 mm day^{-1} and 1.19 to 6.11 mm day^{-1} with means of 3.12 - 3.84 mm day^{-1} respectively. These T_r values increase as vapor pressure deficit (*VPD*) increases. Because *VPD* is a function of temperature and relative humidity, it reflects humidity or dryness of the study area. Low T_r values coincided with low *VPD* values. The *VPD* values were recorded as 0.38, 0.52, 0.36 kPa. In our study, the low *VPD* values occur during rainy events and cloudy conditions. However, the soil moisture in those days was high (84 mm of water) and close to field capacity (F_C) so this means

that T_r was low due to energy limitations. On the other hand, water transfer to the atmosphere by T_r increases linearly with *VPD* values >1 kPa as it has been shown in other well-watered wheat crops (Schoppach & Sadok, 2013). Transpiration increases also and up to some point with increases in temperature. Our results show high transpiration with temperatures around 20 ℃ and high *VPD* values. Concurrently, while T_r remains high, water content decreases after irrigation events as energy in the system is available (Gourdji et al., 2012).

Table 2.3 Average daily transpiration (T_r) at each phenological stage in mm day^{-1}.

Phenology stage	T_r [mm day^{-1}]
Germination (Ge)	0.17
Growing (Gr)	0.64
Tillering (Ti)	1.37
Stem elongation (St)	2.15
booting stage (B)	2.35
Heading (H)	3.81
Anthesis (An)	2.77
Flowering (F)	3.88
grain filling (Gf)	4.95
milk grain (Mg)	4.77
dough grain (Dg)	4.40
physiological maturity (Pm)	2.25

2.4.5 PETVI Soil Evaporation

Transpiration using K_{cb} derived from vegetation indices (*VI*) is well documented in its use in monitoring the vegetation growing and basal crop coefficient (K_{cb}) (Allen et al., 2011; Calera et al., 2010; Carpintero et al., 2020; Duchemin et al., 2006; Hunsaker et al., 2005; Reyes-González et al., 2018). In this work, a *VI* was used to determine K_{cb}, which is necessary to estimate the portion ET_a belonging to T_r (Allen et al., 2011). However, the other important part is the estimation of evaporation. In our proposed method, evaporation is calculated as residual of ET_a from the METRIC algorithm minus $T_{r\ PETVI}$ using *S-2* or high-resolution images. The same idea using *EC* data was documented by (Perez-Priego et al., 2018). This relationship can be applied because the *METRIC* method, which is based on the energy-balance, has the ability to detect the portion of evaporation from bare soil (Allen et al., 2013). The time series of Figure 2.4 showing the behavior of ET_a and T_r from *PETVI*, demonstrates that the majority of evaporation happens in the early season (Chi et al., 2017). This occurs because the irrigation was delivered before the sowing date, increasing soil moisture. Subsequently, during the crop's full development, the difference between ET_a and T_r is reduced close to zero, and T_r values closely approximate those of ET_a (Ferreira et al., 2012). When the vegetation starts the senescence, the crop transpiration reduces (blue line, Figure 2.4), and the ET_a value remains above form T_r values. This probably occurs due to the difference in pixel size 10x10 m T_r (*S-2*) and 30x30 m ET_a (*METRIC*) in these last images incorporating a mix of soil and vegetation signatures (Kadam et al., 2021). The *PETVI* method can be applied using high-resolution images to partition ET_a. In this work, we tested the performance of high-resolution images to make the partitioning by the nature of the *UAV* images during the observation period. We found more details to follow the trajectory of soil evaporation and transpiration (Figure 2.10, panel 3). So far, the *PETVI* model can be used with different image resolutions. However,

with some limitations in the case of S-2 it is possible to make this analysis at a plot scale and in vast areas of irrigation croplands with reasonable accuracy. On the other hand, using high-resolution images increases the plot scale's detail to monitor the unproductive water.

2.4.6 Utility of PETVI method

The parsimony of the *PETVI* method for partitioning ET_a provides some advantages over other more complex methods, as it requires relatively minimal parameterization. The main data inputs are multispectral satellite images from *S-2* and Landsat 7 and 8, that now can be processed using cloud computing such as GEE (https://earthengine.google.org/). GEE has reduced the time and cost related to image processing (Stromann et al., 2019), and allows computing of E_v and T_r fluxes of large areas while remaining suitable for relatively detailed spatial analysis of crop parcels (<1ha). There is, however, the need for specialized programming knowledge and background in remote sensing to perform these analyses, but the implementation of routine algorithms into application programming interfaces (APIs) can readily facilitate the reproduction of these computations for specific areas or crops (Gorelick et al., 2017). To estimate T_r, meteorological data needed to calculate the reference evapotranspiration (ET_0) is required. Ideally, data from weather stations surrounding the study area can supply this information, but in the absence of local meteorological data, reanalysis products can be used (Dhungel et al., 2020; Pelosi & Chirico, 2021). One of the most important steps in correctly estimating the partition of evapotranspiration is obtaining accurate crop coefficient values over the development of the crop. Using satellite derived ET_a (e.g. from METRIC or SEEBAL algorithms) together with ET_0 estimates provides a convenient avenue to back-calculate those K_c values taking advantage of the relationship between ET_0 and ET_a (Allen et al., 2007). Some of those ET_a images are freely accessible through third

party APIs supported by GEE such as the METRIC ET_a (Allen et al., 2007; https://eeflux-level1.appspot.com/), and SEBAL ET_a (Laipelt et al., 2021; https://etbrasil.org/geesebal). These two data sources of ET_a can be readily used to implement the *PETVI* algorithm (Figure 2.2). Knowing the relative contribution of T_r to ET_a in a crop parcel on a near real-time (i.e. every one or two days) basis can be a useful tool for monitoring the productive and unproductive water use to adjust irrigation timing and amounts following closely the varying daily crop water demand.

2.4.7 Tracking the water balance during the agricultural cycle

The soil water balance (*SWB*) is a useful tool for monitoring the trajectory of water transfers from the land surface to the atmosphere. From the agricultural and water conservation point of view, tracking when unproductive water use occurs can help in planning irrigation schedules and amounts to maximize T_r over E_v. In this work, the water balance shows the periods when the water enters and leaves the system and together with T_r data it is possible to determine the time the crop takes to consume that water. This information can be used for scheduling irrigation, and developing strategies for water management. For example, Pereira et al. (2020), used the calculation of a net irrigation requirement (*NIR*) as the water amount that needs to be applied in crops fields to satisfy the crop water requirement (*CWR*) occurring when the soil moisture decreases below certain thresholds based on the water balance equation. The possibilities for the application of this methodology at different spatial resolutions with the use of various remote sensing platforms (e.g. satellite and *UAVs*) might prove useful for crop water use diagnostics at different spatial scales. Other works using the water balance approach for irrigation management, provide practical examples on the applicability of these methods for water conservation efforts. For example, Li et al. (2018), documented a method to improve irrigation scheduling with average

water savings of up to 22 % using *SWB*. A study by El-Naggar et al. (2020) showed the advantages of using soil moisture data from sensor arrays deployed in the crop parcels which increased the accuracy of the *SWB* calculation used for water management.

2.5 Conclusion

The *PETVI* method can provide a viable alternative for estimating a crop's water-use trajectory during the growing cycle where information on plants' water demands can be assessed in near-real-time (every 2 or 3 days). In combination with ET_a, *PETVI* can produce images to detect the period when productive and nonproductive water use occurs in a crop. *PETVI* estimates of T_r and E_v showed good agreement with those obtained through other methods using ground-based data, providing confidence in the method. *PETVI*'s proposed approach can aid in the continuous monitoring of evaporation (E_v) and transpiration (T_r) at different scales, depending on the spatial and temporal resolutions of the input variables, as exemplified with the use of the high-resolution *UAV* imagery and moderate resolution *S-2* scenes. The use of two different spatial resolutions did not have a significant difference between T_r estimates, although E_v did show larger values for lower resolution data at the edges of the crop than those obtained with higher resolution images. This behavior shows that the *PETVI* is a competent method to estimate the T_r, while E_v estimates should be more carefully evaluated depending on the spatial resolution of the data and paying attention to any edge effects on the boundaries of the crops. Despite the current challenges inherent to the spatial resolution of the input data, *PETVI* can provide timely and cost-effective information on the productive and unproductive water use of a crop by monitoring T_r and E_v at the parcel scale (< 1 Hectare). One of the most severe limitations to using *PETVI* for estimating T_r and E_v is the availability of ET_a inputs. Most of the remote-sensing-derived ET_a data available is produced using imagery with a relatively low temporal resolution such as from Landsat 7 and 8 missions (16-day revisiting time). If low quality images such as those with significant cloud cover occur, there could be a significant gap in data inputs that might hinder accurate estimations of ET_a and K_c for producing reliable daily ET_a data. Our study shows that *PETVI* yields reasonable values

of T_r and E_v that closely follow the development of a perennial crop (wheat), and future work should include the evaluation of this approach in other annual and perennial crops under different irrigation systems and climate conditions.

2.6 References

Allen, R. G., & Pereira, L. S. (2009). Estimating crop coefficients from fraction of ground cover and height. *Irrigation Science*, *28*(1), 17–34. https://doi.org/10.1007/S00271-009-0182-Z/FIGURES/8

Allen, R. G., Pereira, L. S., Howell, T. A., & Jensen, M. E. (2011). Evapotranspiration information reporting: I. Factors governing measurement accuracy. *Agricultural Water Management*, *98*(6), 899–920. https://doi.org/10.1016/J.AGWAT.2010.12.015

Allen, R. G., Tasumi, M., & Trezza, R. (2007). Satellite-Based Energy Balance for Mapping Evapotranspiration with Internalized Calibration "METRIC…-Model. *Irrigation and Drainage Engineering*, *133*(4), 380–394. https://doi.org/10.1061/ASCE0733-94372007133:4380

António dos Anjos, L., & Cabral, P. (2021). Small dams/reservoirs site location analysis in a semi-arid region of Mozambique. *International Soil and Water Conservation Research*, *9*(3), 381–393. https://doi.org/10.1016/J.ISWCR.2021.02.002

Arreguin Cortes F, I., Garcia Villanuueva N, H., Gonzalez Casillas A., & Guillen Gonzalez A. (2018). *REFORMS IN THE ADMINISTRATION OF IRRIGATION SYSTEMS: MEXICAN EXPERIENCES †Φ*. https://doi.org/10.1002/ird.2242

Banihabib, M. E., Vaziri, B., & Javadi, S. (2018). A model for the assessment of the effect of mulching on aquifer recharging by rainfalls in an arid region. *Journal of Hydrology*, *567*, 102–113. https://doi.org/10.1016/J.JHYDROL.2018.10.009

Bhering, A. P., Antunes, I. M. H. R., Marques, E. A. G., & de Paula, R. S. (2021). Geological and hydrogeological review of a semi-arid region with conflicts to water availability (southeastern Brazil). *Environmental Research*, *202*, 111756. https://doi.org/10.1016/J.ENVRES.2021.111756

Biemans, H., Haddeland, I., Kabat, P., Ludwig, F., Hutjes, R. W. A., Heinke, J., Bloh, W. von, & Gerten, D. (2011). Impact of reservoirs on river discharge and irrigation water supply during the 20th century. *Water Resources Research*, *47*(3), 3509. https://doi.org/10.1029/2009WR008929

Bierkens, M. F. P., & Wada, Y. (2019). Non-renewable groundwater use and groundwater depletion: a review. *Environmental Research Letters*, *14*(6), 063002. https://doi.org/10.1088/1748-9326/AB1A5F

Blum, A., 2005. Drought resistance, water-use efficiency, and yield potential - are they compatible, dissonant, or mutually exclusive? Aust. J. Agric. Res. 56, 1159–1168.

Burba, G., & Anderson, D. (2010). *A brief practical guide to eddy covariance flux measurements: principles and workflow examples for scientific and industrial applications*. Li-Cor Biosciences.

Calera, A., González-Piqueras, J., & Melia, J. (2010). Monitoring barley and corn growth from remote sensing data at field scale. *Http://Dx.Doi.Org/10.1080/0143116031000115319*, *25*(1), 97–109. https://doi.org/10.1080/0143116031000115319

Carpintero, E., Mateos, L., Andreu, A., & González-Dugo, M. P. (2020). Effect of the differences in spectral response of Mediterranean tree canopies on the estimation of

evapotranspiration using vegetation index-based crop coefficients. *Agricultural Water Management*, *238*, 106201. https://doi.org/10.1016/J.AGWAT.2020.106201

Carrillo-Rojas, G., Silva, B., Córdova, M., Célleri, R., & Bendix, J. (2016). Dynamic Mapping of Evapotranspiration Using an Energy Balance-Based Model over an Andean Páramo Catchment of Southern Ecuador. *Remote Sensing 2016, Vol. 8, Page 160*, *8*(2), 160. https://doi.org/10.3390/RS8020160

Chen, Y., Ding, Z., Yu, P., Yang, H., Song, L., Fan, L., Han, X., Ma, M., Tang, X., 2022. Quantifying the variability in water use efficiency from the canopy to ecosystem scale across main croplands, Agricultural Water Management, 262.

Chi, J., Maureira, F., Waldo, S., Pressley, S. N., Stöckle, C. O., O'Keeffe, P. T., Pan, W. L., Brooks, E. S., Huggins, D. R., & Lamb, B. K. (2017). Carbon and water budgets in multiple wheat-based cropping systems in the inland pacific northwest us: Comparison of cropsyst simulations with eddy covariance measurements. *Frontiers in Ecology and Evolution*, *5*(MAY), 50. https://doi.org/10.3389/FEVO.2017.00050/BIBTEX

de Frutos Cachorro, J., Marín-Solano, J., & Navas, J. (2021). Competition between different groundwater uses under water scarcity. *Water Resources and Economics*, *33*, 100173. https://doi.org/10.1016/J.WRE.2020.100173

de Oliveira Costa, J., José, J. V., Wolff, W., de Oliveira, N. P. R., Oliveira, R. C., Ribeiro, N. L., Coelho, R. D., da Silva, T. J. A., Bonfim-Silva, E. M., & Schlichting, A. F. (2020). Spatial variability quantification of maize water consumption based on Google EEflux tool.

Agricultural Water Management, *232*, 106037. https://doi.org/10.1016/J.AGWAT.2020.106037

Drake, J.E., Power, S.A., Duursma, R.A., Medlyn, B.E., Aspinwall, M.J., Choat, B., Creek, D., Eamus, D., Maier, C., Pfautsch, S., Smith, R.A., Tjoelker, M.G., Tissue, D. T., 2017. Stomatal and non-stomatal limitations of photosynthesis for four tree species under drought: A comparison of model formulations. Agric. For. Meteorol. 247, 454–466.

Drerup, P., Brueck, H., & Scherer, H. W. (2017). Evapotranspiration of winter wheat estimated with the FAO 56 approach and NDVI measurements in a temperate humid climate of NW Europe. *Agricultural Water Management*, *192*, 180–188. https://doi.org/10.1016/j.agwat.2017.07.010

Dhungel, R., Aiken, R., Lin, X., Kenyon, S., Colaizzi, P. D., Luhman, R., Baumhardt, R. L., O'Brien, D., Kutikoff, S., & Brauer, D. K. (2020). Restricted water allocations: Landscape-scale energy balance simulations and adjustments in agricultural water applications. *Agricultural Water Management*, *227*, 105854. https://doi.org/10.1016/J.AGWAT.2019.105854

Duchemin, B., Hadria, R., Erraki, S., Boulet, G., Maisongrande, P., Chehbouni, A., Escadafal, R., Ezzahar, J., Hoedjes, J. C. B., Kharrou, M. H., Khabba, S., Mougenot, B., Olioso, A., Rodriguez, J. C., & Simonneaux, V. (2006). Monitoring wheat phenology and irrigation in Central Morocco: On the use of relationships between evapotranspiration, crops coefficients, leaf area index and remotely-sensed vegetation indices. *Agricultural Water Management*, *79*(1), 1–27. https://doi.org/10.1016/J.AGWAT.2005.02.013

El-Naggar, A. G., Hedley, C. B., Horne, D., Roudier, P., & Clothier, B. E. (2020). Soil sensing technology improves application of irrigation water. *Agricultural Water Management*, *228*, 105901. https://doi.org/10.1016/J.AGWAT.2019.105901

Fallatah, O. A., Ahmed, M., Cardace, D., Boving, T., & Akanda, A. S. (2019). Assessment of modern recharge to arid region aquifers using an integrated geophysical, geochemical, and remote sensing approach. *Journal of Hydrology*, *569*, 600–611. https://doi.org/10.1016/J.JHYDROL.2018.09.061

Famiglietti, J. S., & Rodell, M. (2013). Water in the balance. In *Science* (Vol. 340, Issue 6138, pp. 1300–1301). American Association for the Advancement of Science. https://doi.org/10.1126/science.1236460

Ferreira, M. I., Silvestre, J., Conceição, N., Aureliano, •, & Malheiro, C. (2012). Crop and stress coefficients in rainfed and deficit irrigation vineyards using sap flow techniques. *Irrig Sci*, *30*, 433–447. https://doi.org/10.1007/s00271-012-0352-2

Gleeson, T., Wada, Y., Bierkens, M. F. P., Ludovicus, &, & van Beek, P. H. (2012). *Water balance of global aquifers revealed by groundwater footprint*. https://doi.org/10.1038/nature11295

Glenn, E. P., Huete, A. R., Nagler, P. L., & Nelson, S. G. (2008). Relationship Between Remotely-sensed Vegetation Indices, Canopy Attributes and Plant Physiological Processes: What Vegetation Indices Can and Cannot Tell Us About the Landscape. *Sensors 2008, Vol. 8, Pages 2136-2160*, *8*(4), 2136–2160. https://doi.org/10.3390/S8042136

Gómez-Candón, D., Bellvert, J., & Royo, C. (2021). Performance of the Two-Source Energy Balance (TSEB) Model as a Tool for Monitoring the Response of Durum Wheat to Drought by High-Throughput Field Phenotyping. *Frontiers in Plant Science*, *12*, 623. https://doi.org/10.3389/FPLS.2021.658357/BIBTEX

Gorelick, N., Hancher, M., Dixon, M., Ilyushchenko, S., Thau, D., & Moore, R. (2017). Google Earth Engine: Planetary-scale geospatial analysis for everyone. *Remote Sensing of Environment*, *202*, 18–27. https://doi.org/10.1016/J.RSE.2017.06.031

Gourdji, S. M., Mathews, K. L., Reynolds, M., Crossa, J., & Lobell, D. B. (2012). An assessment of wheat yield sensitivity and breeding gains in hot environments. *Proceedings. Biological Sciences*, *280*(1752). https://doi.org/10.1098/RSPB.2012.2190

Hou, M., Tian, F., Ortega-Farias, S., Riveros-Burgos, C., Zhang, T., & Lin, A. (2021). Estimation of crop transpiration and its scale effect based on ground and UAV thermal infrared remote sensing images. *European Journal of Agronomy*, *131*, 126389. https://doi.org/10.1016/J.EJA.2021.126389

Huang, Z., Liu, X., Sun, S., Tang, Y., Yuan, X., & Tang, Q. (2021). Global assessment of future sectoral water scarcity under adaptive inner-basin water allocation measures. *Science of The Total Environment*, *783*, 146973. https://doi.org/10.1016/J.SCITOTENV.2021.146973

Hunsaker, D. J., Pinter, P. J., & Kimball, B. A. (2005). Wheat basal crop coefficients determined by normalized difference vegetation index. *Irrigation Science*, *24*(1), 1–14. https://doi.org/10.1007/S00271-005-0001-0/FIGURES/8

Jiang, S., Liang, C., Cui, N., Zhao, L., Liu, C., Feng, Y., ... Zou, Q., 2020. Water use efficiency and its drivers in four typical agroecosystems based on flux tower measurements. Agricultural and Forest Meteorology, 295, 108200.

Kadam, S. A., Stöckle, C. O., Liu, M., Gao, Z., & Russell, E. S. (2021). Suitability of Earth Engine Evaporation Flux (EEFlux) Estimation of Evapotranspiration in Rainfed Crops. *Remote Sensing 2021, Vol. 13, Page 3884*, *13*(19), 3884. https://doi.org/10.3390/RS13193884

Krol, M. S., & Bronstert, A. (2007). Regional integrated modelling of climate change impacts on natural resources and resource usage in semi-arid Northeast Brazil. *Environmental Modelling & Software*, *22*(2), 259–268. https://doi.org/10.1016/J.ENVSOFT.2005.07.022

Kumar, P., Avtar, R., Dasgupta, R., Johnson, B. A., Mukherjee, A., Ahsan, M. N., Nguyen, D. C. H., Nguyen, H. Q., Shaw, R., & Mishra, B. K. (2020). Socio-hydrology: A key approach for adaptation to water scarcity and achieving human well-being in large riverine islands. *Progress in Disaster Science*, *8*, 100134. https://doi.org/10.1016/J.PDISAS.2020.100134

Laipelt, L., Henrique Bloedow Kayser, R., Santos Fleischmann, A., Ruhoff, A., Bastiaanssen, W., Erickson, T. A., & Melton, F. (2021). Long-term monitoring of evapotranspiration using the SEBAL algorithm and Google Earth Engine cloud computing. *ISPRS Journal of Photogrammetry and Remote Sensing*, *178*, 81–96. https://doi.org/10.1016/J.ISPRSJPRS.2021.05.018

Lan, L., Iftekhar, M. S., Fogarty, J., & Schilizzi, S. (2021). Performance of a uniform proportional "cut" to manage declining groundwater in Western Australia. *Journal of Hydrology*, *598*, 126421. https://doi.org/10.1016/J.JHYDROL.2021.126421

Li, H., Li, J., Shen, Y., Zhang, X., & Lei, Y. (2018). Web-based irrigation decision support system with limited inputs for farmers. *Agricultural Water Management*, *210*, 279–285. https://doi.org/10.1016/J.AGWAT.2018.08.025

Liou, Y.-A., & Kar, S. K. (2014). Evapotranspiration Estimation with Remote Sensing and Various Surface Energy Balance Algorithms—A Review. *Energies 2014, Vol. 7, Pages 2821-2849*, *7*(5), 2821–2849. https://doi.org/10.3390/EN7052821

Mauder, M., & Foken, T. (2006). Impact of post-field data processing on eddy covariance flux estimates and energy balance closure. *Meteorologische Zeitschrift*, *15*(6), 597-610. https://doi..org/10.1127/0941-2948/2006/0167

Magaña, V., Herrera, E., Ábrego-Góngora, C. J., & Ávalos, J. A. (2021). Socioeconomic Drought in a Mexican Semi-arid City: Monterrey Metropolitan Area, a Case Study. *Frontiers in Water*, *3*, 3. https://doi.org/10.3389/FRWA.2021.579564/BIBTEX

Meisner, C. A., Acevedo, E., Flores, D., Sayre, K., Ortiz-Monasterio, I., & Byerleee, D. (1992). *Wheat Special Report NO.6 Wheat Production & Grower Practices in the Yaqui Valley, Sonora, Mexico*.

Méndez-Barroso, L. A., Garatuza-Payán, J., & Vivoni, E. R. (2008). Quantifying water stress on wheat using remote sensing in the Yaqui Valley, Sonora, Mexico. *Agricultural Water Management*, *95*(6), 725–736. https://doi.org/10.1016/J.AGWAT.2008.01.016

Mengmeng, D., Noboru, N., Atsushi, I., & Yukinori, S. (2017). Multi-temporal monitoring of wheat growth by using images from satellite and unmanned aerial vehicle. *International Journal of Agricultural and Biological Engineering*, *10*(5), 1–13. https://doi.org/10.25165/IJABE.V10I5.3180

Mo, Y., Li, G., Wang, D., Lamm, F. R., Wang, J., Zhang, Y., Cai, M., & Gong, S. (2020). Planting and preemergence irrigation procedures to enhance germination of subsurface drip irrigated corn. *Agricultural Water Management*, *242*, 106412. https://doi.org/10.1016/J.AGWAT.2020.106412

Montecillo-Cedillo J. L. (2016). Grain corn yield per hectare in Mexico: irrigation districts vs temporal irrigation. *Economia Informa*, *398*, 60–74. http://www.edistritos.com/DR/estadisticaAgricola/

Nieto, H., Kustas, W. P., Torres-Rúa, A., Alfieri, J. G., Gao, F., Anderson, M. C., White, W. A., Song, L., Alsina, M. del M., Prueger, J. H., McKee, M., Elarab, M., & McKee, L. G. (2019). Evaluation of TSEB turbulent fluxes using different methods for the retrieval of soil and canopy component temperatures from UAV thermal and multispectral imagery. *Irrigation Science*, *37*(3), 389–406. https://doi.org/10.1007/S00271-018-0585-9/FIGURES/9

Niu, S.L., Xing, X.R., Zhang, Z., Xia, J.Y., Zhou, X.H., Song, B., Li, L.H., Wan, S.Q., 2011. Water-use efficiency in response to climate change: from leaf to ecosystem in a temperate steppe. Glob. Change Biol. 17, 1073–1082.

Ojeda-Bustamante, W., González-Camacho, J. M., Sifuentes-Ibarra, E., Isidro, E., & Rendón-Pimentel, L. (2007). Using spatial information systems to improve water management in

Mexico. *Agricultural Water Management*, *89*(1–2), 81–88. https://doi.org/10.1016/J.AGWAT.2006.11.002

Omer, A., Elagib, N. A., Zhuguo, M., Saleem, F., & Mohammed, A. (2020). Water scarcity in the Yellow River Basin under future climate change and human activities. *Science of The Total Environment*, *749*, 141446. https://doi.org/10.1016/J.SCITOTENV.2020.141446

Paço, T. A., Pôças, I., Cunha, M., Silvestre, J. C., Santos, F. L., Paredes, P., & Pereira, L. S. (2014). Evapotranspiration and crop coefficients for a super intensive olive orchard. An application of SIMDualKc and METRIC models using ground and satellite observations. *Journal of Hydrology*, *519*(PB), 2067–2080. https://doi.org/10.1016/J.JHYDROL.2014.09.075

Pelosi, A., & Chirico, G. B. (2021). Regional assessment of daily reference evapotranspiration: Can ground observations be replaced by blending ERA5-Land meteorological reanalysis and CM-SAF satellite-based radiation data? *Agricultural Water Management*, *258*, 107169. https://doi.org/10.1016/J.AGWAT.2021.107169

Pereira, L. S., Paredes, P., & Jovanovic, N. (2020). Soil water balance models for determining crop water and irrigation requirements and irrigation scheduling focusing on the FAO56 method and the dual Kc approach. *Agricultural Water Management*, *241*, 106357. https://doi.org/10.1016/J.AGWAT.2020.106357

Perez-Priego, O., Katul, G., Reichstein, M., El-Madany, T. S., Ahrens, B., Carrara, A., Scanlon, T. M., & Migliavacca, M. (2018). Partitioning Eddy Covariance Water Flux Components Using Physiological and Micrometeorological Approaches. *Journal of*

Geophysical Research: Biogeosciences, *123*(10), 3353–3370. https://doi.org/10.1029/2018JG004637

Perrone, D. (2020). Groundwater Overreliance Leaves Farmers and Households High and Dry. *One Earth*, *2*(3), 214–217. https://doi.org/10.1016/J.ONEEAR.2020.03.001

Pôças, I., Calera, A., Campos, I., & Cunha, M. (2020). Remote sensing for estimating and mapping single and basal crop coefficientes: A review on spectral vegetation indices approaches. *Agricultural Water Management*, *233*, 106081. https://doi.org/10.1016/J.AGWAT.2020.106081

Portmann, F. T., Siebert, S., & Döll, P. (2010). MIRCA2000—Global monthly irrigated and rainfed crop areas around the year 2000: A new high-resolution data set for agricultural and hydrological modeling. *Global Biogeochemical Cycles*, *24*(1), n/a-n/a. https://doi.org/10.1029/2008GB003435

Ran, H., Kang, S., Li, F., Tong, L., Ding, R., Du, T., Li, S., & Zhang, X. (2017). Performance of AquaCrop and SIMDualKc models in evapotranspiration partitioning on full and deficit irrigated maize for seed production under plastic film-mulch in an arid region of China. *Agricultural Systems*, *151*, 20–32. https://doi.org/10.1016/J.AGSY.2016.11.001

Reyes-González, A., Kjaersgaard, J., Trooien, T., Hay, C., & Ahiablame, L. (2018). Estimation of Crop Evapotranspiration Using Satellite Remote Sensing-Based Vegetation Index. *Advances in Meteorology*, *2018*. https://doi.org/10.1155/2018/4525021

Reyes-González, A., Kjaersgaard, J., Trooien, T., Reta-Sánchez, D. G., Sánchez-Duarte, J. I., Preciado-Rangel, P., & Fortis-Hernández, M. (2019). Comparison of Leaf Area Index,

Surface Temperature, and Actual Evapotranspiration Estimated Using the METRIC Model and In Situ Measurements. *Sensors (Basel, Switzerland)*, *19*(8). https://doi.org/10.3390/S19081857

Rost, S., Gerten, D., Bondeau, A., Lucht, W., Rohwer, J., & Schaphoff, S. (2008). Agricultural green and blue water consumption and its influence on the global water system. *Water Resources Research*, *44*(9), 9405. https://doi.org/10.1029/2007WR006331

Roy, P. D., Logesh, N., Lakshumanan, C., & Sánchez-Zavala, J. L. (2021). Decadal-scale spatiotemporal changes in land use/land cover of El Potosi Basin at semi-arid northeast Mexico and evolution of peat fire between 1980-2020 CE. *Journal of South American Earth Sciences*, *110*, 103395. https://doi.org/10.1016/J.JSAMES.2021.103395

Schoppach, R., & Sadok, W. (2012). Differential sensitivities of transpiration to evaporative demand and soil water deficit among wheat elite cultivars indicate different strategies for drought tolerance. *Environmental and Experimental Botany*, *84*, 1–10. https://doi.org/10.1016/J.ENVEXPBOT.2012.04.016

Schoppach, R., & Sadok, W. (2013). Transpiration sensitivities to evaporative demand and leaf areas vary with night and day warming regimes among wheat genotypes. *Functional Plant Biology : FPB*, *40*(7), 708–718. https://doi.org/10.1071/FP13028

Schüttemeyer, D., Schillings, C., Moene, A. F., & de Bruin, H. A. R. (2007). Satellite-Based Actual Evapotranspiration over Drying Semiarid Terrain in West Africa. *Journal of Applied Meteorology and Climatology*, *46*(1), 97–111. https://doi.org/10.1175/JAM2444.1

Stromann, O., Nascetti, A., Yousif, O., & Ban, Y. (2019). Dimensionality Reduction and Feature Selection for Object-Based Land Cover Classification based on Sentinel-1 and Sentinel-2 Time Series Using Google Earth Engine. *Remote Sensing 2020, Vol. 12, Page 76*, *12*(1), 76. https://doi.org/10.3390/RS12010076

Swain, S. S., Mishra, A., Sahoo, B., & Chatterjee, C. (2020). Water scarcity-risk assessment in data-scarce river basins under decadal climate change using a hydrological modelling approach. *Journal of Hydrology*, *590*, 125260. https://doi.org/10.1016/J.JHYDROL.2020.125260

Tang, X., Li, H., Desai, A.R., Nagy, Z., Luo, J., Kolb, T.E., Olioso, A., Xu, X., Yao, L., Kutsch, W., Pilegaard, K., Köstner, B., Ammann, C., 2014. How is water-use efficiency of terrestrial ecosystems distributed and changing on Earth? Sci. Rep. 4, 7483.

Tenreiro, T. R., García-Vila, M., Gómez, J. A., Jiménez-Berni, J. A., & Fereres, E. (2021). Using NDVI for the assessment of canopy cover in agricultural crops within modelling research. *Computers and Electronics in Agriculture*, *182*, 106038. https://doi.org/10.1016/J.COMPAG.2021.106038

Turner, S. W. D., Hejazi, M., Yonkofski, C., Kim, S. H., & Kyle, P. (2019). Influence of Groundwater Extraction Costs and Resource Depletion Limits on Simulated Global Nonrenewable Water Withdrawals Over the Twenty-First Century. *Earth's Future*, *7*(2), 123–135. https://doi.org/10.1029/2018EF001105

Wada, Y., Beek, L. P. H. van, Kempen, C. M. van, Reckman, J. W. T. M., Vasak, S., & Bierkens, M. F. P. (2010). Global depletion of groundwater resources. *Geophysical Research Letters*, *37*(20). https://doi.org/10.1029/2010GL044571

Wallace, J. S. (2000). Increasing agricultural water use efficiency to meet future food production. *Agriculture, Ecosystems & Environment*, *82*(1–3), 105–119. https://doi.org/10.1016/S0167-8809(00)00220-6

Wan, H., McLaughlin, D., Shao, Y., van Eerden, B., Ranganathan, S., & Deng, X. (2021). Remotely-sensed evapotranspiration for informed urban forest management. *Landscape and Urban Planning*, *210*, 104069. https://doi.org/10.1016/J.LANDURBPLAN.2021.104069

Wang, J., & Bras, R. L. (2009). A model of surface heat fluxes based on the theory of maximum entropy production. *Water Resources Research*, *45*(11). https://doi.org/10.1029/2009WR007900

Wang, J., & Bras, R. L. (2011). A model of evapotranspiration based on the theory of maximum entropy production. *Water Resources Research*, *47*(3), 3521. https://doi.org/10.1029/2010WR009392

Zhang, W., Brandt, M., Wang, Q., Prishchepov, A. v., Tucker, C. J., Li, Y., Lyu, H., & Fensholt, R. (2019). From woody cover to woody canopies: How Sentinel-1 and Sentinel-2 data advance the mapping of woody plants in savannas. *Remote Sensing of Environment*, *234*, 111465. https://doi.org/10.1016/j.rse.2019.111465

Zhang, Y., Zhang, Y., Shi, K., & Yao, X. (2017). Research development, current hotspots, and future directions of water research based on MODIS images: a critical review with a

bibliometric analysis. *Eviron Sci Pollut Res* , 15226–15239. https://doi.org/10.1007/s11356-017-9107-1

Zhao, J., Li, C., Yang, T., Tang, Y., Yin, Y., Luan, X., & Sun, S. (2020). Estimation of high spatiotemporal resolution actual evapotranspiration by combining the SWH model with the METRIC model. *Journal of Hydrology*, *586*, 124883. https://doi.org/10.1016/J.JHYDROL.2020.124883

Zhou, S., Yu, B., Zhang, Y., Huang, Y., Wang, G., 2016. Partitioning evapotranspiration based on the concept of underlying water use efficiency. Water Resour. Res. 52, 1160–1175.

Zhou, S., Yu, B., Zhang, Y., Huang, Y., Wang, G., 2018. Water use efficiency and evapotranspiration partitioning for three typical ecosystems in the Heihe River Basin, northwestern China. Agric. . Meteorol. 253–254, 261–273.

Zhu, X.-J., Yu, G.-R., Hu, Z.-M., Wang, Q.-F., He, H.-L., Yan, J.-H., Wang, H.-M., Zhang, J.-H., 2015. Spatiotemporal variations of T/ET (the ratio of transpiration to evapotranspiration) in three forests of Eastern China. Ecol. Indic. 52, 411–421.

Chapter 3. Assessment of Irrigation Efficiencies of An Agricultural Valley with An Over-Exploited Aquifer Using the PETVI Method.

3.1 Introduction

In Mexico, some of the largest and most productive irrigation districts and units are located in the northern part of the country, where arid and semiarid conditions prevail (SIAP, 2016). In those regions, the most challenging issue farmers are faced with is the availability of water. In most cases, water from surface reservoirs and aquifers are the main source of water for irrigation because precipitation is significantly lower than evapotranspiration. Hence those water sources are needed to guarantee good crop yields. Overexploited aquifers are a concern in different regions; specifically in arid and semiarid locations (Gleeson et al., 2012). In areas marked by urban growth, economic activities such as agriculture frequently lead to stressed groundwater sources (Konikow and Kendy., 2005). In Mexico's northern drylands agriculture can make up 80% of the water use (Wurl et al., 2018). For example, in 2018, agricultural production in the state of Chihuahua used 89 % of the total available water for all activities, and from this amount, groundwater used for agricultural production supplied around 2,772 hm^3 $year^{-1}$, and surface water used 2,054 hm^3 $year^{-1}$ (CONAGUA 2018). The primary perennial crops planted in the state of Chihuahua, in north central Mexico, in 2018 were: alfalfa with 89,688 hectares, pecans orchards with 84,928 hectares, and apple orchards with 28,368. Annual crops consisted of cotton, with 164,841 hectares planted, followed by corn with 125,862 hectares using both, surface and groundwater sources. All of these crops were cultivated under intensive irrigation schemes (SIAP, 2019).

Similar to most regions of the world with arid and semiarid conditions, economic activities in northern and central Mexico, and particularly agriculture, rely on groundwater. Technical

reports from Mexico's National Water Commission (CONAGUA, 2011) have shown that 32 of the most important aquifers of the country are overexploited, meaning more water is being extracted than that being recharged. Moreover, from the total amount of water used in the country, 50.6 % comes from those overexploited aquifers, where agricultural activities are the main users. Consequently, higher water use efficiency and conservation in agriculture in those regions is urgently needed.

Improving irrigation practices in agriculture can help alleviate the pressure on water resources, particularly in places where groundwater supplies the majority of the water. To do this, knowledge of irrigation efficiency, both at the parcel and irrigation district is critical. But depending on the definition of irrigation efficiency, some measures of this term may be more or less useful for the purpose of conserving water while maintaining high crop yields. Traditionally, irrigation efficiency is defined as the percentage of water delivered in the parcel that becomes evapotranspiration (ET_a) (Tennakoon and Milroy, 2003; Ahadi *et al*., 2013). This definition implies that the higher the amount of water that becomes ET_a, the higher the efficiency will be, regardless of how much of that water is actually used by the crop and how much is lost as direct evaporation from the soil or standing water on the furrows when flood irrigated. Because irrigation efficiency is used as an indicator of the modernization or technification of irrigation, this term can also be applied to systems that combine water management and irrigation technology (Wu et al., 2009). Others have defined water use efficiency in agriculture as the crop transpiration ratio to the total water volume delivered to the field (Wang et al., 1996), or as the ratio of the volume of water stored in the root zone over the volume of water extracted from the primary source (Jia *et al*., 2013). Taking the definition of Wu et al., (2019) in which irrigation efficiency is an indicator reflecting water management and irrigation technologies at different scales, this can then be used

to develop plans for adapting to current and future water scarcity scenarios (Fader et al., 2016). As freshwater has become scarce in many regions on a global scale and even more acutely in arid and semiarid areas, it is imperative to improve irrigation efficiency (Ma *et al*., 2018). A general vision of irrigation efficiency is measuring the opportune water delivery to the crops through different irrigation systems without reducing the water for environmental and human uses.

The Mexican National Water Commission (CONAGUA) reported an average decline of 2 m $year^{-1}$ in the regional water levels of the Cuauhtémoc aquifer of Northern Mexico in between the years 1988 to 1997 (CONAGUA, 2002). This report aligns with the stress level found by Gleeson *et al*., (2012) in other places of the world with similar conditions, showing that northwestern Mexico has attained high groundwater stress levels as well. Under these stress levels it is necessary to improve water management and conservation for irrigated agriculture where deficient water delivery practices is taking place along with the much needed application of strategies to improve water use efficiencies.

Water supply conflicts between agricultural and urban areas have recently started to appear, particularly in population centers and agricultural regions located in arid and semi-arid environments (Hargrove et al., 2013). For example, projections from a study of 482 cities around the world using data from 1971 to 2000 found that 46% of the cities studied may experience a deficit of surface water, and in many of those cases, agricultural water users will conflict with cities due to water shortages to meet both urban and crop water needs (Flörke et al., 2018). Similarly, Molle and Berkoff (2009) found that wasteful irrigation and bureaucratic inefficiency point to water scarcity in urban areas. This is precisely what is occurring currently in the Cuauhtémoc aquifer, where water is supplied through 17 deep wells from which 12 Mm^3 per year are extracted for use in urban contexts. Seasonally recurring issues with the city's water supply

caused by the lowering of the water table in the aquifer affect the city's wells at the height of the irrigation season and coincide with the warmest temperatures of the year, creating serious sanitary hazards for the population of Cuauhtémoc, Chihuahua (Díaz et al., 2014). The overexploitation of the Cuauhtémoc aquifer conflicts with its two main users. When irrigation for crop water is at its maximum in the valley, some of the city wells run dry and urban areas located in the higher areas of Cuauhtémoc face water cuts for considerable periods of time.

Knowledge about water use efficiency in a parcel for different irrigation systems (Furrow, Sprinkles, and drip irrigation) is needed. The study's main objective is to assess the productive water use efficiency as the ratio of transpiration to the total water delivered in the plot, using the *PETVI* method in the Cuauhtémoc agricultural valley in northern Mexico. First, we describe the historical context leading to the current unsustainable agricultural activities discussing the climate conditions, principal activities, and prevailing irrigation practices in the region. Next, we address the methodology used to study the irrigation efficiencies of six observation plots representative of the region, by describing the material and methods that were used in the process. We then discuss the results of the irrigation efficiency analysis, their meaning and implication in the context of the aquifer overexploitation and finally we provide some concluding remarks projecting different scenarios of water irrigation improvements without further technification/modernization of the current irrigation systems.

3.1.1 Background and historical evolution of water resources in the Cuauhtémoc valley

Groundwater irrigated agriculture in the Cuauhtémoc valley started in the early 1950s (Sawatzky, 1971; Castro-Martínez, 2000). The first apple orchards were registered in 1953

(SAGARPA, 2013), and favorable climatic conditions and groundwater availability for irrigation helped Cuauhtémoc become the largest producer of apples in Mexico (SIAP, 2018). After industrial-scale apple production started, industrial-scale corn production followed, reaching approximately 470 km^2 of irrigated croplands in Lagoon Bustillos Basing. The conversion of land from a pasture and small-scale rainfed agriculture to intensive irrigation changed the basin's hydrologic dynamics, producing an unsustainable groundwater exploitation scheme. Figure 3.1 represents a hypothetical conceptual model of the Cuauhtémoc Aquifer (*CA*). Their hydrologic evolution, following changes in irrigation modes and magnitudes, and its resulting increases in production operation costs in 5 periods in which the first three periods have occurred or are presently occurring. The last two are desirable periods for the future. The description of each period is as follows: 1) An initial groundwater pumping (red line) did not affect the aquifer volume significantly because the water table (blue line) was able to recover and keep its original level from rapid natural recharge (green line); (2) Overexploitation (orange) started when water pumping exceeded the rate of recharge, resulting in an aquifer drawdown. At the same time, new drillings appear all over the basin, and the depth to the water table notably increases yearly, forcing deeper drillings to reach the water table, thus increasing pumping costs. During this period, the natural recharge rate is augmented and starts being affected by notable climate variability; (3) a period of gradual and non-stop groundwater overexploitation (Orange), with notable population growth (brownish), results in a gradual groundwater abatement (blue line) due to constant pumping activity leading to groundwater mining; (4) an ideal period of technological progress will contribute to gradually reduce the groundwater extraction rate (red line) and pumping costs making the groundwater level to recover gradually while helped by the natural recharge; (5) over time there will be equilibrium and recovering of the aquifer making water extraction sustainable. This

figure shows a changing recharge rate and a variable and out-of-phase groundwater pumping rate in response to the interannual changes in climatic conditions. The magnitudes and the ranges of fluctuation for recharge processes and groundwater pumping are currently unknown. We hypothesize that the fluctuation of these processes in the present time responds directly to human intervention in the hydrologic cycle of the Lagoon Bustillos Basin and indirectly to the natural climatic variability of the area that affects groundwater use in the basin.

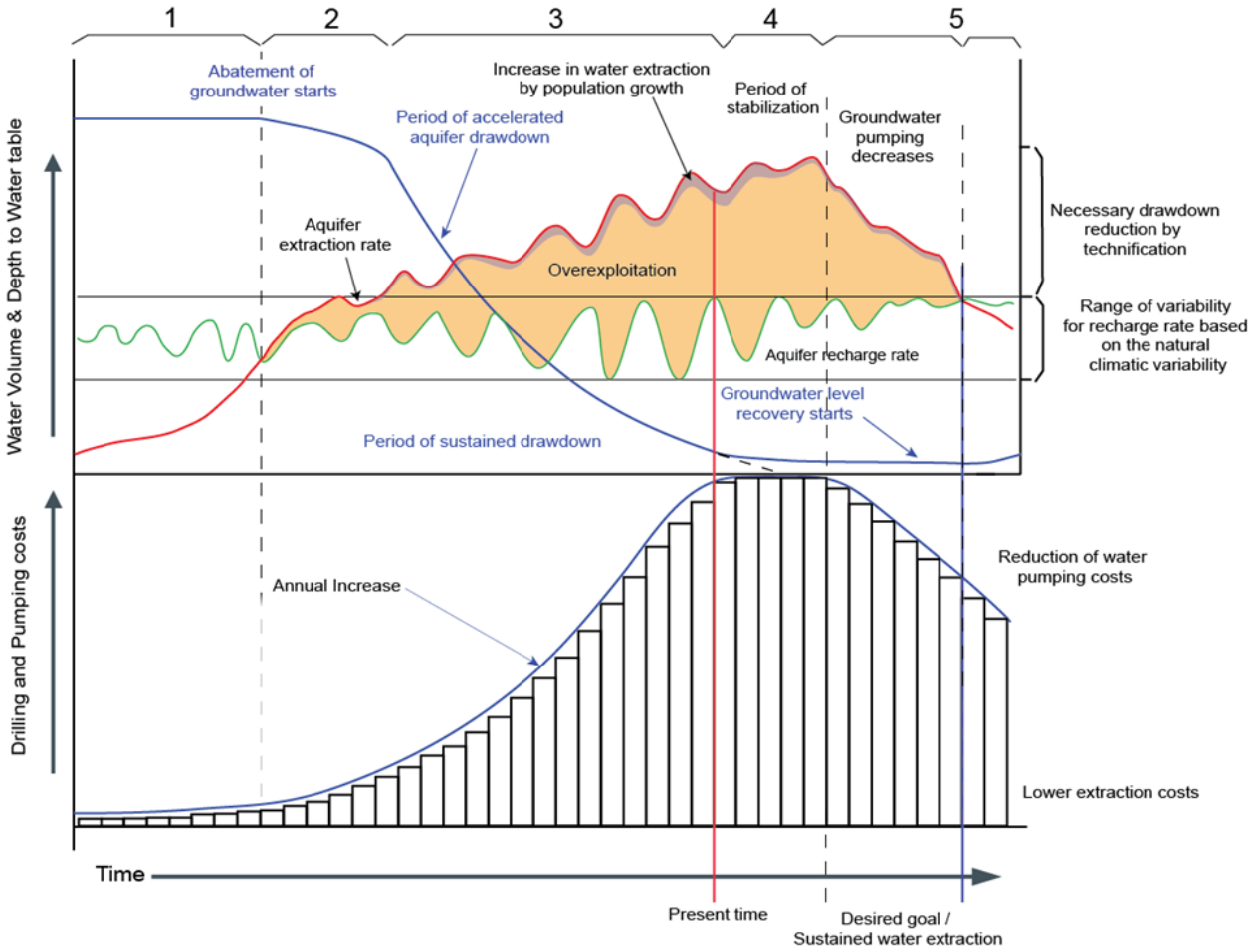

Figure 3.1 Conceptual model (not to scale) of the Cuauhtémoc aquifer recharge rate, pumping, and phreatic levels evolution versus the drilling and pumping costs from the beginning of the agriculture activity in the basin (periods 1-3), the actual situation (period 3) and a hypothetical and desirable sustainable future (periods 4 and 5).

3.2 Materials and Methods

3.2.1 Study site

The agricultural valley is located in the influence area of the Cuauhtémoc aquifer. It is between the coordinates 28°13'19" and 28°59'35" North and -106°34'39" and 107° 10'33" (Figure 3.2). This aquifer has a similar shape to Bustillo's basin. In this area, 58 % of the surface is dedicated to agricultural activities. The site is located in the endorheic basin, where rainfall is the primary source of the natural recharge to the aquifer. It has an annual precipitation of 460 mm, and the temperature in this area is; minimum of -10.5, a maximum of 24, and an average of 14.6 degrees Celsius (Medina et al., 2006). The current situation of the aquifer shows an extraction of 497.90 hm^3 and recharge of 299.40 hm^3, which points to the unsustainability of the Cuauhtémoc aquifer. The agricultural valley has an average elevation of 2000 meters above sea level (CONAGUA, 1991; Alatorre et al., 2014). Cuauhtémoc, with a population of 160,000 people, is the most important city in the area of study. The main economic activity in the Cuauhtémoc Aquifer region is agriculture, with an extension of land measuring around 55,000 hectares that has access to irrigation. Of these 55,000 ha 47,000 ha are dedicated to corn, and 8,000 are used for apples. Groundwater is the primary source of water that maintains agricultural production. With respect to the cornfields, 97 % of them are irrigated with the furrow technique, 2 % through sprinkler irrigation, and only 1% makes use of drip irrigation (Santos-Hernández et al., 2019). This study examines seven field plots where corn was cultivated during the agricultural cycle in 2017; three plots are dedicated to furrow irrigation, two parcels to drip irrigation, and two parcels to sprinkler irrigation. The surface evaluated was: two sites equipped with drip irrigation systems of 16 and 20 ha, respectively, two sites equipped with sprinkler irrigation, 50 and 63 ha, and the conventional

furrow irrigation systems 32, 25, and 47 ha. The sites of the cooperating producers were randomly selected along the agricultural valley.

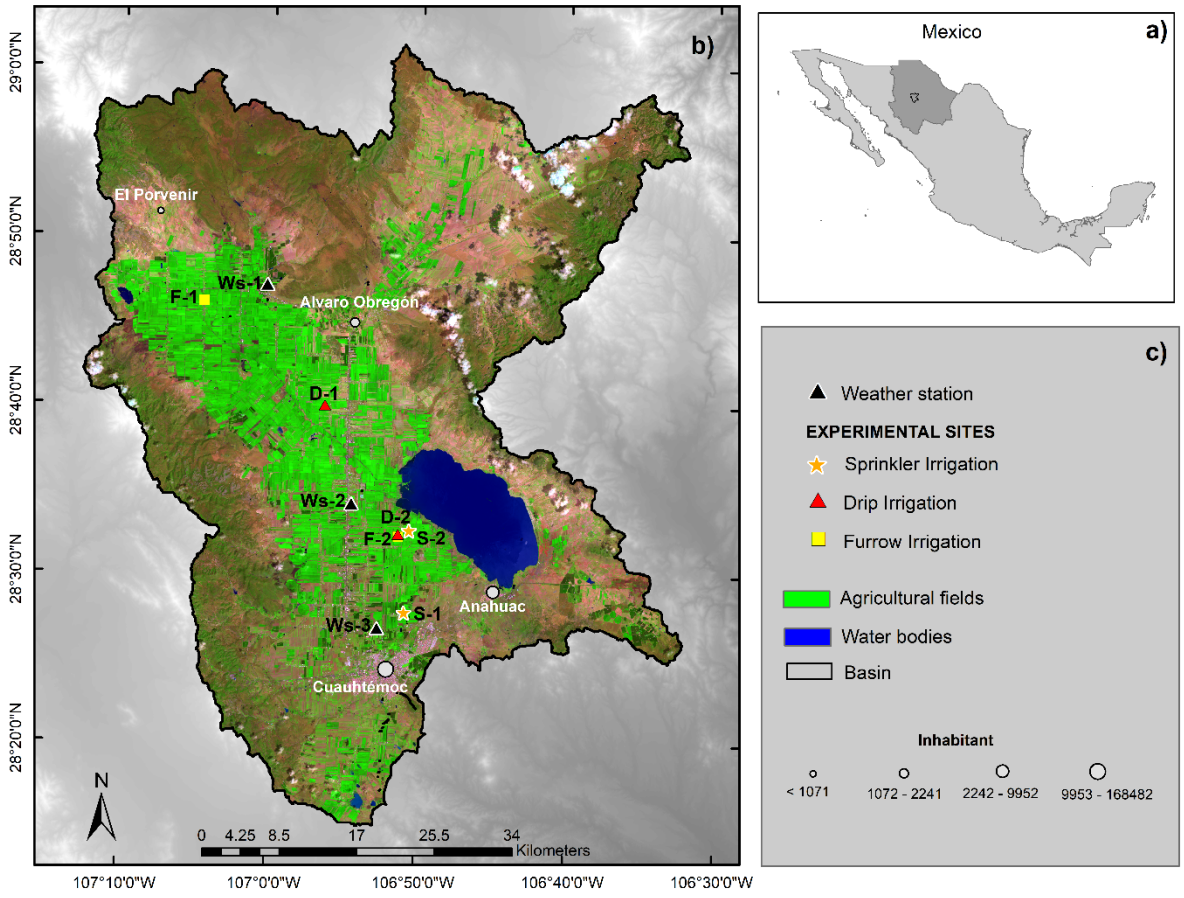

Figure 3.2 a) Show the state of Chihuahua Mexico; b) General view of the Bustillos Lagun Basin delimited by mountains represented by the black line forming a closed basin with its central part forming a large valley. The agricultural plots are shown in a light green color within the basin, making up ~ 80% of the basin's surface. The observation plots distributed in the farming valley are shown. The parcels were labeled as F-1, F- 2 for furrow irrigation, represented by small yellow squares; S-1, S-2 for sprinkler irrigation sites, represented by yellow; and D-1, D-2 for drip irrigation sites, represented by red triangles, standard weather stations are represented by black triangles. White dots represent the main population centers. In addition, three bodies of water are *displayed, one in the north, one in the south, and a larger one that serves important ecological needs called the Laguna de Bustillos in the southwestern part of the basin that has following dimensions: 16 km long and 8 km wide at its maximum capacity.*

3.2.2 Data

3.2.3 Meteorological data

The weather data was obtained from the *Union Agricola Regional de Fruticultores del Estado de Chihuahua A. C.* (*UNIFRUT*). Daily weather station observations of air temperature (°C), relative humidity (%), solar radiation (Kw m^2), wind speed (Km hr^{-1}), and precipitation (mm) are used. The location, latitude, and longitude coordinates of each weather station were obtained from the file manager data of *UNIFRUT*. We used data from three weather stations surrounding the study sites and nearest to the single observation sites.

3.2.4 Remote sensing data

In this study we used remote sensing data, including Landsat 8 evapotranspiration *(ET_a)* images (16 days, 30 m temporal, and spatial resolution, respectively) downloaded from (https://eeflux-level1.appspot.com/), and Sentinel-2 (*S-2*) data (5 days, 10 m temporal and spatial resolution, respectively), *S-2* data are available at (https://developers.google.com/earth-engine/datasets/catalog/COPERNICUS_S2) we used this data from March to November 2017. to cover the observation sites with one image from Landsat (path/Row 033 and 040). We used two scenes for S-2 (mosaic identifier T13RBM and T13RCM) to cover the observation plots. After applying the filter date, the data analysis for the specific observation sites was obtained using the vector shapefile for each plot.

3.2.5 Sentinel-2 data

We used multispectral images with a high temporal and spatial resolution from March to November 2017 (Table 3.1). We processed (*S-2*) imagery in Google Earth Engine (*GEE*) using the top-of-atmosphere reflectance (*TOA*) (Zhang et al., 2019). Recent studies have shown the use of the Normalized Difference Vegetation Index (*NDVI*) to estimate the basal crop coefficient (K_{cb}) (Jiang et al., 2014; López-Urrea et al., 2012; Toureiro et al., 2017). We specifically selected the bands in the near-infrared (~ 0.84 μm wavelength) and the (R) red (~ 0.66 μm central wavelength) portion of the electromagnetic spectrum (Huete et al., 2002). We used these bands to create a time series of the *NDVI* to monitor vegetation dynamics (Martínez & Gilabert, 2009). To eliminate possible spurious data, we generated a time series of the normalized vegetation index for the study plot following standard procedures (Gorelick et al., 2017). This filter removes spurious data in the vegetation index extracted from *S-2* images, rescaling these to K_{cb} values. These procedures were key in obtaining a clean and smooth time series of crop development. Finally, when we already had the data for each observation site, the numerical data was exported to a comma-separated values (*CSV*) file. to process them in Matlab.

Table 3.1 Characteristics of S-2 Images processed on GEE

DATE	NAME	Cloud %		Band 8	Band 4
		T13RBM	T13RCM		
4/29/2017	20170429T174752	12	74	X	X
5/19/2017	20170519T174800	6	0	X	X

6/08/2017	20170608T174718	11	2	X	X
6/28/2017	20170628T174712	7	7	X	X
7/13/2017	20170713T174714	14	12	Nd	Nd
7/18/2017	20170718T174646	58	55	Nd	Nd
8/2/2017	20170802T174713	15	20	Nd	Nd
8/7/2017	20170807T174624	8	1	X	X
8/22/2017	20170822T174710	9	18	Nd	Nd
8/27/2017	20170827T174714	64	49	X	X
9/11/2017	20170911T174826	14	3	X	X
9/16/2017	20170916T175023	30	33	X	X
10/1/2017	20171001T174935	6	6	X	X
10/6/2017	20171006T175353	4	1	X	X
10/21/2017	20171021T175230	0	0	X	X
10/26/2017	20171026T174528	0	0	X	X
11/10/2017	20171110T174631	41	0	X	X

X= data available; Nd= no data

3.2.6 METRIC data

We obtained the images of evapotranspiration (ET_a) from the website (https://eeflux-level1.appspot.com/). Images are freely available after processing with the METRIC algorithm using the Landsat images. The METRIC algorithm computes each pixel of daily actual (ET_a) at each available satellite image of the Landsat series (Allen et al., 2007; Irmak et al., 2012). These ET_a daily values can get the crop coefficient (K_c) using the back-calculation through the simple relationship between ET_a and reference evapotranspiration (ET_0) as follow $K_c = ET_a/ET_0$. The reference evapotranspiration will be calculated using the Penman-Monteith equation using data from the weather station at the time of the satellite overpass. Using this process it is possible to rescale the daily ET_a on a daily time series. Also, the ET_a images were selected with no cloud cover at the observation sites.

Table 3.2 Characteristics of Landsat images processed on GEE

Date	ID	Cloud [%]	Doy
2017-03-13	LC80330402017072LGN00	0	072
2017-03-29	LC80330402017088LGN00	1	088
2017-04-14	LC80330402017104LGN00	51	104
2017-04-30	LC80330402017120LGN00	0	120
2017-05-16	LC80330402017136LGN01	0	136
2017-06-01	LC80330402017152LGN00	30	152
2017-06-17	LC80330402017168LGN00	1	168
2017-07-03	LC80330402017184LGN00	33	184

2017-08-13	LC80320402017225LGN00	58	225
2017-08-21	LE70320402017233EDC00	0	233
2017-08-29	LC80320402017241LGN01	33	241
2017-09-21	LC80330402017264LGN00	1	264
2017-10-07	LC80330402017280LGN00	6	280
2017-10-23	LC80330402017296LGN00	0	296
2017-11-08	LC80330402017312LGN00	23	312

3.2.7 Methods

3.2.8 Crop coefficient and basal crop coefficient.

The representative evolution of the crop coefficient (K_c) component is represented in Figure 3.3, which is represented by a curve that has the same shape as the phenological evolution of the crop. The K_c comprises the evaporation coefficient (K_e) and the basal crop coefficient (K_{cb}). The K_e at the beginning of the crop cycle is always higher, especially if the soil is wetted by irrigation or rain. It decreases as the soil dries or is covered by vegetation. The K_{cb} has an inverse relationship concerning K_e, the K_{cb} values are low at the beginning of the season because it represents the proportion of the vegetation, and at this time, the vegetation is small. However, it increases with crop develoment and reaches its maximum value when the crop reaches its full development. K_c is usually estimated using a lysimeter or relating crop height and meteorological variables (Ko et al., 2009). However, these measurements are not always recorded in the field, but it is possible to infer them from independent estimates of ET_a using the relationship $K_c = ET_a/ET_0$.

Discrete daily values of ET_a can be derived from energy balance algorithms using satellite imagery and meteorological data (e.g. geeSEBAL, Laipelt et al., 2021; eeMETRIC, Allen et al., 2011). Although the K_c function can vary in response to year-to-year climate and water variations, the K_c shape has been widely studied for most crops. Therefore, it is well-known and can be reconstructed by simple linear interpolation from a few values distributed throughout the growing season (Allen et al., 2007; Duchemin et al., 2006; Kumar Gontia et al., 2010). On the other hand, the shape of the K_{cb} function can be tracked by following the phenology of the crop using a vegetation index, such as the Normalized Difference Vegetation Index (*NDVI*). In other words, K_{cb} can be inferred using satellite-derived vegetation indices. Because in a well-watered crop, the phenology of the vegetation shows a smooth curve, potential issues of spurious data on the vegetation indices can be easily discarded by removing outliers data, and interpolation between satellite images to obtain daily vegetation index values can be performed. In the same way, the calculation of K_{cb} represents the proportion of the vegetation. For this reason, K_{cb} can be rescaled from vegetation indices due to its close relationship with the phenological development of the crop. Based on this fact, and if we have the punctual values in time, it is possible to make a linear interpolation to construct the K_{cb} curve for a particular agricultural cycle.

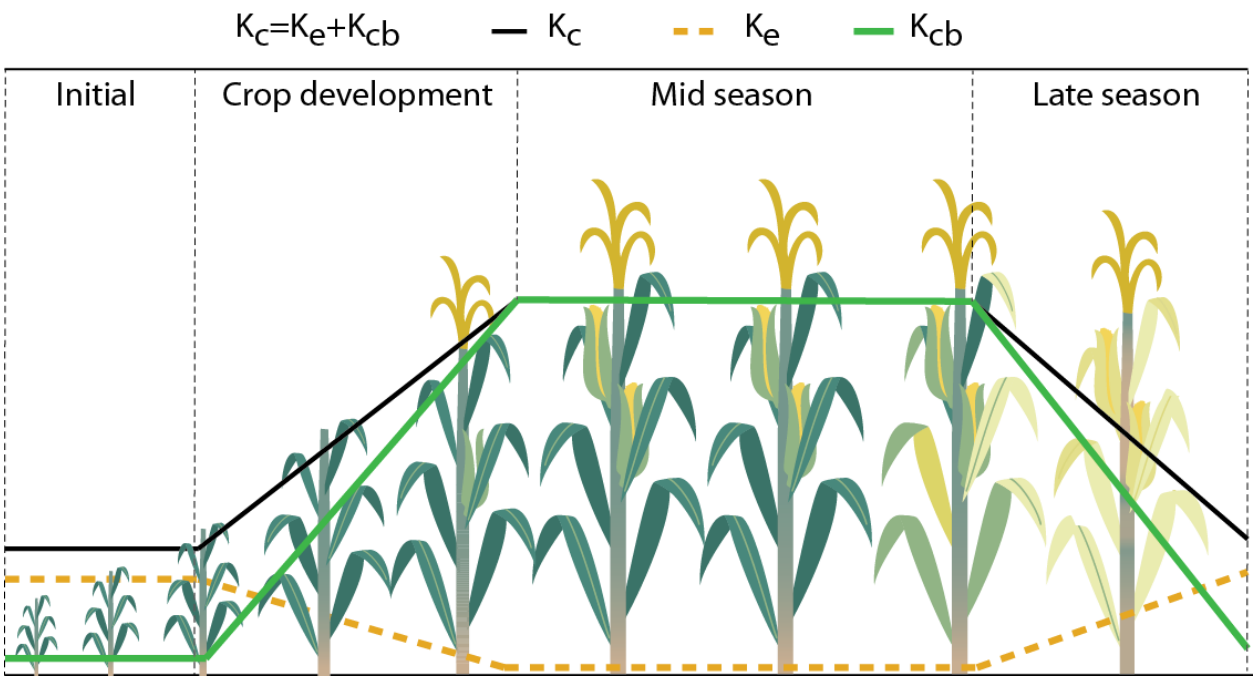

Figure 3.3 shows the scheme of the crop coefficient curve (K_c), represented by the black line; the evaporation coefficient curve (K_e), represented by the yellow dashed line. Moreover, the green line represents the basal crop coefficient curve (K_{cb}); the vertical dashed lines represent the crop growth stages

3.2.9 Basal crop coefficient (K_{cb}) from NDVI and transpiration (T_r).

The validation of the different methodologies using high-precision instruments helps implement the new methods at low cost and is accessible for sites without sophisticated meteorological instrumentation. In this work, we used the *PETVI* method to separate the productive and unproductive water through the estimation of a daily basal crop coefficient (K_{cb}) using a vegetation index (*VI*) following the close relationship between *VI* and crop development during the growing cycle, and the fact that they are in close correspondence with transpiration demands (Allen et al., 2011; Glenn et al., 2008). We calculated the normalized difference vegetation index (NDVI) to monitor vegetation growth dynamics using *S-2* imagery. The images

were processed in the *GEE* platform (Gorelick et al., 2017; Kandekar et al., 2021) using bands 8 (near-infrared) and 4 (red). Before the analysis, the area of interest is defined inside *GEE* by loading a shapefile using the assets manager. For the calculation of *NDVI*, no cloudiness filter was performed on the images because. Once *NDVI* values had been established for the days with available satellite observations, a quality control procedure was carried out to eliminate spurious data that may have been produced by contamination of the reflectance values in the satellite images from cirrus clouds or cloud shading. This analysis was developed through the *NDVI* time series and identified abnormal data values by locating unrealistic sudden drops of *NDVI* that depart from the expected evolution of the vegetation cycle; we eliminated data values from those dates to generate a clean time series. After that procedure, instantaneous K_{cb} values were calculated from the *NDVI* time series by rescaling the *NDVI* values to the seasonally maximum possible K_c reported for that particular crop using the equation for the vegetation cover fraction (Schüttemeyer et al., 2007; Allen et al., 1998; Hunsaker et al., 2005):

$$K_{cb} = 1.20 * \frac{NDVI - NDVI_{min}}{NDVI_{max} - NDVI_{min}} \quad \text{Eq. (1).}$$

In our study we used $NDVI_{min}$ = 0.14, $NDVI_{max}$ = 0.63 and a maximum value of 1.20 for the corn crop coefficient (K_c) following Allen et al., (1998). Because the K_{cb} function of a well-watered crop should follow a relatively smooth trajectory, daily K_{cb} values can be obtained by linearly interpolating between the satellite-derived values, producing a daily time series of K_{cb}. During the growing cycle of the crop, one of the most essential variables changing the proportion of evaporation to transpiration is the evolution of the vegetation fractional cover F_c. As F_c grows, the area of exposed bare soil decreases, reducing the direct evaporation of soil moisture, while the vegetation increases its water demand and, with it, the fraction of ET_a that becomes transpiration.

To account for this process, we calculated F_c through the entire growing cycle using a linear relationship with *NDVI* from *S-2* following (Irmak et al., 2012) (Eq 2.).

$$F_c = \frac{NDVI - NDVI_{min}}{NDVI_{max} - NDVI_{min}} \quad \text{Eq. (2).}$$

The final form of the equation for T_r is then as follows:

$$T_r = K_{cb} * F_c * ET_0 = 1.20 * \left[\frac{NDVI - NDVI_{min}}{NDVI_{max} - NDVI_{min}}\right]^2 * ET_0 \quad \text{Eq. (3).}$$

3.2.10 Reference evapotranspiration (ET0)

We used data from *UNIFRUT* provided by standard weather stations on a daily scale. Following the workflow illustrated in figure 3. Firstly we need to sort the data; maximum and minimum air temperature (°C), relative humidity (%), solar radiation (Kw m^2), and wind speed (Km hr^{-1}), after using Matlab to encode the Penman-Monteith equation (Allen et al., 1998), we obtain the ET0 in (mm day^{-1}) for the study period.

$$ET_0 = \frac{0.408\Delta(R_n - G) + \gamma\left(\frac{900}{T+273}\right)u_2(e_s - e_a)}{\Delta + \gamma(1 + 0.34u_2)} \quad \text{Eq (4),}$$

where ET_0 is the reference evapotranspiration (mm day^{-1}), R_n is the net radiation (MJ m^2 day^{-1}), G is the heat flux density of the soil (MJ m^2 day^{-1}), T is the daily mean air temperature at 2 m height (° C), u_2 is the wind speed at 2 m height (m s^{-1}), e_s is the saturation vapor pressure (kPa), e_a is the real vapor pressure (kPa), Δ is the slope of the vapor pressure curve (kPa ° C^{-1}), γ is the psychrometric constant (kPa ° C^{-1}), and e_s-e_a is the saturation vapor pressure deficit (kPa).

3.2.11 Evapotranspiration from METRIC

In this work we used ET_a data [mm day^{-1}] derived from the *METRIC* algorithm (Allen et al., 2007) using Landsat 7 and 8 missions (path 034 and row 040)1 with a spatial resolution of 30 m and temporal resolution of 16 days. The images were obtained from the *EEFLux* website https://eeflux-level1.appspot.com/ (Allen et al., 2007; Allen et al., 2015; Allen et al., 2011; Wan et al., 2021) and inspected manually to select those free of cloudiness for the study area. The images were uploaded into an image collection inside *GEE* with their respective metadata. Once the collection of images was created, a scene cut was made for the area of interest using a shapefile. Given the characteristics of the study, it was necessary to have daily ET_a values. However, linear interpolation of ET_a values is nonviable due to their dependence on daily conditions in local weather that can vary substantially daily. To overcome this problem, we derived K_c values from the satellite-derived ET_a following the well-established relationship between the ratio of evapotranspiration and the reference Evapotranspiration (ET_0) from local weather data to K_c (Eq. 5).

$$K_c = \frac{ET_a}{ET_0} \qquad \text{Eq. (5).}$$

where K_c is the crop coefficient, ET_a is the daily evapotranspiration from *METRIC*, and ET_0 is the reference evapotranspiration. Using equation 6, we obtained the K_c daily values. With this approach, some dates with low ET_a can yield lower K_c values than expected based on the crop phenological stage. Therefore, ET_a images obtained from the energy balance algorithm (i.e. *METRIC*) need to be previously calibrated by adjusting the K_c using the tabulated values and observations of the crop in the experimental site based on its phenological stage.

3.2.12 Partitioning Evapotranspiration

The ET_a flux separation in evaporation (E_v) and transpiration (T_r) for the proposed approach was estimated as the residual of ET_a and T_r, similar to the FAO-56 dual crop coefficient method (Allen et al., 1998; Allen, 2000). Using the PETVI approach to obtain daily values of T_r by using the smooth function of the phenology of a well-watered crop to obtain values for K_{cb} and K_c in-between days where vegetation indices and satellite-derived ET_a observations are not available.

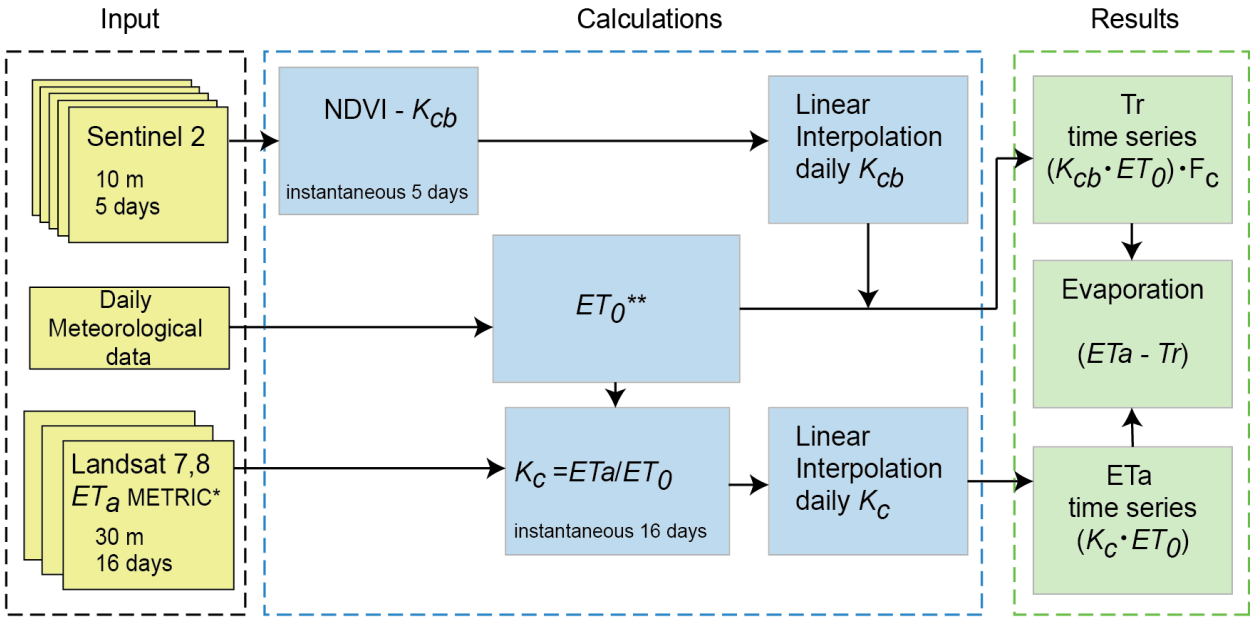

*Allen et al., 2007; ** Penman-Monteith, Allen et al., 1998.

Figure 3.4 workflow to estimate the variables needed in the PETVI method. This workflow diagram shows the input variables from left to right with yellow squares. Here are the required S-2 images, meteorological data, and ET_a images from Landsat using METRIC algorithms. In the center of the flow diagram are the basic calculations and procedures. Finally, in the green boxes are represented the results at the daily scale of T_r, ET_a, and last but not less significantly, the evaporation as residual from the subtraction of the T_r of ET_a.

3.3 Results

3.3.1 Dynamics of Evapotranspiration (ET_a) during the growing cycle in furrow-irrigated fields.

In the observation plots with furrow irrigation (F1 and F2), evaporation (E_v) occurs in two different periods (Figure 3.5). The first period occurs at the beginning of the agricultural cycle, which starts from day 75 and goes until day 150. The second period begins when the crop enters senescence, which occurs from day 245 until the harvest date around day 280 approximately. The evaporation in the first period for both plots was different; plot F1 E_v was 166 mm and F2 E_v was 91 mm. For the second period, F1 E_v was 164 mm and F2 E_v was 181 mm. Although planting dates were different at each site, (similar timing of crop emergence as revealed by the transpiration signal) total T_r for both parcels was very similar (F1 T_r = 500 mm and F2 T_r = 550 mm). In both sites, transpiration dominates ET_a fluxes from day 150 to day 250. However, the evaporation totals between sites differ significantly; for F1 E_v was 380 mm while for the F2 E_v was 300 mm. This difference in E_v between sites was caused by an evaporation peak in the F1 site around days 160 to 170 and to the fact that the transpiration in the F2 makes the entirety of ET_a during that period. In both sites, most of the water irrigated was delivered before the rainy season, with a final irrigation delivered at the end of the rainy season. Analysis of surface water balances (SW) at both sites show that both plots end up with excess water, although in one plot SW is significantly higher (F1 SW = 350 mm and F2 SW = 450 mm). The difference in SW between F1 and F2 is due to the greater evaporation in F1 relative to F2.

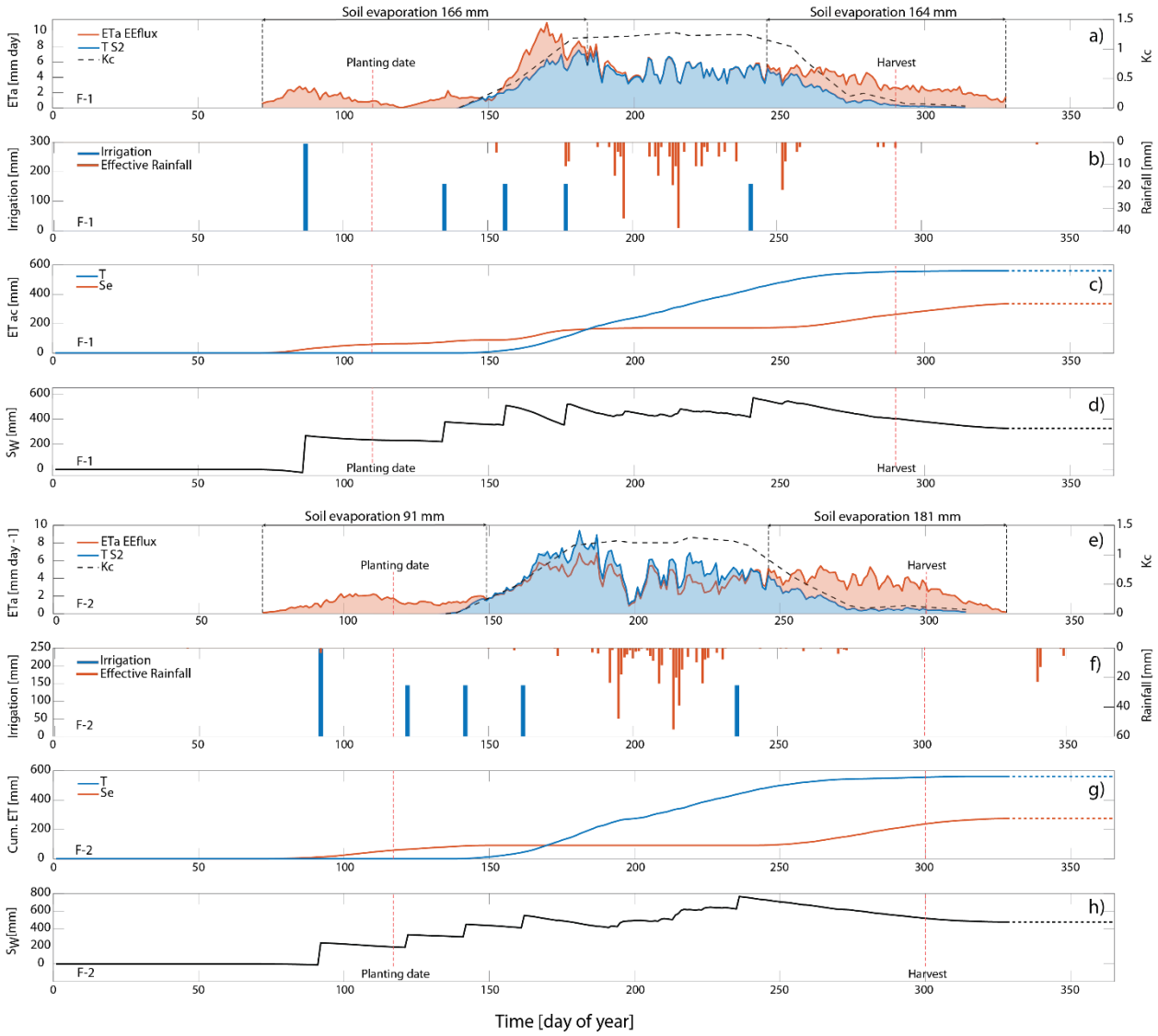

Figure 3.5 Hydrological fluxes in observation parcels with furrow irrigation system for sites F-1 and F-2. (a, e) showing the behavior of Evapotranspiration [ET mm d^{-1}; orange line], and Transpiration [T mm d-1; blue line]. Soil evaporation is shown as a shaded orange region. The black dashed line shows the basal crop coefficient; (b, f) show the main water inputs to the parcel; effective rainfall [mm; orange bars], and irrigation events [mm; blue bars]; (c, g) show the cumulative Transpiration [mm; blue line] and Evaporation [mm; orange line], the dashed horizontal lines indicate the absence of analysis at the end of the cycle; (d, h) show the surface water balance (P-ET [mm]) at the plot scale, the dashed line indicates the absence of analysis in the final of the period and the dashed vertical lines in orange show the planting and harvest dates.

3.3.2 Dynamics of Evapotranspiration (ET_a) during the growing cycle in sprinkler-irrigated fields.

The observation sites equipped with sprinkler irrigation (S-1 and S-2) showed a behavior similar to the previously described sites related with evaporation periods (Figure 3.6). The first period occurred during the beginning of the establishment and development of the crop between days 72 and 180; the second period occurred when the crop begin dormancy until the day 280 harvest period. The Ev in the first period for S-1 was 215 mm; in the second period, Ev was 193 mm. For site S-2, Ev in the first period was 240 mm and second period was 187 mm. Planting dates for S-1, and S-2 were around day 110. Total evaporation and transpiration are very similar in both sites despite irrigations being delivered with different frequencies and amounts (S-2 irrigations were more frequent and with smaller amounts than S-2). Irrigation management did not affect the proportion of ETa in both plots. However, the frequencies and amounts of irrigation had evident repercussions in the SW. Reviewing the behavior of the water balance in S-1, SWB remained almost neutral, while for S-2, the water balance maintained excess water before the rainy season; even after the rainy season, it was delivered the last irrigation, this increased the moisture content at the end of the cycle in both sites (S-1, SW = -0 and S-2, SWB = 150). Therefore, the SW difference between S-1 and S-2 was due to the differences in the operation of irrigation.

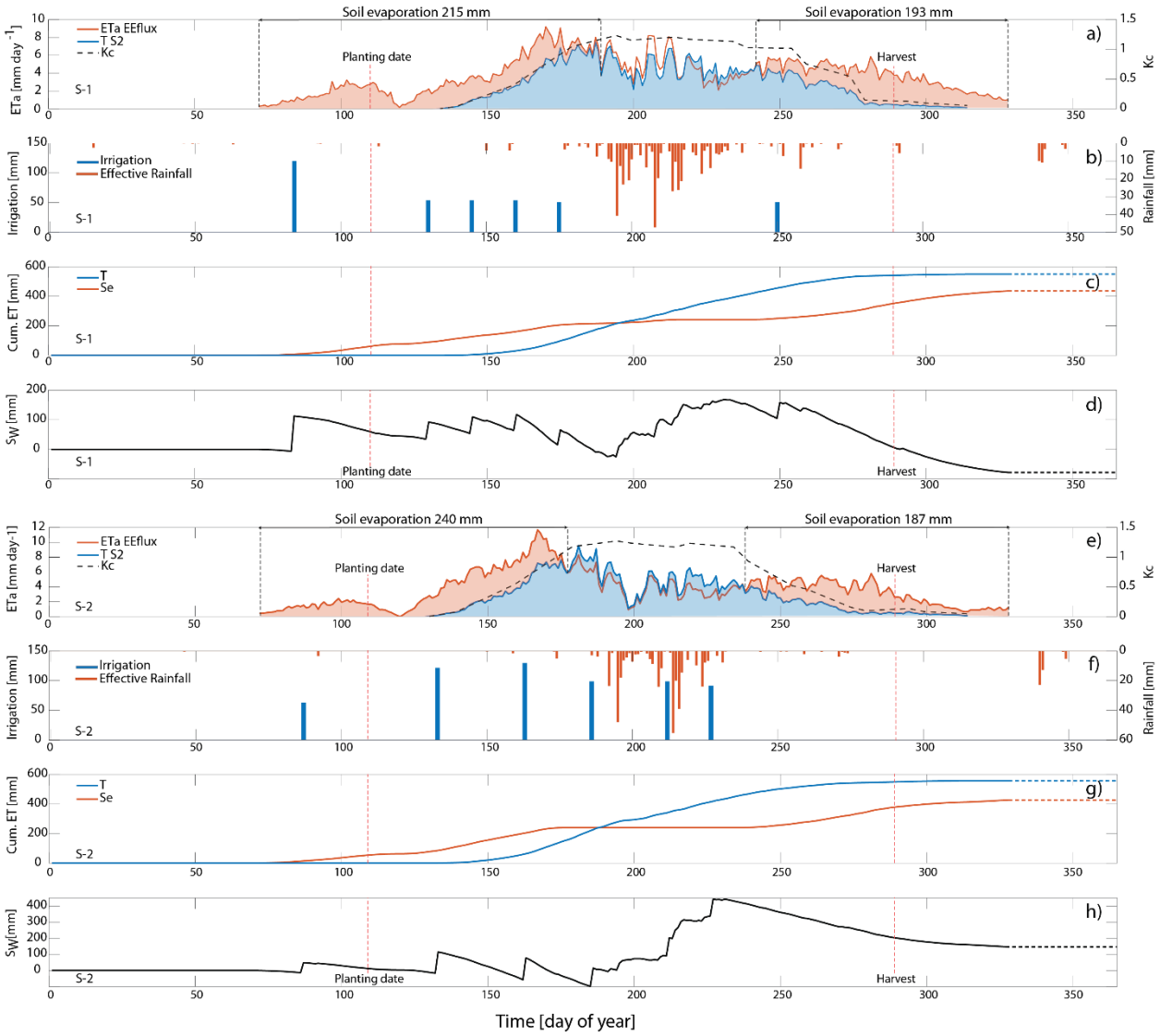

Figure 3.6 Hydrological fluxes in observation parcels with sprinkler irrigation systems for sites S-1 and S-2. (a, e) showing the behavior of Evapotranspiration [ET mm d^{-1}; orange line], and Transpiration [T mm d^{-1}; blue line]. Soil evaporation is shown as a shaded orange region. The black dashed line shows the basal crop coefficient; (b, f) show the main water inputs to the parcel; effective rainfall [mm; orange bars], and irrigation events [mm; blue bars]; (c, g) show the cumulative Transpiration [mm; blue line] and Evaporation [mm; orange line], the dashed horizontal lines indicate the absence of analysis at the end of the cycle; (d, h) show the surface water balance (P-ET [mm]) at the plot scale, the dashed line indicates the absence of analysis in the final of the period and the dashed vertical lines in orange show the planting and harvest dates.

3.3.3 Dynamics of Evapotranspiration (ET_a) during the growing cycle in drip-irrigated fields.

Among all available irrigation systems, drip irrigation and particularly subsurface drip irrigation is the most efficient in delivering only the required water to crops, with maximum operation efficiencies of ~95%. In the two observation plots equipped with subsurface drip irrigation that were evaluated in the study (D-1 and D-2), we expected lower E_v totals than for the previously described systems. However, both the dynamics and totals of E_v maintain a similar pattern with two periods of E_v (Figure 3.7); one at the beginning and the end of the cycle. The first period occurred from day 75 to 175, and the second period occurred when the crop began the senescence period, from day 240 to harvest season. At D-1, E_v was 284 mm and 186 mm for the first and second periods respectively; at D-2, E_v was 137 mm, and 157 mm for the first and second period respectively. On the other hand, while T_r totals were remarkably similar at both sites (~ 550 mm), the high E_v recorded at D-1 during the first period yielded large differences in E_v totals between the observation plots (470 mm and 294 mm for D-1 and D-2 respectively). Differences in irrigation observed between both sites may help explain the disparities in E_v totals: at D-1, irrigation was more frequent throughout the entire crop development, stopping right before the start of the rainy season and favoring an E_v peak between days 130 to 175. With respect to the surface water balance (*SW)*, we found a large difference at the end of the growing cycle between both sites, D-1 *SW* ended at 98 mm and D-2 *SW* ended at 230 mm. The difference between *SW* is because a large amount of evaporation occurs during the crop development period in D-1.

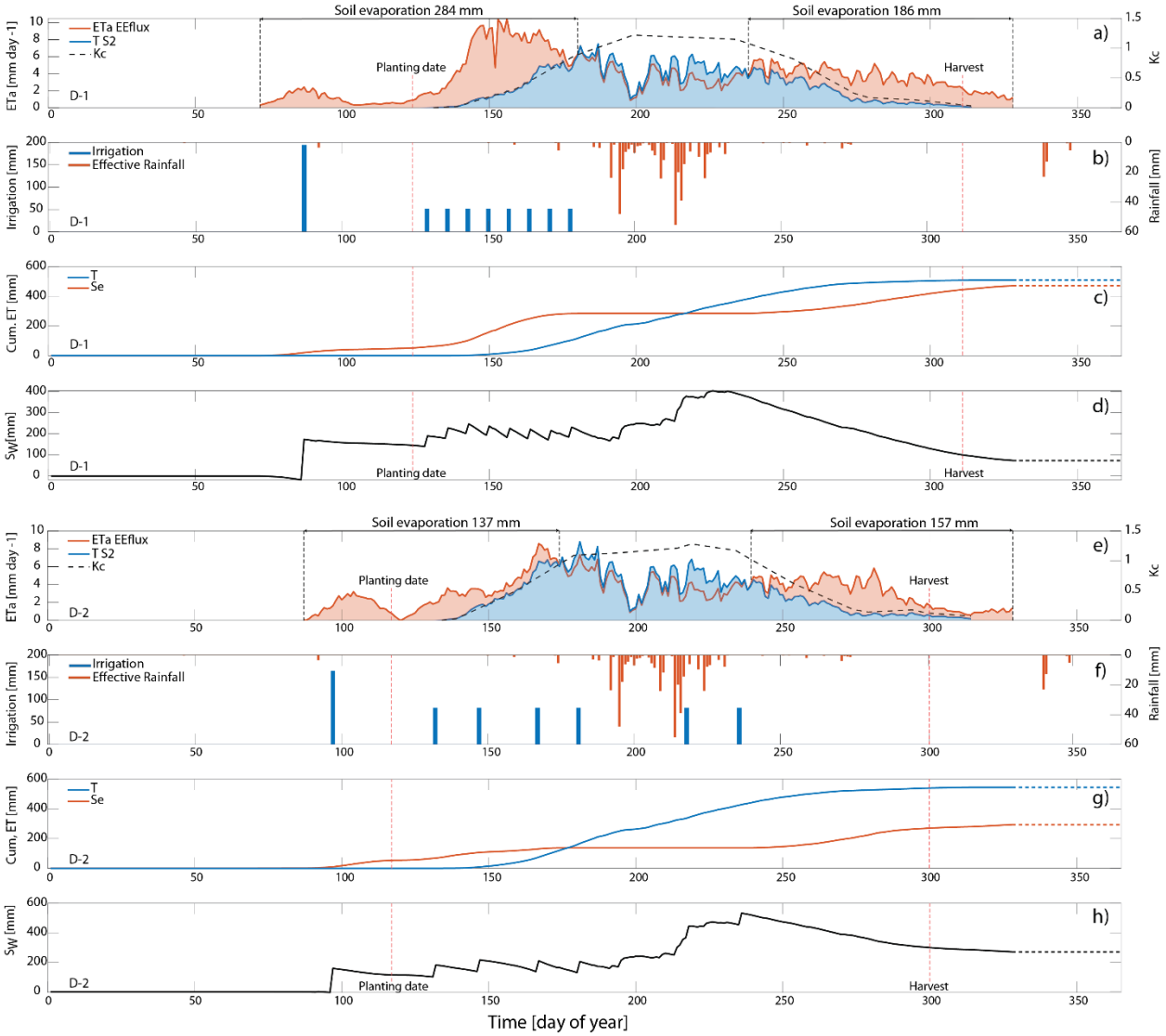

Figure 3.7 Hydrological fluxes in observation parcels with drip irrigation systems for sites D-1 and D-2. (a, e) showing the behavior of Evapotranspiration [ET mm d^{-1}; orange line], and Transpiration [T mm d^{-1}; blue line]. Soil evaporation is shown as a shaded orange region. The black dashed line shows the basal crop coefficient; (b, f) show the main water inputs to the parcel; effective rainfall [mm; orange bars], and irrigation events [mm; blue bars]; (c, g) show the cumulative Transpiration [mm; blue line] and Evaporation [mm; orange line], the dashed horizontal lines indicate the absence of analysis at the end of the cycle; (d, h) show the surface water balance (P-ET [mm]) at the plot scale, the dashed line indicates the absence of analysis in the final of the period and the dashed vertical lines in orange show the planting and harvest dates.

3.3.4 Relative contribution of the Evaporation (E_v) component into total Evapotranspiration (ET_a).

The rainfall season in the study area begins in early June, at a time when the crops have attained their maximum development. This means that from the start of the sowing period farmers use groundwater to irrigate their crops at least until late May, which is the period when E_v has the most significant contribution to the total ET_a. This pattern occurs on all six observation plots with slight variations on the E_v/ET_a ratio (Figure 3.8.a-f). In plot F-1, after the second irrigation, E_v/ET_a decreases to almost zero on day of year (doy) 150, but after the third irrigation is applied, the E_v contribution to ET_a, quickly increases; a similar behavior occurs in F-2 (Figure 3.8b). In the case of the sprinkler irrigation system (Figure 3.8. c, d) E_v/ET_a shows a gentler decrease relative to that of F-1 and F-2, where $E_v/ET_a = 0$ is reached on doy 180. On the drip irrigated plots (Figure 3.8.e, f) a similar E_v/ET_a behavior to sprinkler irrigated plots is observed, but with some differences inherent to their operation; during the early season the farmer delivered water on a highly frequent basis, increasing the availability of water for direct soil evaporation and increasing the E_v contribution to the ET_a. After that, E_v/ET_a slowly decreased until reaching zero values on doy 180, and then the crop continued with their physiological activities using water from rainfall. In plot D-2, nonproductive water use occurred early in the growing season but with clear differences to D-1. In D-2 irrigation was applied at larger intervals than in D-1, and E_v/ET_a went to 20% quickly after the third irrigation, and to 0% after the fourth irrigation around doy 180. The analyses show that unproductive water use occurs when most of the water comes from groundwater and when the rainfall season begins most of that water is used by the crop (i.e. productive water). Also, the last irrigation on the six observation plots is delivered close to the physiological maturity in the last

stretch of the growing season. At that period, the crop's water demand is reduced significantly, and the E_v/ET_a ratio increases up to 100 % at the end of the cycle.

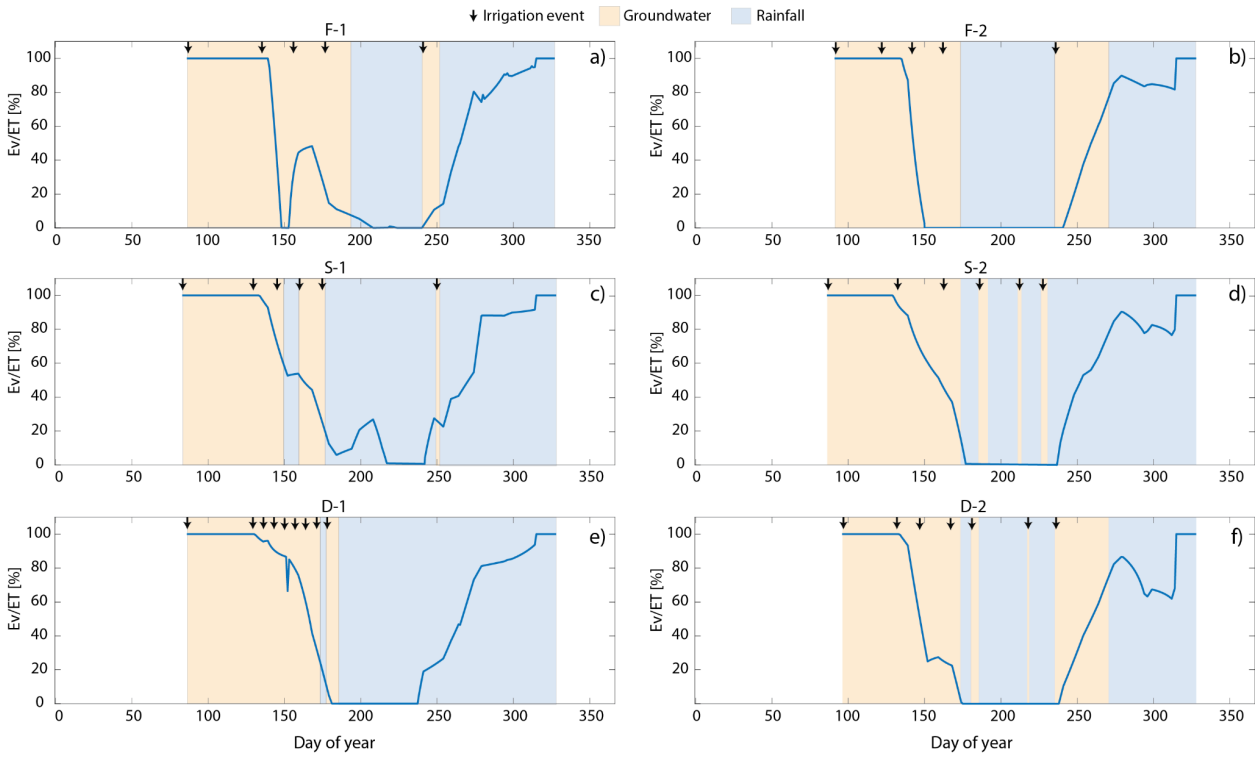

Figure 3.8 Evaporation ratio (E_v/ET) displaying the contribution of soil evaporation (E_v) to the total Evapotranspiration (ET). a) and b) show the E_v/ET in the sites with furrow irrigation (F-1 and F-2); c) and d) show the E_v/ET relationship in the parcel with sprinkler irrigation systems (S-1 and S-2); e) and f) show the E_v/ET in the parcels using drip irrigation. The blue line shows the evolution of E_v/ET during the observation period. The light orange shaded area shows the period when groundwater was used for irrigation, and the blue-shaded regions shows the period when water came from rainfall.

3.3.5 Impact of agricultural practices at the basin level

Derived the parcel scale analysis of the irrigation systems operation; this result is essential to know how the water use at the basin scale. To do this analysis, we extrapolated the found results

using the area of corn under irrigation reported by (Santos-Hernandes et al., 2019). To see the performance of this analysis of the operation of the irrigation systems at plot scale corresponding to F-1 and F-2, we averaged transpiration, soil evaporation, and water inputs (precipitation and groundwater), and we extrapolated them. The same procedure it realized for the other observation plots. The results are in figure 8.a), the water volumes used to extrapolate the findings in the observation sites' we assume a similar performance to the sampled areas. The water volume used by transpiration in the furrow irrigation system was recorded at 247 hm^3, 136 hm^3 corresponding to evaporation, and 157.93 hm^3 as excess water. On the other hand, we quantified the water inputs; groundwater consumption at 391.45 hm3 , and the rainfall contribution was 150.02 hm^3 ; to know the potential water savings, we use the maximum potential efficiency for furrow irrigation This means to satisfy the water volume of 247.39 hm^3 demanded by transpiration using the 55 % of efficiency it is necessary to use 449.80 hm^3, even with this efficiency and evaluating the contribution of rainwater of 150.02 hm^3 and completing it with groundwater 299.80 hm^3 to meet the water needs of the crop is possible to generate potential water saving of 91.67 hm^3. Figure 3.9 b) shows the results of the extrapolated values analysis in the area occupied by sprinkler irrigation; the results are shown in the same units of measurement, but a magnitude difference in the values due to the occupied area by the sprinkler irrigation. The water output of the system using the averages of the individual plots of sprinkler irrigation is given by transpiration that amounts to 9.71 hm^3 and estimated evaporation at 7.63 hm^3 to satisfy this demand. The system uses the water from rain 7.52 hm^3 and 9.74 hm^3 of groundwater (pink color). Following this analysis, a scenario was performed managing the irrigation system with a theoretical efficiency of 80%. The water demand due to transpiration remains constant at 9.71 Hm3 with this efficiency, and after satisfying the water need due to transpiration, a volume of 2.43 hm3 of excess water is observed. On the

other hand, if we manage the irrigation system as close to the theoretical efficiency and consider the contribution of rainwater as 7.52 hm3, it will only be necessary to use 4.72 hm^3. This management will allow a perception of a potential water saving of 5.12 hm^3.

Finally, the analysis for drip irrigation at the basin scale using Figure 3.9 c) the average data from individual observation plot. We calculated the water output in transpiration, evaporation, and excess water. Transpiration represents 6.90 hm^3, evaporation 5.04 hm^3 and excess water 1.48 hm^3. To satisfy these crop water demands, extracting 8.34 hm^3 of groundwater and the water from rainfall of 5.10 hm^3 is necessary. When we create the scenario with potential irrigation efficiency of 95%, we can see encouraging results. The water necessary to satisfy the transpiration needs of 6.90 hm^3, and the use of groundwater of 7.27 hm^3 without considering the contribution of rain; that is, there are 0.37 hm^3 of excess water. Nevertheless, considering the contribution of rainwater of 5.10 hm^3, it only estimates an extraction of groundwater of 2.17 hm^3. Suppose these results are consistent with the reality of what happens with the water management at the basin level. In that case, it is alarming to know the amount of water used in intensive agriculture in an unsustainable way. Moreover, the productive water use efficiencies with which the systems are operated should not be allowed for the degree of overexploitation of the aquifer.

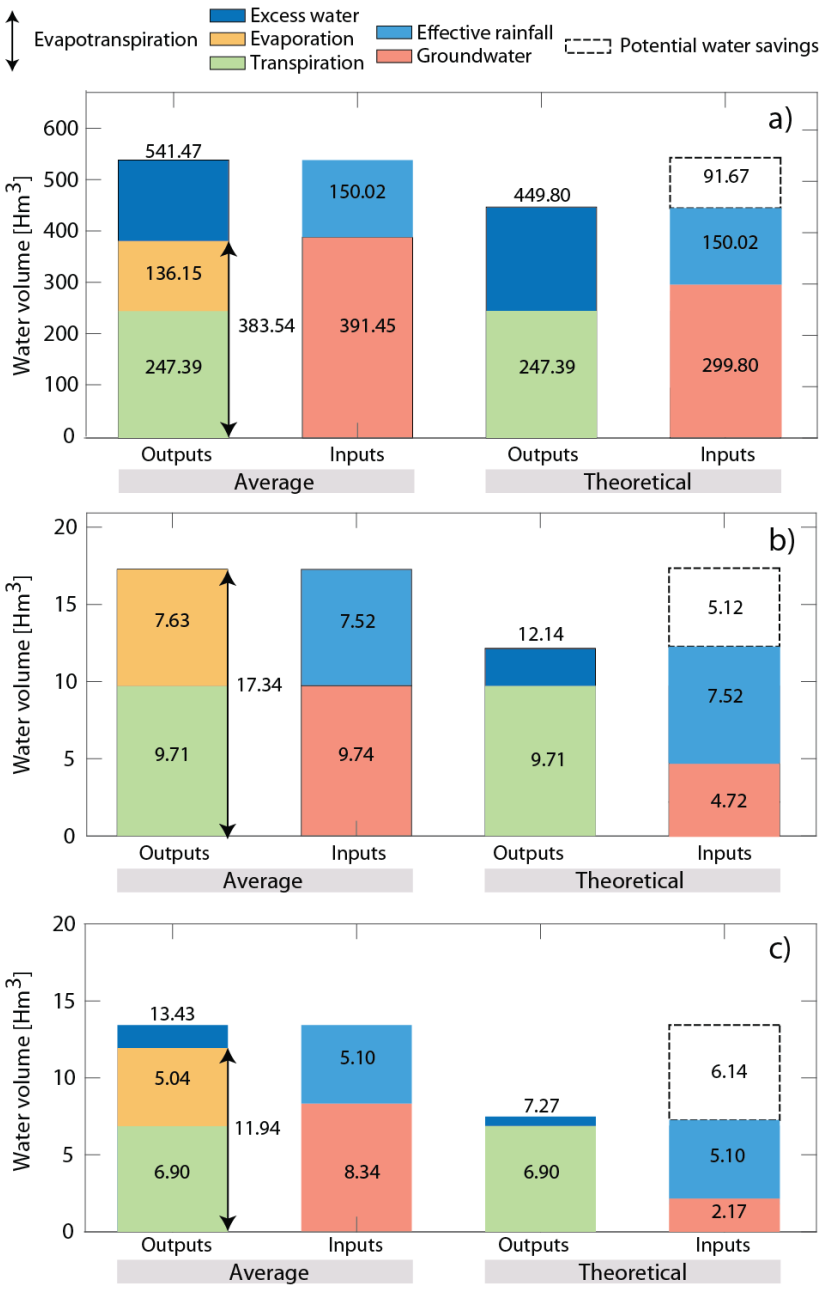

Figure 3.9 Extrapolation analysis of the impact of the agricultural practices at basin scale; a) average behavior of the furrow irrigation based on F-1, and F-2; b) average behavior of the sprinkler irrigation based on S-1 and S-2; c) average behavior of drip irrigation based on D-1 and D-2. In all panels the two bars on the left show the average values considering current operation efficiencies, while the right-side bars show the theoretical water use considering the maximum theoretical efficiency for those irrigation systems.

.

3.3.6 The behavior of soil evaporation during the interval between pre-sowing irrigation and sowing date in the six observation plots

We analyzed the amounts (cumulative) of unproductive water use for the observation sites (Figure 3.10) during the time interval between pre-sowing irrigation and sowing (TI-PS-S). The amount of unproductive water in Site S-1 during TI-PS-S was 54.31 mm; it corresponds to 45% of the total water delivered during the pre-sowing; 75% of nonproductive water was reached at 21 ***days after pre-sowing irrigation*** (DAPI). Unproductive water on S-2 was calculated at 40.63 mm; this represents the 64 % of delivered water in the pre-sowing irrigation, the 75% of the unproductive water was reached in 17.5 DAPI. Site F-1 had a cumulative unproductive water of 35.63 mm; this is equivalent to 12 % of the total water delivered in the pre-sowing irrigation, 75 % of unproductive water was recorded during 13 DAPI. Site F-2 had a cumulative soil evaporation value of 47.31 mm, equivalent to 19 % of the total water delivered in the pre-sowing irrigation; 75 % occurred during 18 DAPI.

Site D-1 in this site recorded 34.14 mm of soil evaporation, equivalent to 17 % of the water delivered in the pre-sowing irrigation; 75% of the soil evaporation occurred during 22 DAPI. Site D-2 has cumulative soil evaporation recorded at 45.42 mm; this value corresponds to 27 % of the water delivered by the pre-sowing irrigation. 75 % was recorded during 13.5 DAPI. The average time between the pre-sowing irrigation and the sowing date is around 25.5 days. The analysis shows that, on average, 50 % of soil evaporation occurs 11 DAPI. This analysis allows us to glimpse the opportunity to develop techniques that will enable the saving of 50% of unproductive water in the early stages of the agricultural cycle.

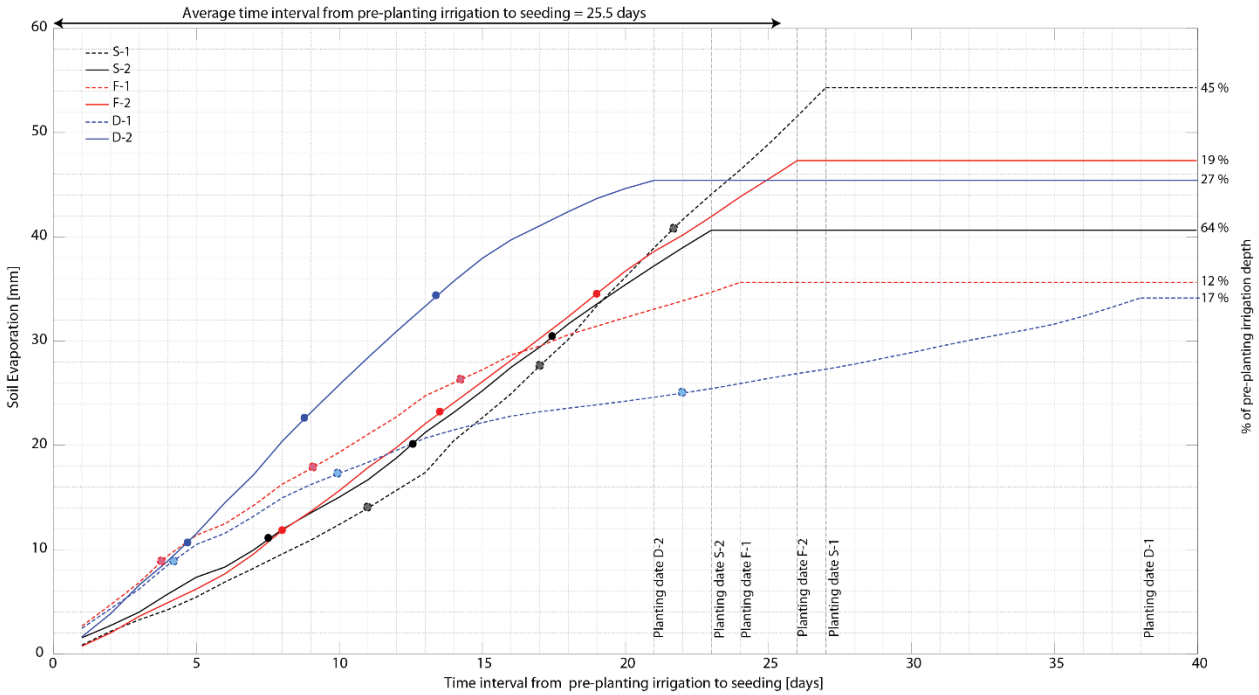

Figure 3.10 Cumulative soil evaporation and the period between pre-sowing irrigation and the sowing date for: sprinkler irrigated parcels S-1 (black dashed line) and S-2 (black line); furrow irrigated parcels F-1 (red dashed line) and F-2 (red line); drip irrigated parcels D-1 (blue dashed line) and D-2 (blue line). Bottom, middle, and top points on each line represent 25, 50, and 75 % of the cumulative soil evaporation.

3.3.7 Impact of irrigation operation on water balance at parcel scale

To analyze the impact of irrigation operations on the water balance of the observation plots we separated the components of the water inputs and outputs in each site. Water inputs consisted of two primary sources, groundwater and rain; the sites with the highest use of groundwater were the plots with irrigated by furrows (F-1 = ~1,200 mm, F-2 = 1,232 mm), followed by the fields irrigated with subsurface drip (D-1 = ~990 mm, D-2 = ~1,050 mm), and lastly by sprinkler irrigation (S-1 = ~850 mm, S-2 = 980 mm). The productive use of water (i.e. transpiration), showed very similar values on all six sites regardless of irrigation mode and averaged ~ 542 mm for the entire agricultural cycle. Unproductive use of water (i.e. E_v), was highest on the sprinkler irrigated

fields (S1= 547 mm, S-2 = 575 mm [soil E_v + E_v canopy]), followed by drip irrigated (D1= 470 mm, D-2 =294 mm), and the furrow irrigated plots with the least E_v (F-1= 330 mm, F-2 = 271 mm). Residual runoff or deep soil moisture percolation was highest on the furrow irrigated fields (F-1 = 325 mm, F-2 = 422 mm), followed by drip irrigated (D-1= 61 mm, D-2 = 149 mm) and sprinkler irrigated fields (S-1 = ~ 0 mm and S-2 = 129 mm). This last component clearly shows how the management of the irrigation amounts directly affects the E_v, runoff, and percolation without significantly affecting the T_r values.

Figure 3.11Water balance in the observation plots. a) main water inputs (red color is rainwater and blue is groundwater); b) water input proportion (in %) of rainwater and groundwater; c) use of water by the transpiration component; d) outflow of water from the system due to soil evaporation (light orange), evaporation of rainwater intercepted by the canopy (yellow), and evaporation of irrigation water intercepted by the canopy (purple color); e) runoff or percolation; f) proportion of water outputs (in %) by each component.

3.4 Discussion

3.4.1 Comparison of the observed efficiencies in three irrigation systems.

In this study, we explore the efficiency of three irrigation systems for corn production: subsurface drip, sprinkler, and furrow. Despite the overexploited condition of the aquifer comprising the main water source in the region, currently there are only a handful of modern irrigation systems in the agricultural valley. Drip irrigation systems can achieve considerably high efficiency if two essential characteristics are met; proper design and careful operation (Lamm & Trooien, 2003). Water loss through soil evaporation is an important factor in the inefficiency of irrigation systems (Evett et al., 2005). For instance, drip irrigation's efficiency depends largely on soil evaporation losses from saturated soil and to a lesser extent on deep moisture percolating into the soil profile (Wang et al., 2013; Zhang et al., 2019). However, improved drip methods such as subsurface irrigation can reduce the inefficiency of the drip irrigation systems (Meshkat et al., 2000). A study by Irmak et al., (2011) show a maximum attainable efficiency (i.e. theoretical efficiency) by subsurface drip irrigation of more than 95%. In the study area, we found much lower efficiencies relative to that theoretical efficiency. For example site D-1 equipped with subsurface drip irrigation had an actual efficiency of 46%. This low-efficiency value can be attributed to high evaporation losses of around 48% in addition to 6% losses from percolation or runoff. In observation site D-2 the efficiency was 47%, one percentage point higher than site D-1. In this case, 31% of the irrigated water was lost to evaporation and 22% was lost to percolation or runoff. Percolation or runoff values in our observation plots varied from 6% to 22% and are within the range of those reported by Nassah et al., (2018), who found deep percolation values of 37 and 45% in drip irrigation. These high percolation or runoff values occur when there is a mismatch between

irrigation and the crop's water demands. On the other hand, water losses from soil evaporation in D-1 and D-2 (48% and 31% respectively) are comparable to evaporation losses in the range of 48% to 57% in studies of crops without mulching (Jia et al., 2021). Operating the drip system at an irrigation efficiency of 47% resulted in similar efficiency to furrow irrigation. The evidence shown in this study suggests that technification of irrigation without proper operation of the systems does not improve water conservation.

The sprinkler irrigation systems in this study showed an efficiency of 50% for S-1 and 44% for S-2. These values are comparable with a ~ 42 % efficiency found by Wang et al., (2012), from a winter wheat irrigated with sprinkler irrigation in the southern part of the Shanxi Province with similar weather conditions to our study site. These reported efficiencies are relatively low compared to the maximum or potential efficiencies for this irrigation system of 75 to 85% (Irmak et al., 2011). In site S-1, the 50% efficiency is because part of the water delivered to the system is lost through the Evaporation component. In the observation plot S-2, the efficiency recorded is 44%. It decreased by 6% concerning S-1 due to water output by percolation or runoff component at 10%, and the evaporation rate was accounted for at 34%. In the plots with furrow irrigation, the efficiency for the F-1 site was recorded at 44%, and for the F-2 site at 42%. These data can be compared with those reported by Wang et al., 2012, who documented values of efficiency for this irrigation method of 38%, Bakker et al., (2006) of 36%, Slatni et al., (2011), who reported 44%, also Reddy et al., (2013) found an irrigation efficiency of 48 %, Masseroni et al., (2022) found a range from 16 to 56 %, and Reddy et al., (2013) found an average 48 % of irrigation efficiency and 39 % of runoff loss. These efficiency values are low concerning potential efficiency for furrow irrigation 45 to 65% (Irmak et al., 2011). The efficiencies found in the study site are low due to the large portion occupied by percolation or runoff. For Site F-1, the percolation or runoff was 25

%, and for the site, F-2 was recorded as up to, 32%. These results can be compared with (Huang et al., 2022), who found the 18 to 25 % loss of water from irrigation as runoff, another factor that reduces irrigation efficiency was 40% as evaporation. These values can be attributed to over-irrigation. The result we found in the observation sites, can not be attributed to the irrigation system. However, this reflects their farmer's field operation, which does not have an irrigation schedule and no in situ soil moisture measurement to help manage the water most efficiently. The farmers apply irrigation based on their empirical knowledge. This reflects the deficiency or lack of training. In addition to the fact that there is no charge for the volume of water used, the only incentive for the efficient use of water is the reduction of energy expenditure to reduce the production costs of the crop.

3.4.2 Effect on the different types of irrigation in the partition of the water balance.

Attaining high water use efficiency in agriculture means supplying crop water needs without leaving excess water that would evaporate, runoff or percolate deep (past the root zone) in the soil. On average, the total amount of water required in a season for corn transpiration is estimated at ~542 mm. In an ideal scenario, farmers would deliver approximately the crop water demand considering the natural contribution of rainfall and irrigation water. However, our findings reveal that the water delivered to the parcel by irrigation plus the contribution from rainfall largely exceeds the crop's water requirements. On average, the water delivered at the observation sites is ~ 1,170 mm (irrigation + rainfall). In all cases, the majority of the water not used by the crops is lost to evaporation, with differences among sites depending on the irrigation system and its operation: site D-1 recorded 440 mm, site D-2 363 mm, site S-1 554 mm, S-2 576 mm, sites F-1

421 mm, and F-2 349 mm. Furrow irrigation shows the lowest values of evaporation, with larger amounts of runoff or percolation compared to the other observation sites. Our observations indicate that the low performance of the different irrigation systems in this study is the result of their deficient operation.

3.4.3 Non-productive water use (beginning or end of the agricultural cycle)

Nonproductive water in our observation sites occurs during the beginning and end of the agricultural cycle. The larger amount of non-productive water occurs immediately after systematic pre-sowing irrigation. The higher evaporation values during the early growth stages compared to those at the end of the crop cycle are due to higher temperatures and wind speeds. The nonproductive water in sites D-1 and D-2 (42 and 25 % respectively), These values are significantly higher than ~ 15 % of Ev found by Nazari et al. (2021) who conducted the water delivered using subsurface drip irrigation in an apple orchard. The drip irrigation sites evaluated in this study did have comparable unproductive water to that reported by Yunusa et al., (2004) with soil evaporation comprising up to 64 % of the total water inputs (i.e. rainfall + irrigation) in vineyards. Because the observation sites in our study are equipped with subsurface drip irrigation, we expected that the soil evaporation would be minor; however, the data shows high values of soil evaporation. These evaporation values could be attributed to deficiencies in the schedule of irrigation as well as in the total amounts of irrigation delivered. Water delivered at site D-1 was up to ~1,110 mm, and D-2 ~1,158 mm (grounwater plus rainfall), while the the total nonproductive water in site D-1 was 470 mm, and site D-2 was 294 mm. During the early season, the daily nonproductive water ranged from 0.08 to 3.51 mm day^{-1}, similar to Kerridge et al., (2013) values

ranging from 0.69 and 2.52 mm day^{-1} of soil evaporation from inter rows (bare soil) in a grapevine field using drip irrigation. Soil evaporation in drip irrigation systems can yield the same values as surface irrigation techniques when large irrigation amounts are applied (Guo et al., 2022). In other words, the amounts of water deliveries are important to maximize the water use efficiency; when the irrigation water amounts increase the water use efficiency decreases (Yang et al., 2020). Careful management of subsurface drip irrigation can reduce the net water amount of water delivered and minimize the nonproductive water and drainage (Lamm et al., 1995). However, an excessive regime of high irrigation can cause wet soil surface, resulting in water loss (Meshkat et al., 2000). One of the main purposes of irrigation technification is improving the water delivery to the crops for the maximization of yield and water savings, and in the process reducing the nonproductive water use (evaporation). However, studies by Zhou et al., (2021) show that in some instances, new irrigation techniques reduce the nonproductive water, but increase the return flow (recoverable and unrecoverable water) more than the accumulated soil evaporation, when some water management deficiencies occur at the plot scale.

Sprinkler irrigation is the other technique the farmers implemented in the agricultural valley. However, due to the nature of the system, the canopy and bare soil are the key components to increasing the nonproductive water (evaporation Losses) (Mattar et al., 2022); in our observation sites, soil evaporation occurs during the early of the growing season particularly when the crops do not completely cover the soil, and large portions of bare ground are exposed to the elements. When the soil is finally covered by the canopy, in crops irrigated by sprinklers, a percentage of the water irrigated is intercepted by the canopy and evaporated directly there (Uddin et al., 2013). In site S-1, nonproductive water during the agricultural cycle was recorded at 40 % from soil evaporation and 10 % from water intercepted by the canopy. During the early season, the amount

of nonproductive water was 215 mm, and 173 mm at the end of the season. In site S-2, the nonproductive water from soil evaporation was 34% and 12 % from intercepted water from irrigation; the evaporation water amount during the early season was 240 mm and at the end of the season was 172 mm.

Furrow irrigation is both the theoretically least efficient system and the most used method to deliver water to the parcels due to the low cost, and low technical knowledge required for operating it. On site F-1 26 % of the water delivered to the observation was nonproductive water turned into evaporation, while for F-2 that number was 20 %. For these two sites, evaporation was significantly lower relative to the sites with drip and sprinkler systems. However, the portion of nonproductive water lost as deep percolation was significantly higher than on the drip and sprinkler sites. Water lost as deep percolation or runoff is not used by the crop. For these two sites, the increased percolation or runoff for site F-1 the runoff or percolation was recorded at 25 %, and for F-2 site was 32 %. Also, the evaporation from canopy intercepted rainfall was 4% and 6% for F-1 and F-2 respectively. Taking the contribution from all components of the water balance, nonproductive water for the F-1 was 55%, and 58% for F-2. Seeda & El-Nour EAA (2020) reviewed furrow irrigation in Egypt and documented similar (~50%) amounts of unproductive water on wheat crops under furrow irrigation. This water loss is due to deficient irrigation management.

The six observation sites in this study showed a pattern of systematic pre-sowing irrigation with high water amounts delivered at the parcel. The cost of water delivered in the study region equates to the cost of pumping, and for that reason economic incentives to improve irrigation to conserve water are relatively low. Because the majority of the unproductive water that is lost to evaporation

is delivered early in the growing season, and because all of that water is pumped from the already overexploited aquifer, the best opportunities to improve irrigation efficiencies, minimize production costs and conserve water are to reduce irrigation during pre-sowing season. That could be achieved by reducing the time between the first irrigation and the planting date. Currently, the average time interval between pre-sowing irrigation and planting is 25.5 days. During this time the nonproductive water is up to 40 % of the water delivered at the parcel. Because planting date depends on the pre-sowing time, as well as on the amount of water irrigated and the soil texture and drainage of the cultivated area, planning for reducing the time interval between pre-sowing irrigation and planting date should take into account the variables described above as well as the cycle of the crop type (e.g. in this case hybrid late, medium, or short maize).

3.4.4 Impact of agricultural practices on water use at the basin-scale (potential savings)

Water supply problems for regions where agriculture and urban areas compete for water resources have intensified due to population growth, higher demands of food, the overexploitation of limited water resources and the impending effects of climate change driving higher water consumptions. This problem is particularly acute in regions where population centers and agricultural areas are located in desert or semi-desert environments (Hargrove et al., 2013). The repercussions of those phenomena are already surfacing; for example, Flörke et al., (2018) in a study conducted in 482 cities around the world, starting from a baseline of 1971 to 2000, found that 46% of the cities studied will experience a deficit of surface water, and in 41% of river basins, agricultural water user needs will be in conflict with cities due to water shortages to meet urban

and agricultural needs. Likewise, Molle and Berkoff, (2009), identified wasteful irrigation and bureaucratic inefficiency favoring water scarcity in urban areas. This situation is currently occurring in our study site (Laguna de Bustillos Basin), where water is supplied for urban use through 17 deep wells from which 12 Mm^3 $year^{-1}$ are extracted. Concurrently, water extractions to supply the agricultural fields on which the economy of the region depend are carried out amid severe problems for the supply of drinking water caused by the depletion of the aquifer and the marked decrease in static levels once the irrigation of crops adjacent to the city of Cuauhtémoc, Chihuahua start (Díaz et al., 2014). The situation described above represents a significant challenge for maintaining the current intensive agricultural economy of the region. A solution to this problem requires a more efficient use of water and to keep urban and agricultural water consumption as balanced as possible.

To evaluate the effect of the irrigation efficiencies on the total annual water consumption from the aquifer, we projected the total water use from agriculture by extrapolating the water use efficiencies estimated in the observation plots to the total area occupied by each irrigation systems in the agricultural valley, using three scenarios: 1) current observed efficiencies, 2) theoretical efficiencies, and 3) current observed efficiencies with a shortened time interval between pre-sowing irrigation and planting. Figure 3.12 shows three scenarios; bar a) represent the water volume in hm^3 to the current water management in the three different irrigation systems used to produce corn. Total water use by transpiration was 247.3 hm^3, 9.71 hm^3, and 6.9 hm^3 for furrow, sprinkler and drip irrigation, respectively; the large differences between these amounts is due to the fact that furrow irrigation occupies by far the largest area in the valley. The water use by evaporation was 136.2 hm^3 7.63 hm^3, and 5.06 hm^3 for furrow, sprinkler and drip irrigation,

respectively. Finally, the excess water for each scenario were 157.9 hm^3. Bar b) shows water management using theoretical efficiency. The main changes with respect to the evaporation component in the previous scenario were; furrow irrigation keeps the same values of 136.2 hm^3, Sprinkler irrigation reduces the evaporation to 2.43 hm^3, and drip irrigation reduces the evaporation close to zero; this resulted in water excess decreases of 66.26 hm^3, 41% less than with the current management. Finally, considering current efficiencies and the reduction between the time of the first irrigation and planting date, water excess is significantly reduced to up to 14.25 hm^3. In this instance, we have a decrease of water excess of 85.7 %. Considering the water requirement by urban consumers of Cuauhtemoc city, the second scenario using the irrigation system at maximum efficiency can save 91 hm^3. This hypothetical water savings is equivalent to the total water use by the city of Cuauhtemoc for ~ seven years. However, reducing the time of the pre-sowing irrigation to planting date would yield water savings of 143 hm^3, equivalent to ~ ten years of water demand for urban use.

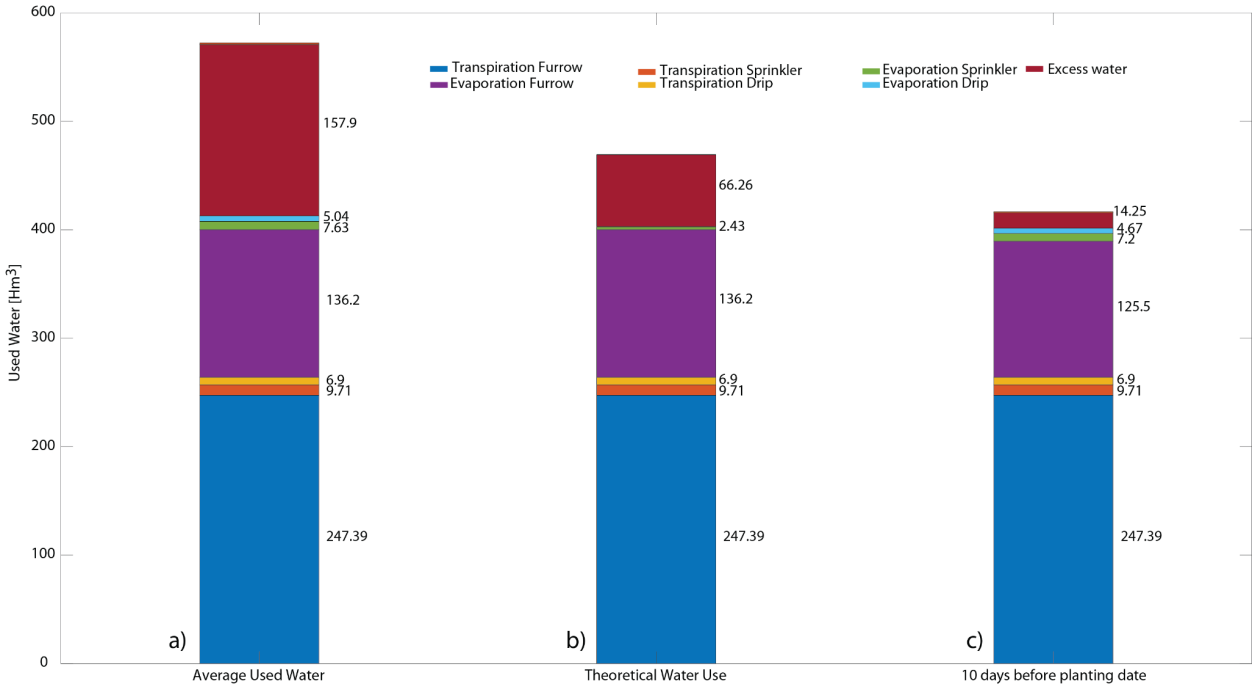

Figure 3.12 Water management scenarios at the basin scale; a) average of current water management; b) potential savings with irrigation systems operating at theoretical efficiencies; c) potential savings by reducing time intervals between pre-sowing irrigation and planting date.

3.5 Conclusion

In this study, we evaluated the productive water use efficiency of six observation plots with different irrigation systems and calendarization and assessed through the estimation of their productive and unproductive water use how those factors affected the water balance on each observation site. All sites displayed low productive water use efficiencies with more than half of the water applied is not used by the crop. These low productive water efficiencies sustain a level of stress on the water resources of a continuously declining and overexploited aquifer. Analyses of the times and magnitudes of productive and unproductive water use by the crops and the periods in which it occurs allows us to pay attention and implement water-saving alternatives as mentioned in the 3.5 section the maximum unproductive water occurs during the beginning of the agricultural cycle due to the systematic pre-sowing irrigation and the delay for the planting date. some

alternatives that can help us to increase the productive water can be reducing the time between the pre-sowing irrigation and planting date, and the other fact is the development campaign of extension related to activities on water management and schedule irrigation to increase the beneficial of modern irrigation system installed in the agricultural valley.

3.6 References

Ahadi, R., Samani, Z., & Skaggs, R. (2013). Evaluating on-farm irrigation efficiency across the watershed: A case study of New Mexico's Lower Rio Grande Basin. *Agricultural Water Management*, *124*, 52–57. https://doi.org/10.1016/J.AGWAT.2013.03.010

Alatorre, L. C., Díaz, R. E., Miramontes, S., Bravo, L. C., & Sánchez, E. (2014). Spatial and Temporal Evolution of the Static Water Level of the Cuauhtemoc Aquifer during the Years 1973, 1991 and 2000: A Geographical Approach. *Journal of Geographic Information System*, *06*(05), 572–584. https://doi.org/10.4236/jgis.2014.65047

Allen, R. G., & Pereira, L. S. (1998). Crop Evapotranspiration (guidelines for computing crop water requirements). *Irrigation and Drainage*, *56*.

Allen, R. G., Pereira, L. S., Howell, T. A., & Jensen, M. E. (2011). Evapotranspiration information reporting: I. Factors governing measurement accuracy. *Agricultural Water Management*, *98*(6), 899–920. https://doi.org/10.1016/J.AGWAT.2010.12.015

Allen, R. G., Tasumi, M., Morse, A., Trezza, R., Wright, J. L., Bastiaanssen, W., Kramber, W., Lorite, I. J., & C.W., R. (2007). Satellite-Based Energy Balance for Mapping Evapotranspiration with Internalized Calibration (METRIC)— Model. *Journal of Irrigation and Drainage Engineering*, *133*(4), 395–406. https://doi.org/10.1061/(ASCE)0733-9437(2007)133

Bakker, D. M., Plunkett, G., & Sherrard, J. (2006). Application efficiencies and furrow infiltration functions of irrigations in sugar cane in the Ord River Irrigation Area of North

Western Australia and the scope for improvement. *Agricultural Water Management*, *83*(1–2), 162–172. https://doi.org/10.1016/j.agwat.2005.12.004

CONAGUA. (2002). DETERMINACIÓN DE LA DISPONIBILIDAD DE AGUA EN EL ACUIFERO DE CUAUHTÉMOC CHIHUAHUA. *Comisión Nacional Del Agua*.

de Oliveira Costa, J., José, J. V., Wolff, W., de Oliveira, N. P. R., Oliveira, R. C., Ribeiro, N. L., Coelho, R. D., da Silva, T. J. A., Bonfim-Silva, E. M., & Schlichting, A. F. (2020). Spatial variability quantification of maize water consumption based on Google EEflux tool. *Agricultural Water Management*, *232*, 106037. https://doi.org/10.1016/J.AGWAT.2020.106037

Díaz Caravantes, R. E., Bravo Peña, L. C., Alatorre Cejudo, L. C., & Sánchez Flores, E. (2013). Análisis geoespacial de la interacción entre el uso de suelo y de agua en el área peri-urbana de Cuauhtémoc, Chihuahua. Un estudio socioambiental en el norte de México. *Investigaciones Geográficas, Boletín Del Instituto de Geografía*, *83*, 116. https://doi.org/10.14350/rig.32694

Evett, S. R., Colaizzi, P. D., & Howell, T. A. (2005). *DRIP AND EVAPORATION*. *02*. https://hdl.handle.net/10217/205462

Fader, M., Shi, S., von Bloh, W., Bondeau, A., & Cramer, W. (2016). Mediterranean irrigation under climate change: More efficient irrigation needed to compensate for increases in irrigation water requirements. *Hydrology and Earth System Sciences*, *20*(2), 953–973. https://doi.org/10.5194/hess-20-953-2016

García, G. M., Martinez, M. B., Humberto, A., & Silva, C. (2006). ESTADÍSTICAS CLIMATOLÓGICAS BÁSICAS DEL ESTADO DE CHIHUAHUA (PERIODO 1961-2003). In *Libro Técnico*.

Gleeson, T., Wada, Y., Bierkens, M. F. P., Ludovicus, &, & van Beek, P. H. (2012). *Water balance of global aquifers revealed by groundwater footprint*. https://doi.org/10.1038/nature11295

Gorelick, N., Hancher, M., Dixon, M., Ilyushchenko, S., Thau, D., & Moore, R. (2017). Google Earth Engine: Planetary-scale geospatial analysis for everyone. *Remote Sensing of Environment*, *202*, 18–27. https://doi.org/10.1016/J.RSE.2017.06.031

Guo, L., Cao, H., Helgason, W. D., Yang, H., Wu, X., & Li, H. (2022). Effect of drip-line layout and irrigation amount on yield, irrigation water use efficiency, and quality of short-season tomato in Northwest China. *Agricultural Water Management*, *270*, 107731. https://doi.org/10.1016/J.AGWAT.2022.107731

Hargrove, W. L., Borrok, D. M., Heyman, J. M., Tweedie, C. M., & Ferregut, C. (2013). Water, climate, and social change in a fragile landscape. *Ecosphere*, *4*(2). https://doi.org/10.1890/ES12-00269.1

Huang, Y., Zhang, Z., Li, Z., Dai, D., & Li, Y. (2022). Evaluation of water use efficiency and optimal irrigation quantity of spring maize in Hetao Irrigation District using the Noah-MP Land Surface Model. *Agricultural Water Management*, *264*. https://doi.org/10.1016/J.AGWAT.2022.107498

Huete, a, Didan, K., Miura, T., Rodriguez, E. P., Gao, X., & Ferreira, L. G. (2002). Overview of the radiometric and biophysical performance of the MODIS vegetation indices. *Remote Sensing of Environment*, *83*(1–2), 195–213. https://doi.org/10.1016/S0034-4257(02)00096-2

Hunsaker, D. J., Pinter, P. J., & Kimball, B. a. (2005). Wheat basal crop coefficients determined by normalized difference vegetation index. *Irrigation Science*, *24*(1), 1–14. https://doi.org/10.1007/s00271-005-0001-0

Irmak, A., Allen, R. G., Kjaersgaard, J., Huntington, J., Kamble, B., Trezza, R., & Ratcliffe, I. (2012). Operational Remote Sensing of ET and Challenges. *Evapotranspiration - Remote Sensing and Modeling*. https://doi.org/10.5772/25174

Irmak, S., Odhiambo, L. O., Kranz, W. L., & Eisenhauer, D. E. (2011). Irrigation Efficiency and Uniformity, and Crop Water Use Efficiency. *Biological Systems Engineering: Papers and Publications. 451.*, 1–8.

Jia, Q., Shi, H., Li, R., Miao, Q., Feng, Y., Wang, N., & Li, J. (2021). Evaporation of maize crop under mulch film and soil covered drip irrigation: field assessment and modelling on West Liaohe Plain, China. *Agricultural Water Management*, *253*, 106894. https://doi.org/10.1016/J.AGWAT.2021.106894

Jia, Z., Wu, Z., Luo, W., Xi, W., Tang, S., Liu, W. L., & Fang, S. (2013). The impact of improving irrigation efficiency on wetland distribution in an agricultural landscape in the upper reaches of the Yellow River in China. *Agricultural Water Management*, *121*(2013), 54–61. https://doi.org/10.1016/j.agwat.2013.01.003

Jiang, X., Kang, S., Tong, L., Li, F., Li, D., Ding, R., & Qiu, R. (2014). Crop coefficient and evapotranspiration of grain maize modified by planting density in an arid region of northwest China. *Agricultural Water Management*, *142*(2014), 135–143. https://doi.org/10.1016/j.agwat.2014.05.006

Kerridge, B. L., Hornbuckle, J. W., Christen, E. W., & Faulkner, R. D. (2013). Using soil surface temperature to assess soil evaporation in a drip irrigated vineyard. *Agricultural Water Management*, *116*, 128–141. https://doi.org/10.1016/J.AGWAT.2012.07.001

Konikow, L. F., & Kendy, E. (2005). Groundwater depletion: A global problem. *Hydrogeology Journal*, *13*(1), 317–320. https://doi.org/10.1007/S10040-004-0411-8/FIGURES/2

Laipelt, L., Henrique Bloedow Kayser, R., Santos Fleischmann, A., Ruhoff, A., Bastiaanssen, W., Erickson, T. A., & Melton, F. (2021). Long-term monitoring of evapotranspiration using the SEBAL algorithm and Google Earth Engine cloud computing. *ISPRS Journal of Photogrammetry and Remote Sensing*, *178*, 81–96. https://doi.org/10.1016/J.ISPRSJPRS.2021.05.018

Lamm, F. R., Manges, H. L., Stone, L. R., Khan, A. H., & Rogers, D. H. (1995). Water requirement of subsurface drip-irrigated corn in northwest Kansas. *Transactions of the American Society of Agricultural Engineers*, *38*(2), 441–448. https://doi.org/10.13031/2013.27851

Lamm, F. R., & Trooien, T. P. (2003). Subsurface drip irrigation for corn production: A review of 10 years of research in Kansas. *Irrigation Science*, *22*(3–4), 195–200. https://doi.org/10.1007/S00271-003-0085-3/FIGURES/6

López-Urrea, R., Montoro, a., González-Piqueras, J., López-Fuster, P., & Fereres, E. (2009). Water use of spring wheat to raise water productivity. *Agricultural Water Management*, *96*(9), 1305–1310. https://doi.org/10.1016/j.agwat.2009.04.015

Ma, Y., Liu, S., Song, L., Xu, Z., Liu, Y., Xu, T., & Zhu, Z. (2018). Estimation of daily evapotranspiration and irrigation water efficiency at a Landsat-like scale for an arid irrigation area using multi-source remote sensing data. *Remote Sensing of Environment*, *216*, 715–734. https://doi.org/10.1016/j.rse.2018.07.019

Martínez, B., & Gilabert, M. A. (2009). Vegetation dynamics from NDVI time series analysis using the wavelet transform. *Remote Sensing of Environment*, *113*(9), 1823–1842. https://doi.org/10.1016/J.RSE.2009.04.016

Mattar, M. A., Roy, D. K., Al-Ghobari, H. M., & Dewidar, A. Z. (2022). Machine learning and regression-based techniques for predicting sprinkler irrigation's wind drift and evaporation losses. *Agricultural Water Management*, *265*, 107529. https://doi.org/10.1016/J.AGWAT.2022.107529

Meshkat, M., Warner, R. C., & Workman, S. R. (2000). Evaporation reduction potential in an undisturbed soil irrigated with surface drip and sand tube irrigation. *Transactions of the American Society of Agricultural Engineers*, *43*(1), 79–86. https://doi.org/10.13031/2013.2690

Nassah, H., Er-Raki, S., Khabba, S., Fakir, Y., Raibi, F., Merlin, O., & Mougenot, B. (2018). Evaluation and analysis of deep percolation losses of drip irrigated citrus crops under non-saline and saline conditions in a semi-arid area. *Biosystems Engineering*, *165*, 10–24. https://doi.org/10.1016/j.biosystemseng.2017.10.017

Nazari, E., Besharat, S., Zeinalzadeh, K., & Mohammadi, A. (2021). Measurement and simulation of the water flow and root uptake in soil under subsurface drip irrigation of apple tree. *Agricultural Water Management*, *255*, 106972. https://doi.org/10.1016/J.AGWAT.2021.106972

Reyes-González, A., Kjaersgaard, J., Trooien, T., Reta-Sánchez, D. G., Sánchez-Duarte, J. I., Preciado-Rangel, P., & Fortis-Hernández, M. (2019). Comparison of Leaf Area Index, Surface Temperature, and Actual Evapotranspiration Estimated Using the METRIC Model and In Situ Measurements. *Sensors (Basel, Switzerland)*, *19*(8). https://doi.org/10.3390/S19081857

Santos-Hernández, A. L., Palacios-Velez, E., Mejía-Saenz, E., Matus-Gardea, J. A., Galvis-Spíndola, A., Vásquez-Soto, D., Ascencio-Hernández, R., & Peña-Díaz, S. A. (2019). Análisis del uso del agua del acuífero Cuauhtémoc, Chihuahua, México / Water use analysis in the Cuauhtemoc Aquifer, Chihuahua, Mexico. *Tecnología y Ciencias Del Agua*, *10*(3), 156–189. https://doi.org/10.24850/J-TYCA-2019-03-07

Schüttemeyer, D., Schillings, C., Moene, a. F., & de Bruin, H. a. R. (2007). Satellite-Based Actual Evapotranspiration over Drying Semiarid Terrain in West Africa. *Journal of Applied Meteorology and Climatology*, *46*(1), 97–111. https://doi.org/10.1175/JAM2444.1

Seeda, A. M., & El-Nour EAA, A. (2020). Management of Furrow Irrigation Technology and Its Risk Assessments: A review. *Middle East Journal of Applied Sciences*, *10*(04), 590–616. https://doi.org/10.36632/mejas/2020.10.4.51

Tennakoon, S. B., & Milroy, S. P. (2003). Crop water use and water use efficiency on irrigated cotton farms in Australia. *Agricultural Water Management*, *61*(3), 179–194. https://doi.org/10.1016/S0378-3774(03)00023-4

Toureiro, C., Serralheiro, R., Shahidian, S., & Sousa, A. (2017). Irrigation management with remote sensing: Evaluating irrigation requirement for maize under Mediterranean climate condition. *Agricultural Water Management*, *184*, 211–220. https://doi.org/10.1016/J.AGWAT.2016.02.010

Uddin, J., Smith, R. J., Hancock, N. H., & Foley, J. P. (2013). Evaporation and sapflow dynamics during sprinkler irrigation of cotton. *Agricultural Water Management*, *125*, 35–45. https://doi.org/10.1016/J.AGWAT.2013.04.001

Wang, P., Song, X., Han, D., Zhang, Y., & Zhang, B. (2012). Determination of evaporation, transpiration and deep percolation of summer corn and winter wheat after irrigation. *Agricultural Water Management*, *105*, 32–37. https://doi.org/10.1016/J.AGWAT.2011.12.024

Wang, Z., Zerihun, D., & Feyen, J. (1996). *General irrigation efficiency for field water management*. *3774*(32).

Wurl, J., Gámez, A. E., Ivanova, A., Imaz Lamadrid, M. A., & Hernández-Morales, P. (2018). Socio-hydrological resilience of an arid aquifer system, subject to changing climate and

inadequate agricultural management: A case study from the Valley of Santo Domingo, Mexico. *Journal of Hydrology*, *559*, 486–498. https://doi.org/10.1016/j.jhydrol.2018.02.050

Yang, X., Qin, Q., Yésou, H., Ledauphin, T., Koehl, M., Grussenmeyer, P., & Zhu, Z. (2020). Monthly estimation of the surface water extent in France at a 10-m resolution using Sentinel-2 data. *Remote Sensing of Environment*, *244*(May), 111803. https://doi.org/10.1016/j.rse.2020.111803

Yunusa, I. A. M., Walker, R. R., & Lu, P. (2004). Evapotranspiration components from energy balance, sapflow and microlysimetry techniques for an irrigated vineyard in inland Australia. *Agricultural and Forest Meteorology*, *127*(1–2), 93–107. https://doi.org/10.1016/J.AGRFORMET.2004.07.001

Zhang, W., Brandt, M., Wang, Q., Prishchepov, A. v., Tucker, C. J., Li, Y., Lyu, H., & Fensholt, R. (2019). From woody cover to woody canopies: How Sentinel-1 and Sentinel-2 data advance the mapping of woody plants in savannas. *Remote Sensing of Environment*, *234*(October), 111465. https://doi.org/10.1016/j.rse.2019.111465

Zhou, X., Zhang, Y., Sheng, Z., Manevski, K., Andersen, M., Han, S., Li, H., & Yang, Y. (2021). Did water-saving irrigation protect water resources over the past 40 years? A global analysis based on water accounting framework. *Agricultural Water Management*, *249*, 106793. https://doi.org/10.1016/J.AGWAT.2021.106793

Chapter 4. Quantifying productive vs. unproductive water use in a pecan orchard under flood irrigation and different soil textures

4.1 Introduction

Surface water is a limited resource in arid and semiarid regions. For that reason, irrigated crops in drylands use groundwater to supplement or in some cases supply most crops' water needs. However, groundwater can be a non-renewable resource at a human time-scale. Hence water availability and the finite nature of most groundwater reservoirs becomes one of the most pressing issues for sustainable food production systems in drylands. Furthermore, with the advent of rising temperature trends from global warming and the continuously shrinking and more uncertain water supplies, agricultural production in semi-arid regions is becoming more vulnerable to high temperatures and limited surface water supplies. Consequently, improving irrigation management and planning is essential for agriculture's efficient water use and its continued viability (Nazari et al., 20018). However, despite dwindling water supplies and the looming threat of more frequent and intense droughts, low water-use-efficient irrigation (e.g., furrow) continues to be the most widely used method for water delivery into agricultural parcels (Sketch et al., 2019).

As climate change adds pressure to agricultural production and socioeconomic activities world wide (Jin et al., 2018), upward trends in global water scarcity pose an immediate risk to food production systems of drylands (Mekonnen & Hoekstra, 2016). Considering that agriculture consumes around 70 % of the freshwater globally (AQUASTAT-FAO, 2021), and that the slow pace in the implementation of technological innovations promoting water conservation in agriculture maintains a large proportion of irrigated drylands with irrigation efficiencies of ~29 %

on average at a global scale (Jägermeyr et al., 2015), there is ample opportunity to improve water management efforts on a global scale. For example, irrigation efficiencies reported in the Rio Grande Valley of the US Southwest, range from 20 to 95 % in pecan orchards (Ahadi et al., 2013), their methodology is based on evapotranspiration estimates that count soil evaporation as part of the water demand by the crops. In this study, we explore a different definition of water efficiency based on the productive water use of the crops as the transpiration ratio relative to the total water delivered in the plot.

In the Rio Grande Valley of southern New Mexico and west Texas, pecan producers use surface water and groundwater to satisfy the water demand of their crops. However, in the last 20 years, surface water in the river has experienced reduced flows (Mokari et al., 2022); Under this scenario, farmers need to improve their irrigation practices to maintain their yields and profits despite growing uncertainties in surface water availability. Confronting this situation requires managing water more efficiently. For this reason, identifying the conditions leading to and the periods when productive and unproductive water occurs, will decrease the vulnerability of crops to limited water availability. In rows of crops, the unproductive water (evaporation) occurs early in the season due to the low vegetation cover (Kang et al., 2003), particularly in between tree lines in orchards (Phogat et al., 2016). Knowing the water demand of the crops during the agricultural cycle can help adjust irrigation amounts and timing and increase water use efficiency. Also, knowing the spatial distribution of tree water use due to canopy cover, soil texture and albedo, and how that affects direct soil evaporation of irrigated water can help in better planning and distribution of resources (Kerridge et al., 2013). However, systematic irrigation at the plot scale assumes uniform irrigation distribution without considering the tree development differences and

soil texture variability and its effects on crop water demand (Jiménez et al., 2022). Various techniques are available to quantify crop water demands and usage with high accuracy but with limitations on spatial representation. For example, sap flow provides a direct measurement of tree water use that is punctual in nature and its generalizability depends on the homogeneity of the orchard; spatial changes in soil properties, tree development and water irrigation conditions would limit their representativeness. Eddy Covariance, and lysimeters are two of the most accurate methods to quantify crop water use, but their highly technical operation, maintenance, and cost render them impractical for adoption by most farmers (Nassar et al., 2020; Liu et al., 2012; Sánchez et al., 2019; Fang et al., 2020). In the last decade, remote sensing has been a helpful tool for monitoring croplands with high and moderate spatial and temporal resolutions (10-30 m and <16 days of revisiting time) (Drusch et al., 2012; Roy et al., 2014). Currently, satellite images can be used to monitor the agricultural dynamics both at the plot and regional scale in near real-time (i.e. every other day). These non-invasive techniques for monitoring the biophysical and biochemical variables of the crops (Dimitrov et al., 2019) are becoming more ubiquitous and accessible through a series of application programing interfaces in mobile devices (Melton et al., 2021; Wen et al., 2022). These tools can be used to characterize vegetation activity, stress, soil health and moisture and evapotranspiration fluxes at low cost using widely available public datasets and algorithms that have been extensively validated (Folhes et al., 2009).

Among the various remote sensing datasets publicly available, multispectral imagery from Sentinel-2 and Landsat missions can be used to provide indirect measurements of vegetation health through vegetation indices (VI). VIs are useful for monitoring the seasonal development of crops with high spatial and temporal resolution using empirical relationship between their values and

various plant traits (Bush & Neale, 1987; Neale et al., 1989). For example, Campos et al., (2010) documented the calculation of the basal crop coefficient (K_{cb}) using the Normalized Difference Vegetation Index (*NDVI*), through a linear relationship between *NDVI* and K_{cb}. Other studies verified the strong relationship between various forms of vegetation indices and K_{cb} (Sánchez et al., 2012; Pôças et al., 2020), even under non-optimal vegetation conditions (Hunsaker et al., 2007). VIs can also be used to estimate and monitor changes in canopy cover (*CC*) and crop growth to parameterize and calibrate hydrological models (Tenreiro et al., 2021). This is because VIs can closely track the changes in phenology associated with agronomic management on agricultural lands (Nagler et al., 2009), and because they are also associated with the dynamics of evapotranspiration (Nagler et al., 2005). In this work we use the *"Partitioning of Evapotranspiration through Vegetation Indices"* (*PETVI*) approach to investigate the spatial and temporal dynamics of water use by a flood irrigated pecan orchard with significant changes in soil texture. Hence, the study has two main objectives: the first is to analyze the dynamics of productive and unproductive water use of an annual crop (i.e. pecan orchard) in an arid region facing uncertain water availability for irrigation; the second objective is to evaluate the effects of differences in soil texture and tree development on the productive and unproductive water of a pecan orchard with flood irrigation (i.e. homogeneous water deliveries).

4.2 Materials and Methods

4.2.1 Study site

The study site is located in Tornillo, Texas, ~36 miles southeast from El Paso City (Figure 4.1). The site is a mature pecan orchard, with an area of 25.4 ha and a planting density of ~64 trees ha^{-1}. The experimental site is close to the Rio Grande River (~900 m) and has a shallow water table of ~ 2.10 m depth. The climate in the area is arid, with an average annual rainfall of 203-250 mm (Assadian et al., 1999; Mokari et al., 2021). Water is delivered to the orchard by flood irrigation during the agricultural cycle. In the year 2018, we recorded 11 irrigation events of ~127 mm each. The irrigation was systematically performed in time intervals of about ~3 to 4 weeks. The first irrigation is applied to leach salts from the soil profile that had accumulated from the previous cycle. Depending on the availability of surface water from the local irrigation district, the orchard can receive surface water from the canals in the area, or in the event of surface water unavailability, groundwater is pumped from the deep aquifer (>21 m deep) to fully supply or complement the crop water needs. When groundwater is used, it comes from two wells that withdraw water from the deep aquifer (Sheng et al., 2001). A peculiarity of the study site is the existence of two distinct soil textured regions that are spatially visible in the field and from aerial imagery. One of the soil textures is composed of soils with high contents of clays (hereafter referred to as Pecan Fine (*PF*), where pecan trees show precarious growth; the other soil texture is composed of coarser soil particles (hereafter referred to as Pecan Coarse (*PC*)) where the trees have grown healthy (Ortiz & Jin, 2021). We have obtained LiDAR cloud point data from the USGS in the area to calculate the canopy height model (*CHM*) and evaluate the effect of soil textures in the areas within the orchard where the trees show differential growth. The LiDAR point clouds were generated with an

airborne laser scanning (*ALS*) (Davison et al., 2020). The acquired *ALS* LiDAR point clouds (*LAZ*) were classified according to metadata, and used to evaluate the tree's growth. More details on the LiDAR data processing are provided in the data section below.

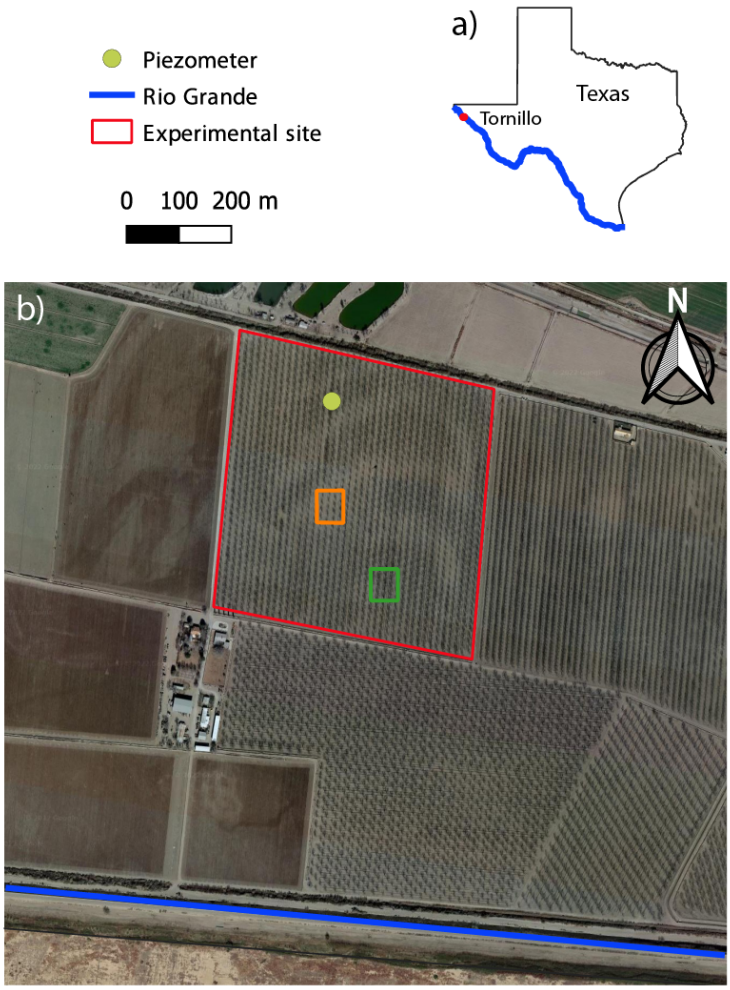

Figure 4.1 General location of the experimental site; a) Texas State highlighting the Rio Grande (blue line) and the experimental site (red dot); b) experimental plot (red square) and location of a piezometer (yellow dot) and two sample areas representative of fine soil textures (PF; orange square) and coarse soil textures (PC; green square). The blue line shows the location of the Rio Grande River 900 m south of the center of the orchard.

4.2.2 Data

4.2.3 Remote sensing data

The free online platform Google Earth Engine (*GEE*) has wide pre-processing images and is ready to use efficiently. Their catalogs contain a public database and various satellite images, and products with environmental variables. Landsat and Sentinel images are the most used (Gorelick et al., 2017). The *NDVI* 10 m spatial resolution, five days temporal resolution from *S-2*, and actual evapotranspiration *(ET*) come from *METRIC* algorithms using Landsat images 30 m spatial resolution and 16 days temporal resolution. Using these satellite products, we calculated transpiration (T_r) and *ET*.

4.2.4 METRIC data:

We downloaded ET_a images from https://eeflux-level1.appspot.com from January 2018 to March 2019. The quality control was made manually by image to avoid spurious data. Afterward, the images were uploaded to the *GEE*, each ET_a image with its metadata through the *GEEassets*. Subsequently, we made the ET_a images collection. Using the loaded shapefile in *GEEassets*, once we have ready the image collection with instantaneous ET_a. However, we need to get the daily ET_a values. Nevertheless, interpolating the ET_a data is impossible because ET_a depends on meteorological conditions. We need to get the crop coefficient (K_c) using the following relationship $K_c=ET_a/ET_0$ (Allen et al., 2007).

4.2.5 Sentinel-2 (S-2) images

We used *S-2* images to calculate the *NDVI* for each image available during the study period. We loaded the shape file with the geometric characteristics of the interest area; after that, we made a filter date from January 1, 2018, to March 31, 2019. We processed all available images on *GEE*. Later, we generated the *NDVI* time series. Afterward, we selected good data through the elimination of spurious data. Once we have the clean data, we calculate the vegetation fraction (V_f) using a linear model (Montandon & Small, 2008; Qi et al., 2000) and the basal crop coefficient (K_{cb}).

4.2.6 Reference evapotranspiration ET_0 from (gridMET).

The gridMET dataset is a reanalysis product where a model fed with ground-based and remotely sensed data, outputs gridded values of meteorological variables for the continental United States (CONUS). The dataset is produced and updated by the University of Idaho and is available in GEE (Abatzoglou, 2013). The variable we used for this work was reference evapotranspiration (ET_0) calculated with the Penman-Monteith equation; the time series data we used during 2018 was a daily scale. gridMET is reported in the literature as a reliable source for estimating reference evapotranspiration (Allen et al., 2015; Niyogi et al., 2020).

4.2.7 Lidar cloud points

We obtained the lidar data for the study site through the Open topography data gateway; the id survey was USGS LPC TX RioGrand FTWhit 2014 LAS 2016. After downloading the data, we decompressed and processed it to cover only the orchard and to classify each point as vegetation or bare ground using the free *LAStool* program (https://rapidlasso.com/lastools/). Class statistics

values contained in the metadata were used in the classification process through visualization using *lasview*. Once a first classification has been performed, class types are confirmed, and overlapping data points are removed to have a clearer image. Using these classified datasets we created both a digital surface model (*DSM*) and a digital terrain model (*DTM*), and used them both to generate a canopy height model (*CHM*) by substracting the *DTM* from the *DSM* (Mielcarek et al., 2018).

4.3 Methods

The crop coefficient is composed of two elements; an evaporation coefficient (K_e) and a basal crop coefficient (K_{cb}). In orchards, trees are planted in successive rows with bare ground interspaces at a regular distance, and depending on tree type, density and age of the orchard, the fraction of vegetation cover even at maximum canopy development does not completely cover the ground. Therefore, K_e can maintain a significant contribution to the Kc during the growing cycle. Usually, K_e has higher values at the beginning of the crop cycle, especially if the soil is wetted by irrigation or rain. However, it decreases gradually as the soil dries or is covered by vegetation. In any case, for this type of crop, foliage does not entirely cover the ground in between tree rows. K_{cb} values of orchards are low at the beginning of the season when trees are devoid of foliage, but once the growing season starts and trees begin the process of budding K_{cb} values start increasing (Figure 4.2). K_{cb} continues to increase with crop development reaching its maximum value when the crop reaches its full development. In the field, K_c is usually estimated by using a lysimeter, high-precision equipment, or by relating crop heights and meteorological variables (Sánchez et al., 2019; Fang et al., 2020). However, these measurements are frequently not available or recorded in the field, but it is possible to estimate them using the widely known relationship of K_c with the ET_a/ET_0 ratio. In this way, if we have punctual values in time, we can linearly interpolate to

construct the K_c curve. In the same way, the calculation of K_{cb} represents the proportion of the vegetation. For this reason, K_{cb} can be rescaled from vegetation indices due to its close relationship with the phenological development of the crop. Based on this fact, and if we have the punctual values in time, it is possible to make a linear interpolation to construct the K_{cb} curve for a particular agricultural cycle.

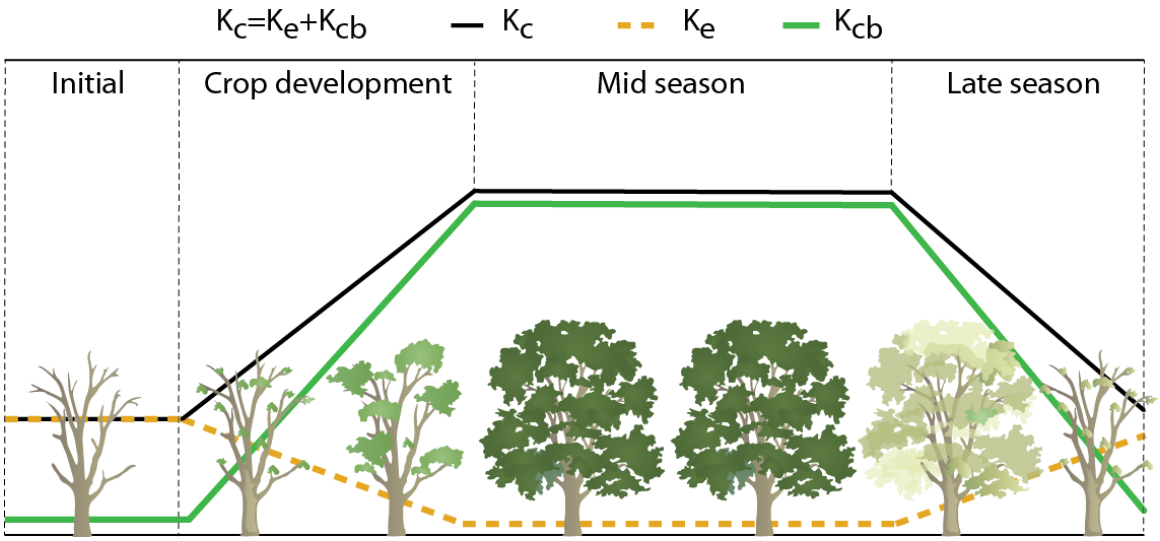

Figure 4.2 General shape of the crop coefficient (K_c) in a pecan orchard represented by a black line; the orange dashed line shows the hypothetical trajectory of the evaporation coefficient (K_e), and the green line characterizes the basal crop coefficient (K_{cb}). The vertical dashed lines delimit the main crop growth stages.

4.3.1 Vegetation fraction (*Fv*)

Here we used the fraction of vegetation through normalized difference vegetation index (*NDVI*) to adjust the transpiration values the images used to make the F_v calculation came from S-2. The F_v is easily obtained from remote sensing. F_v was computing using NDVI values following linear relationship using equation 1.

$$F_v = \frac{NDVI - NDVI_{min}}{NDVI_{max} - NDVI_{min}}$$ Eq. (1),

where NDVI corresponds to the index value, NDVImin corresponds to the absolute minimum values of NDVI that correspond to soil values, NDVImax is the absolute maximum values that usually correspond to the maximum vegetation development. The values we used to calculate were NDVI min 0.10 and NDVI max 0.75. the minimum and maximum values were obtained from the study site.

4.3.2 Transpiration using Basal crop Coefficient (K_{cb})

We used a method that combines energy balance-based ET_a from remotely sensed data estimate the basal crop coefficient (K_{cb}), using a vegetation index (VI) based on the empirical relationship between VI and crop development during the growing cycle and their relationship with plant transpiration (Allen et al., 2011; Glenn et al., 2008). This method uses satellite products to monitor vegetation growth dynamics and water use. A detailed graphical representation of the process is shown in Figure 3, where the inputs to obtain the vegetation index are denoted using the images captured by the *S-2* satellite (yellow boxes) with a temporal resolution of 5 days and spatial resolution of 10 m. The images were processed entirely in the GEE platform. The calculation was made through the normalized difference function between two spectral bands, band 8 (near-infrared) and band 4 (red). Before the analysis, the shapefile with geographical characteristics of the interest area was uploaded to GEE's online platform using the assets tool to delimit the specific calculation area for the study site. For the calculation of NDVI, we used all available images within the study period. daily K_{cb} values were calculated from the NDVI time series by rescaling the NDVI values to the maximum possible K_c reported for that particular crop using the equation for the vegetation cover fraction following (Schüttemeyer et al., (2007); Allen et al., (1998); Hunsaker

et al., (2005)). That is, the vegetation fraction from NDVI was multiplied by the maximum value of K_c as follows:

$$K_{cb} = 1.05 * \frac{NDVI - NDVI_{min}}{NDVI_{max} - NDVI_{min}} \quad \text{Eq. (2),}$$

the 1.05 corresponds to the maximum value of the pecans basal crop coefficient (K_{cb}) reported by Allen et al., (1998). Before interpolating the daily K_{cb} values, visual analysis was carried out on the time series of the instantaneous K_{cb} values. Quality control was carried out manually, removing the spurious data. Subsequently, linearly interpolates the daily K_{cb} values, creating a time series at a daily scale.

The transpiration was calculated as follows:

$$T_r = ET_0 * K_{cb} * F_c = ET_0 * 1.05 * \left[\frac{NDVI - NDVI_{min}}{NDVI_{max} - NDVI_{min}}\right]^2 \quad \text{Eq. (3),}$$

4.3.3 Evapotranspiration from METRIC.

In the diagram of Figure 3, the Evapotranspiration (ET_a) images in [mm day^{-1}] are represented in yellow color. These images are available on the Earth Engine Evapotranspiration Flux (EEFLux) website https://eeflux-level1.appspot.com/, (Allen et al., 2007; Allen et al., 2015; Allen et al., 2011; Wan et al., 2021). For our study period, the *ET* images from Landsat 7 and 8 missions corresponding to path 034 and row 041 with a spatial resolution of 30 m and temporal resolution of 16 days were used. The images were inspected manually to select those free of cloudiness on the study parcel. The images were uploaded to the *GEE* platform by creating a collection of images with the assets tool; the selected images were added with metadata. Once the

collection of images is created, a scene cut is made based on the shapefile of the study area. Given the characteristics of the study. It is necessary to have daily *ET* values. However, linear interpolation of *ET* images is impossible due to daily changes in local weather conditions. The way to extrapolate these data is through interpolating crop coefficient values (K_c), (Allen et al., 2007; de Oliveira Costa et al., 2020; Reyes-González et al., 2019). K_c was calculated with the relationship between the daily *ET* for each pixel of the image, and the reference Evapotranspiration (ET_0) was calculated from local weather data. Equation 4.

$$K_c = \frac{ET_a}{ET_0} \quad \text{Eq. (4),}$$

Where K_c is the crop coefficient, ET_a is the instantaneous evapotranspiration, and ET_0 is the reference evapotranspiration. Once the instantaneous K_c values were obtained, linear interpolation was performed to obtain a daily scale time series of K_c.

The maximum basal crop coefficient for pecan is 1.05 (Allen et al., 1998). Using equation 5, we obtained the K_c instantaneous values. However, using this approach, some dates with low ET_a can yield K_c values lower than the expected K_c according to the phenological stage of the crop. Therefore, ET_a images obtained from the energy balance algorithm (i.e. METRIC) need to be calibrated by adjusting the Kc using the tabulated values and observations of the crop in the experimental site based on its phenological stage.

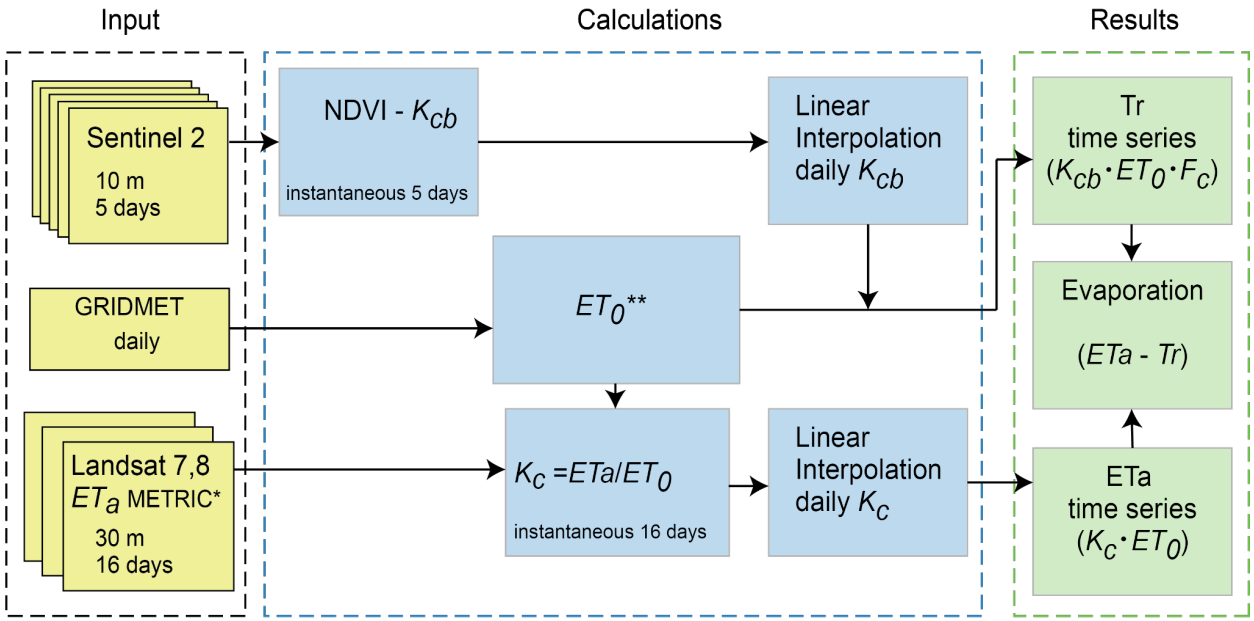

**Allen et al., 2007; ** Penman-Monteith, Allen et al., 1998.*

Figure 4.3 Diagram to estimate the variables needed in the PETVI method. This workflow diagram shows the input variables from left to right with yellow squares. Here are the required S-2 images, meteorological data, and ET_a images from Landsat using METRIC algorithms. In the center of the flow diagram are the basic calculations and procedures. Finally, in the green boxes are represented the results at the daily scale of T_r, ET_a, and last but not less significantly, the evaporation as residual from the subtraction of the T_r of ET_a.

4.3.4 Partitioning Evapotranspiration

To partitioning the (transpiration) and unproductive (evaporation) evapotranspiration in a cropland can support decision making for improved water management practices. Once the daily values of K_c, $K_{cb,}$ and ET_0 were obtained, the multiplication between ET_0 and K_{cb} was carried out as shown in Figure 4.3 in the green box. In this way, it is possible to obtain the transpiration of the vegetation (T_r). The estimate T_r is based on the $K_{c's}$ transpiration portion of the vegetation. In the same way, to calculate the daily ET_a, the procedure shown in Fgure 4.3 is followed in the green box where the multiplication between ET_0 and K_c is shown. Both procedures are based on the

methodologies proposed by (Hargreaves & Samani, 1991; Allen et al., 1998). Thus, with the daily time series of ET_a and T_r. Evaporation was determined as the residual between ET and T_r. That is the fraction of productive water use (T_r) and unproductive water evaporation from the soil (E_v) during the growing season for the wheat crop.

4.4 Results

4.4.1 Evapotranspiration dynamics during the agricultural cycle

Studying the dynamics of evapotranspiration in croplands of semiarid regions is helpful because it permits us to understand how the water moves in agricultural systems. In this work, we show the dynamics of actual ET_a and its partition into evaporation (E_v; unproductive water) and transpiration (Trwith a time series beginning on January 1, 2018, and ending in March 31, 2019 to observe the behavior of the pre-budding irrigation (Figure 4.4). The water consumed through evapotranspiration (ET_a) in the orchard during the growing season was 1,297 mm. The majority of the ET_a in the early season of the agricultural cycle, was unproductive water (Evaporation [(E_v]), directly evaporated from the soil, at a time when the pecan trees are inactive and water is delivered primarily to leach the salts accumulated in the soil profile during the previous growing cycle. Transpiration (T_r) begins in April with the bud breaking of the Pecan trees, reaching its maximum value in June, when the crop attained its highest leaf development with a T_r rate of 7.8 mm day^{-1}, and the E_v decreased its magnitude to close to zero. In September, E_v values appear because vegetation activity decreases and trees start senescing. E_v continues beyond the end of the growing cycle when moisture becomes available and atmospheric demand for evapotranspiration continues. Figure 4.4.a,b and c, display the time series of the average and standard variation of ET_a, E_v and T_r for the whole pecan orchard (WP) and for two sample areas representative of coarse (PC) and

fine (PF) soil textures respectively. Variability in T_r for the WP is higher than that of PC and PF reflecting the contribution of both soil textures on tree water use. Generally and throughout the growing season, T_r variability in PC remains low, reflecting the homogeneous signal of the vegetation indices from the healthy trees, while T_r from PF show larger variability. Also, trees from the PF area are significantly smaller than those in the PC area, yielding lower T_r values than the trees in the PC all along the growing season. The cumulative E_v averaged over the entire orchard (WP) was 758 mm, while the cumulative average of T_r was 541 mm. The cumulative averaged E_v on PC was smaller than that of WP (661 mm) and the cumulative averaged T_r was higher than in WP (~640 mm). 3g). The smaller cumulative water fluxes occurred in the PF area, where E_v totaled 920 mm, and T_r accounted for only 377 mm, which compared to T_r from PC it represents ~58 % of its total.

For the purpose of this analysis, the surface water balance (input-output) of the orchard begins at 0 mm before the first irrigation in early March and ends in mid-November where it ends with a surplus of 309 mm of water content stored in the soil profile after the last irrigation event. During the last stretch of the season in October, significant rainfall events (> 66 mm) contributed to the surplus of water in the orchard. This surplus starts to recede past November and into the new year until a new irrigation event in March of 2019 starts a new cycle. This analysis shows that the orchard ends its cycle with more water than needed for the season. Figure 3.i shows the proportion of irrigation water and rainfall as water inputs to the orchard, with 88 % and 12 % coming from irrigation and rainfall, respectively. Figure 4.4 j) are the water output represented in percentage of the total water entering to the plot by the condition of the average fluxes of the plot is 35 % corresponds to transpiration (productive water use), 49 % corresponds to unproductive water use,

and 16 % corresponds to change in the storage. Figure 4.4 k) on the trees within the pecan-coarse area, the Tr increase relative to the plot average is 43 % Ev 41 %, and the change in the storage continues to show the same value of 16 %. Finally, panel l) shows the water output on the pecan-fine area; the Tr was 24 %, Ev was 59 %, and 16 % of the change in storage.

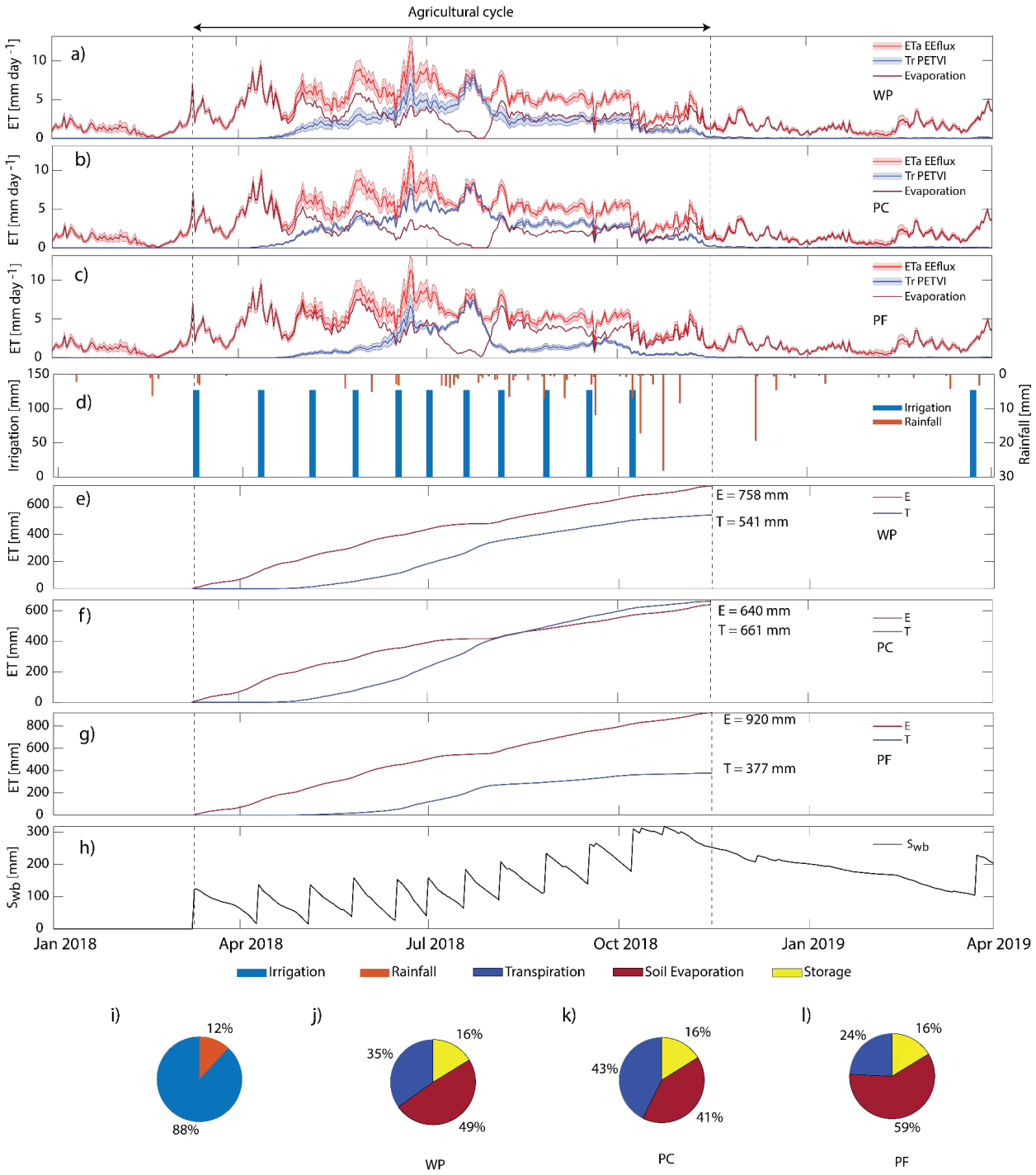

Figure 4.4 a), b), and c) time series of the mean evapotranspiration (ET_a), transpiration (T_r) and soil evaporation (E_v) for the orchard (WP), the coarse grained soil area (PC) and the fine grained soil area (PF) respectively; shaded red and blue lines show the variability of the ET_a and T_r respectively with +/- one standard deviation; d) shows the water inputs to the orchard from irrigation events (blue bars) and rainfall events (red bars); e, f, g) show the cumulative E_v (red)

and cumulative T_r (blue) for WP, PC and PF respectively; h) time series of the surface water balance (SWC); i) proportion of water inputs as percentage of irrigation (blue) and rainfall (red); and j, k, l) proportion of water output components (T_r in blue, Storage in yellow and E_v in red) in percentage for the WP, PC and PF respectively.

4.4.2 Evolution of the water balance components in the orchard during the growing season.

Assessment of the times and relative magnitudes of productive (T_r) and unproductive (E_v) water use in agriculture of semi-arid environments can provide insights into the evolution of the crop water demand. In this study, we tracked the behavior of both fluxes after each irrigation event in a pecan orchard under flood irrigation. Figure 4.5 shows the water balance components in the study site for the 11 periods in between irrigation events. The amount of water delivered to the orchard in all irrigation events was constant, with a total of 127 mm per event, while rainfall contributed a total of 153 mm during the entire growing cycle, and was irregularly distributed in time, although the majority came in October at the end of the cycle. In total water input was 1,550 mm. Figure 4.5.b, c and d, show how the orchard used this water. After the first irrigation event to leach salts below the root system in early March, the majority of the water was consumed as E_v and about ~10% was stored in the soil column. From the beginning to the end of the Tree's activities, the cumulative T_r for the entire orchard averaged 541mm. During the same period, cumulative T_r in the PC and PF areas averaged 661 mm and 377 mm respectively, while cumulative E_v values from the average plot were 758 mm, for the PC area was 640 mm, and the E_v values from the PF site were 920 mm. The change in moisture storage (**Δ**S) in the soils of the

whole orchard averaged 251 mm, while the average for the PC area was 149 mm, and for the PF area was 253 mm.

Except for the first irrigation event, T_r has a rising trend until the 7th irrigation in mid-July; after that, T_r reverses the trend, constantly decreasing until the end of the season in mid-November. On the other hand, E_v behavior is opposite to T_r, showing a decreasing trend at the beginning of the season until the seventh irrigation event, and then reverting to an increasing trend until the end of the season. After the first irrigation, **Δ**S shows a gain in water content in the second irrigate the soil water content appear seem to contribute to ET water fluxes. The third irrigation again has a positive **Δ**S, in fourth irrigation the **Δ**S shoes the negative values reveal the soil water contribution to the ET fluxes. from the fifth irrigation to the end of the agricultural cycle the **Δ**S shows positive values that is mean the soil profile gain water with great **Δ**S in the eleventh irrigation due last irrigation and rainfall contribution.

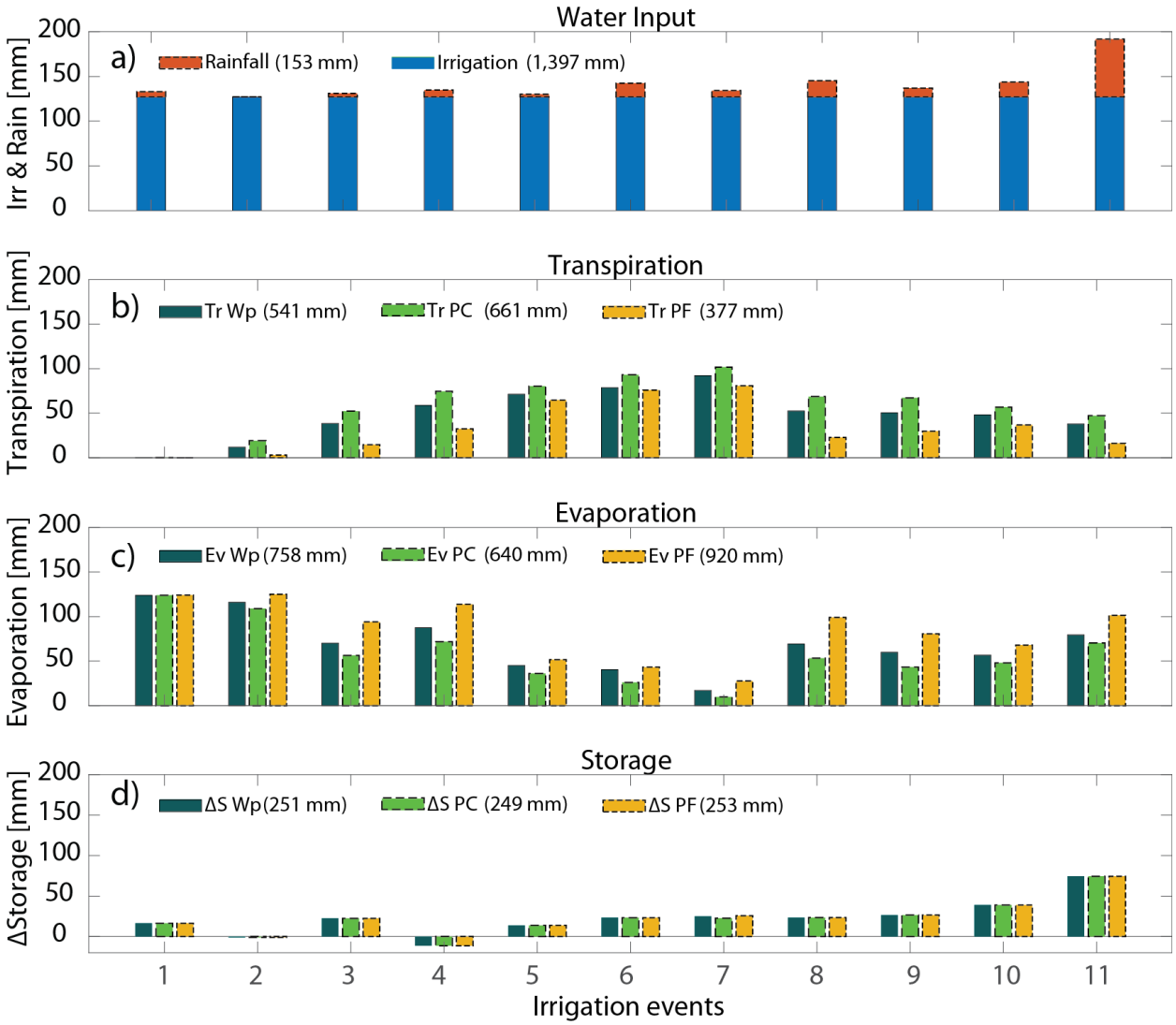

Figure 4.5 Water balance components in between irrigation events; a) water inputs from irrigation (blue bars), and rainfall (red bars); b), c) and d) show the averages of transpiration (T_r) evaporation (Ev) and (ΔS) respectively, for the whole orchard (WP; dark green), the Pecan Coarse area (PC; light green), and the Pecan Fine area (PF; yellow).

4.4.3 Analysis of canopy height and soil texture distribution.

The spatial distribution of canopy height (*CH*) can be used to show the effect of different soil textures on tree growth as a proxy for expected vegetation activity and water use. Figure 4.6 a) shows the spatial distribution of CH for the trees in the orchard. Clear contrasts between *PF* and *PC CH* are visible in that image. Trees on *PF* areas are consistently lower than the trees within the PC areas; on average, the height at the middle of the canopy was 3.5 m in the *PF* areas, while on the PC areas was 5 m. The development of vegetation had effects on the rate of transpiration. As described above, vegetative growth is attenuated mainly where the *PF* area is located. The trees show a much-limited canopy development in this area compared to *PC* areas. To confirm this assumption, we analyzed the *CH* profiles across the *PF* and *PC* areas (Figure 4.6 b). We observe the variability of larger *CH* values reveals a good tree development (~ 9 m). In some distances, the *CH* values decrease until ~3 m or less, indicating a deficient tree development. This behavior is dominated by the *PC* and *PF* areas. In this finding, we motivate to analyze *Tr* and *Ev* for both texture locations to evaluate how tree growth changes affect *ET* fluxes (Section 3.3).

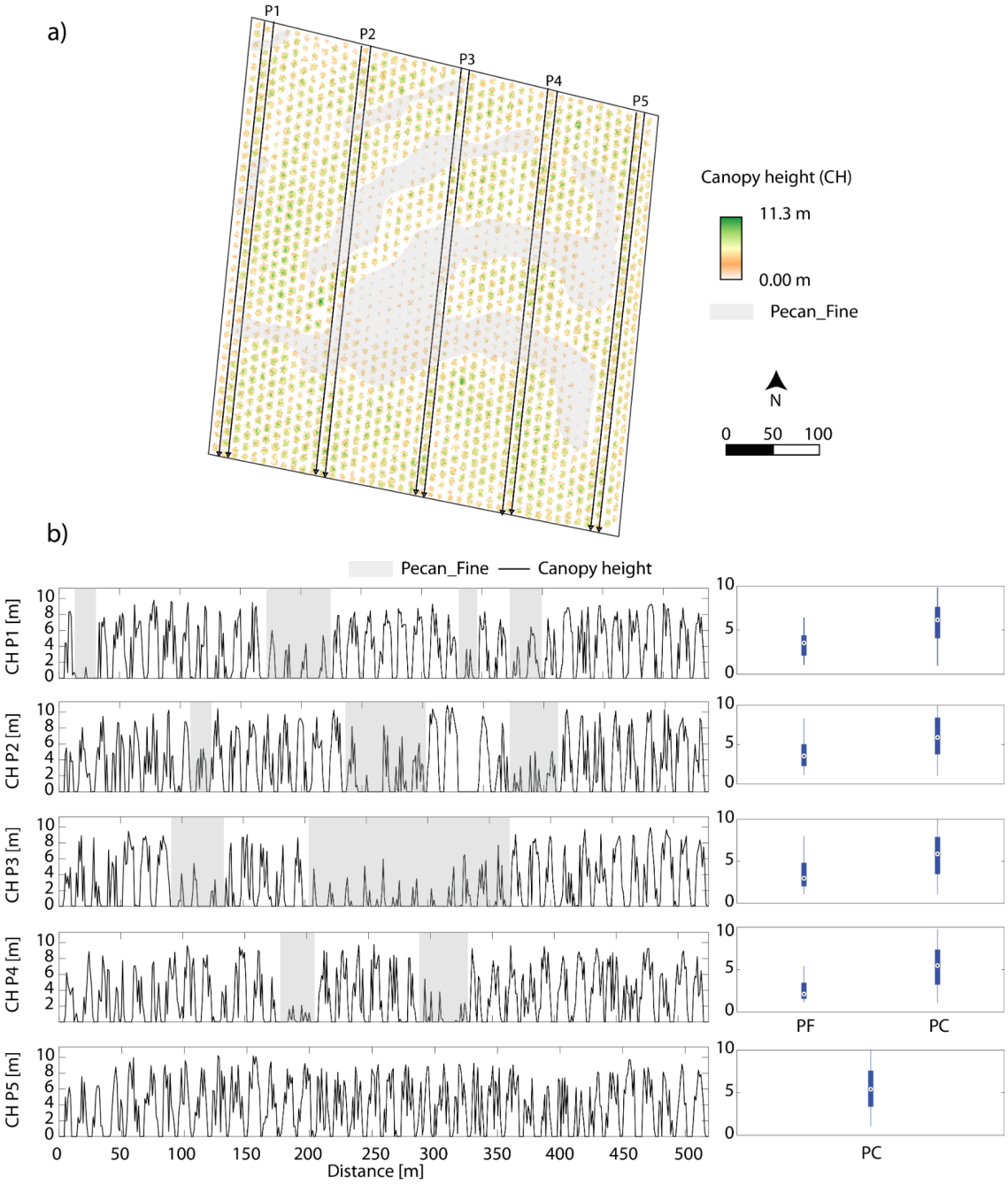

Figure 4.6 Spatial distribution of LiDAR-derived canopy height (CH) for each tree in the Pecan Orchard; black arrows depict the transects of the profiles showing the variability in CH from P1 to P5 in (b); areas of fine texture soil are shown in gray color; CH varies from 0 (white) to 11.3 m (green); b) Canopy height distribution across each profile (P1 to P5) increasing in distance from north to south; c) box plots showing the distribution of CH values for each profile and separated by soil texture where PF is fine texture soil, and PC is coarse texture soil.

4.4.4 Effect of soil texture on transpiration dynamics during the agricultural cycle.

The presence of high clay content in soils of agricultural lands can create anoxic conditions in the soil profile after large irrigation events by restricting the downward movement of water (Keiluweit et al., 2018), thereby favoring the accumulation and concentration of solutes and salts and restricting root development, vegetation activity including photosynthesis and transpiration and consequently tree growth. In our study site, this is evidenced by significantly lower height and size of the canopies sitting on fine-grained soils with high clay contents. Our study site has two main soil textures PC (sandy soil) and PF (clayey soil), and their spatial distribution is visible through aerial images. The fine texture soil is located in the middle of the parcel in an irregular shape. In these areas, Pecan trees show uneven development with shorter and irregular canopies relative to those of the average trees located on coarse textured soil. Figure 4.7 shows both the spatial patterns (contrasts) between T_r in areas with fine grained and coarse grained soils and the distribution of their T_r values with probability distribution functions (PDF) for the entire orchard in between irrigation events during the 2018 growing season. After the first irrigation on March 10, there was no T_r anywhere on the orchard. An incipient amount of T_r was detected after the second irrigation event (1.5 mm mode for PF and 18 mm mode for PC), and the separation in the distribution of T_r values between the different soil texture areas continued as T_r increased together with the phenological development of the pecan trees. After the fourth irrigation event, the difference in modes of the T_r distribution between the areas with coarse and fine grained soils grew to >40 mm. Then after the fifth irrigation event on June 16, the distribution of T_r values for PF and PC soil textures got closer, with PF showing a 60 mm mode and PC a 78 mm mode. Maximum T_r modes were reached during July and August, at the peak of the crop development, with T_r modes

of 70 mm for PF and 95 mm for PC on July 1th, and 90 mm for PF and 105 mm for PC in August. After that, T_r significantly decreased and with it the average separation of the two soil types distributions. In the last irrigation period the T_r mode was 20 mm for the PF and 55 mm for the PC. The distribution of Tr values for both soil types shows clearly the effect of soil texture and tree development on the productive and unproductive use of water for these orchards.

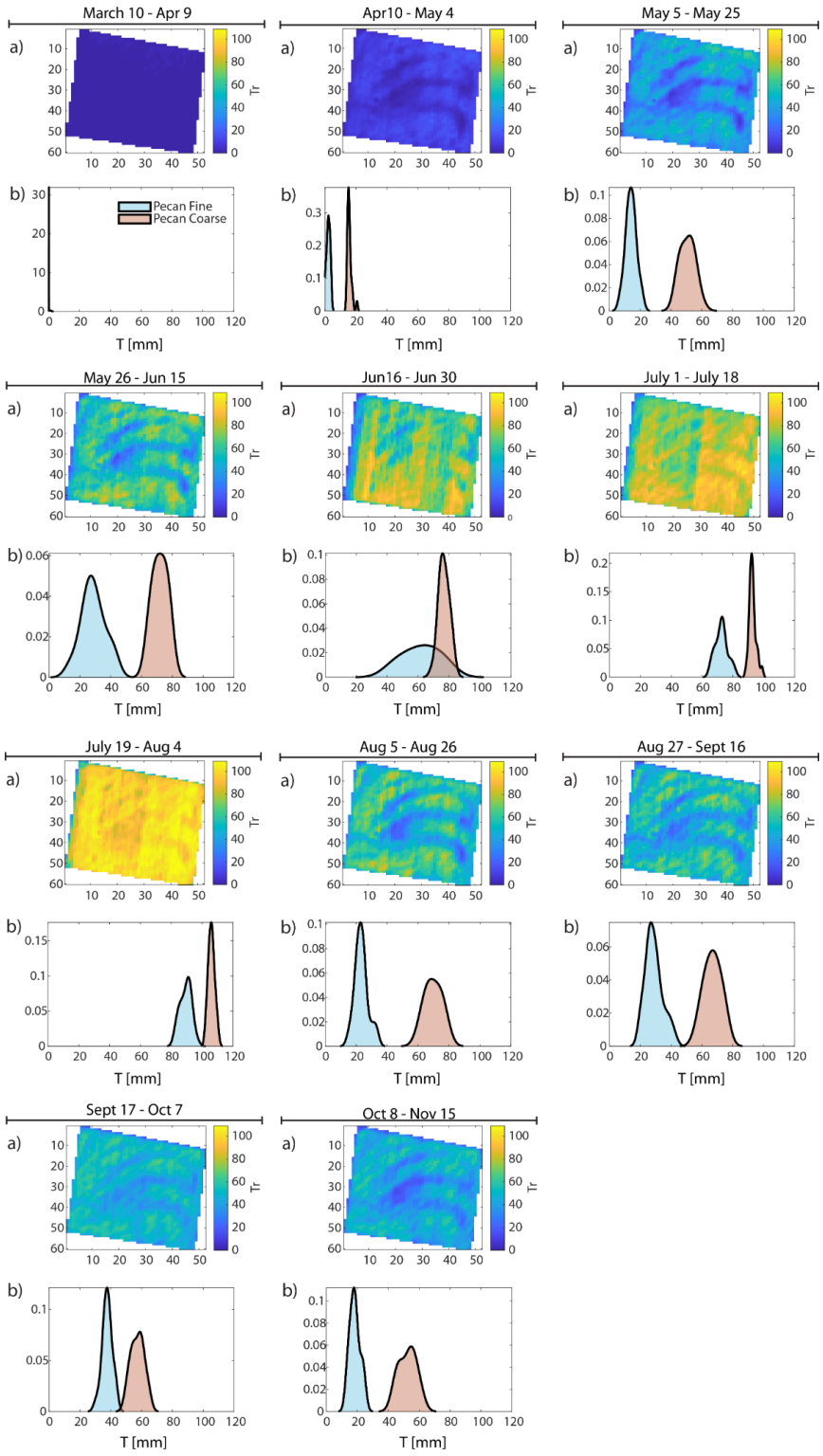

Figure 4.7 Transpiration (T_r) spatial patterns in the orchard for periods in between irrigation events and their probability density functions (PDF) for the coarse textured (PC; pink shaded), and fine textured (PF; blue shaded) soils.

4.4.5 Effect of soil texture on evaporation dynamics during the agricultural cycle.

Soil evaporation (Ev) in the two sampled areas, PC and PF, showed the opposite behavior to Tr. Figure 4.8 shows the spatial distribution of Ev and its PDF for each irrigation period in both areas. In our study site during the study period, the first irrigation was delivered on March 10; PC and PF areas show the same Ev distribution of values for that date with a mode of 45 mm; for subsequent irrigations, the Ev values continue to increase, with a separation in the distribution of Ev. Mode of 25 mm, this trend continues until the fourth irrigation on May 26. For the June and July irrigations, the Ev was significantly reduced with a separation of the Ev values based on the mode was 15 mm, with the trend of higher Ev in the PF area. After this period, the Ev values gradually increase, with the pattern of separation between both areas (PC and PF) consistent. At the end of the season, there were rain events followed by the last irrigation, given this condition for the irrigation of October 8, which shows greater evaporation. As we can see, the textures are a key factor in the crop's development with interference in Ev's flows.

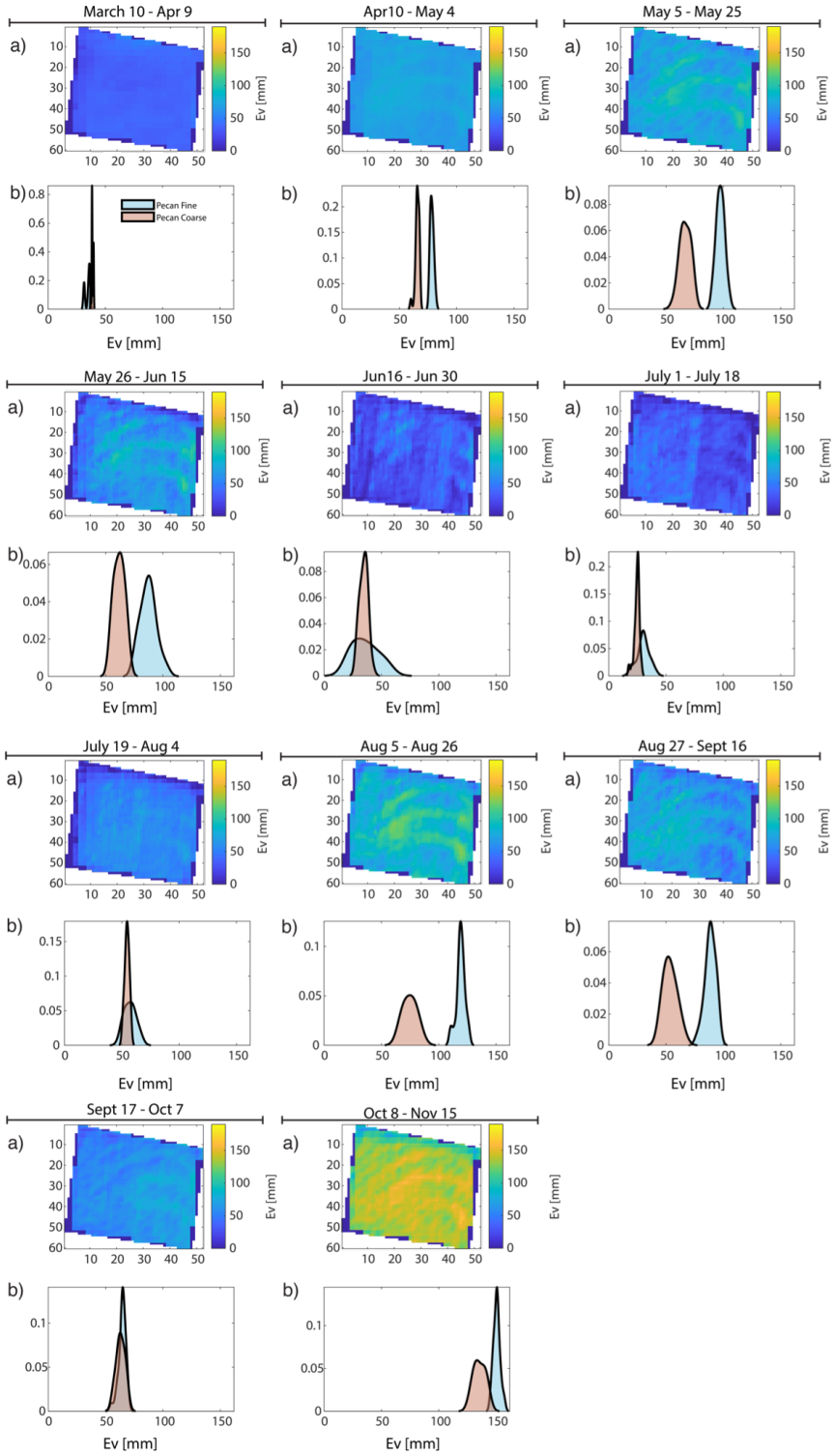

Figure 4.8 Evaporation (E_v) spatial pattern in the orchard for periods in between irrigation events and their probability density functions (PDF) for the coarse textured (PC; pink shaded), and fine textured (PF; blue shaded) soils.

4.5 Discussion

4.5.1 Dynamics of evapotranspiration during the agricultural cycle.

In agricultural production, consumptive water use is determined from evapotranspiration (ET_a), and which is commonly thought of as the equivalent of the crop's water footprint. This water footprint in crops of economic importance is generally supplemented by irrigation. In our study orchard, ET_a flows started in early March, after the first irrigation event and before bud break, as part of soil preparation to leach salts beyond the root zone (Jin et al., 2018; Palmate et al., 2022). Most of the water inputs into the orchard during the senescence period returns to the atmosphere as evaporation (E_v) and become unproductive water because the vegetation is inactive. The daily values of ET_a fluctuated from close to zero in the early season to maximum values of 10 mm day^{-1} during the season of maximum vegetation development; this occurred from July to August. From March 10 [first irrigation] to November 15, a total ET_a of 1,297 mm was calculated during the observation period. These values are comparable to recent findings by Mokari et al., (2022) in a pecan orchard in New Mexico, where ET_a was obtained using thermal imaging and reported a range of 1200 – 1300 mm of water. Other work conducted in the pecan producing region of New Mexico (Miyamoto, 1983) reported an total ET_a of 1,310 mm during the growing season, also similar to the water footprint found in our study site. Differences between the reported values and our findings can be attributed to the particularities of the study site because of soil textures and vegetation development and slight differences in weather conditions from the natural climatic variability in the area. The most salient feature of our analysis, is the finding that most of the unproductive water consumed in the orchard occurs at the beginning of the year, early in the

growing season and it represents 28 % of the annual amount of water delivered and 30 % of the total ET.

4.5.2 Productive and unproductive water use during different stages of the agricultural cycle.

The change in water use in a crop follows the development of different phenological stages, as mentioned in sections 3.1.1 and 4.1. As such, most of the unproductive water use occurs at the early stage and at the end of the agricultural cycle. Our findings are consistent with previous studies by Sammis et al., (2004) on flood irrigated pecan orchards, who reported that the highest contribution of E_v (unproductive water) to the ET occurs from January to March, just before the pecan trees reach 50 % of budbreak. Other authors refer that high rates of soil evaporation occur right after water is delivered by flood irrigation, and particularly when the crops are in their early stages of development and only partially covering the soil (Er-Raki et al., 2009; Ibraimo et al., 2016). The average E_v on the orchard in this study was 41% of the total ET_a, which is 6% higher than that reported by Er-Raki et al., (2014) in an olive orchard in Morocco under similar flood irrigation and climatic conditions. Typically, flood irrigation favors potential evaporation for a few days immediately after the water is delivered, which translates into high E_v rates from standing water or fully saturated shallow soils from irrigation or rainfall events. As shown in Figure 3.a) a peak in evaporation occurs after each irrigation event with higher E_v rates at the beginning of the agricultural cycle. However, when canopy cover increased, E_v continued but at a lower rate, reflecting the fact that evaporation rates of soils under canopies decrease relative to bare soil E_v due to decreases in energy loads from shade effects (Deb et al., 2011). Unproductive water can be seen at the end of the agricultural cycle when water from the last irrigation and from rainfall events

maintain high soil moisture conditions at a time trees start senescing. Although the productive water use period occurs from April to November, when the pecan trees have already gone through the process of resprouting, developing a full canopy and filled their nuts, the most productive water use stage occurs during mid-season, when K_{cb} had reached its maximum (Paço et al., 2006). Hence, greater transpiration (productive water) occurs in July-August. On the other hand, low transpiration rates occur at the beginning and the end of the agricultural cycle when K_{cb} starts to grow and once it starts decreasing respectively (Puig-Sirera et al., 2021).

4.5.3 Effect of soil texture on partitioning ET fluxes of a pecan orchard.

Ideal crop development depends on a variety of factors, but particularly on soil conditions. For example, vegetation growth (e.g. leaf area index) and evapotranspiration response is strongly associated with soil texture (el Maayar & Chen, 2006), where slight variations in soil properties can significantly alter the water use efficiency (WUE) of crops. For instance, Yu et al., (2021) reported that vegetation in medium textured soils display large differences in WUE compared to plants in fine textured soils. Our study site has two main soil textures (i.e., fine grained [PF] and coarse grained [PC]) that have largely influenced the development of the trees, affecting their canopy sizes and influencing the spatial variability of the *ET* partitioning in the orchard. In the PC areas, 41% of the water inputs corresponds to E_v, while in PF that number rises to 59% significatively altering the irrigation water use efficiency of the orchard. Those high E_v values (59 % of water inputs) occur in areas where most of the soil is directly exposed to the elements because the trees have small canopies. This is comparable to results from a study reported by Wang and Wang (2017), who found 52 % of water inputs as soil evaporation in an orchard with small trees. Similarly, Odi-Lara et al., (2016), found a high E_v rate after rainfall and irrigation events in areas

with low vegetation cover. Also, it is consistent with the report by Gong et al., (2007) that the E_v is dominant in areas with low leaf area index and low canopy development (Ritchie, 1972; Testi et al., 2004; Villalobos et al., 2000). Furthermore, if the exposed soils have high clay contents, such as in the PF areas in the study orchard, soil cracking during the desiccation of the shallow soil enhances further soil moisture evaporation from deeper in the profile (Whitmore & Whalley, 2009). Soil texture, as noted above, is an important factor that govern the water movement and availability of nutrients, both of which can decrease the capability of roots to take water and minerals and in the end affecting trees' growth (Clark et al., 2003). The PF patch in the middle of the study plot shows physical evidence of those characteristics already described: soil cracking, unhealthy and smaller than average trees with irregular canopy development. This is consistent with a work conducted by Khalil et al., (2020) who reported low vegetation development in clayey soils. When compared to PF E_v, PC E_v values are 18 % less than the E_v in the PF area.

In the studied orchard, soil evaporation will always occur to some extent due to planting arrangement and the bare soil between the tree rows (Agam et al., 2012), and soil textures, irrigation regime and plant canopy development (Kool et al., 2014). In general terms, evaporation occurs due to the bare soil exposed between tree lines and high soil water contents due to the flood irrigation. Because of the nature of flood irrigation, it is difficult to variably adjust irrigation amounts to reduce unproductive water use based on the spatial distribution of soil texture.

4.5.4 Implications of the information on the productive and unproductive use of water for sustainable management of an orchard with two water sources.

In this work, we found that unproductive water occurs during the early season of the crop cycle. In some places, with perennial crops, due to fertilization practices or poor quality water, irrigation from complementary water sources favors the soil salt concentration. This condition needs to be reduced to avoid significant decreases in crop yield for many sensible crops. To alleviate soil salinization, farmers apply irrigation to leach salts below the root zone to reduce soil salinization. Systematically, these watering events are placed during the dormant period (Miyamoto, 2006). This supports why the unproductive water occurs just at the beginning of the agricultural cycle. The soil salt phenomena have more effect in clay textures areas due to their low permeability, that increase with high soil compaction and low vegetation development due to the pass agricultural implements to do the agronomic practices (Miyamoto & Cruz, 1986). In some years, surface water is scarce, reflecting the low river flow (Sheng & Liu, 2015); when that occurs is a need to use the groundwater to leach salt. However, these practices increase groundwater's unsustainability because some water delivered in the plot is returned to the atmosphere as soil evaporation (unproductive water). Moreover, it can increase the problem because, in some areas, the groundwater has elevated salinity (Miyamoto, 2006). Other issues that faced the agricultural plots were the soil texture variability. We found a high evaporation rate in the PF textures area. Similar behavior was found by Li et al., (2022) in their work related to soil evaporation in different soil textures. This information can be used to improve irrigation schedules by identifying the optimal periods to do this practice and reduce the effect of unproductive water on the efficiency of water use, especially in semiarid environments. However, soil texture variabilities make it difficult

to spatially-modify water deliveries within orchards with flood irrigation systems where the irrigation water depth is delivered uniformly. From empirical knowledge, some farmers guess that the excess water delivered by flood irrigation could recharge the aquifer. However, that does not occur, especially in soil with fine particles that inhibit irrigation recharge (Scanlon et al., 2010). Knowledge of the areas where the unproductive water occurs can be used to differentially manage water deliveries if the plot is equipped with spot irrigation. When possible adequate operation of irrigation systems can help decrease the excess water that plants are not using and with it the reduction of E_v from the annual water footprint through the irrigation season.

4.6 Conclusion

In this work, we found that the soil texture influenced the variability of the productive and unproductive water in the orchard. We observed that a large portion of the unproductive water use occurs early in the season due to soil preparation for the following agricultural cycle. Applying the PETVI methodology to separate the ET fluxes using moderate spatial (30 m from Landsat and 10 m from S-2) and temporal (16 days from Landsat and 3-5 days from S-2) resolution allowed us to observe the spatiotemporal variability of the productive and unproductive water use in the orchard. Our data indicates supports the hypothesis that soil texture driven changes in ETa partitioning constrain water use by trees limiting or enhancing their growth and canopy development. In our findings, most of the unproductive water occurs in the irregular PF patches, while the most productive water use occurs in the PC areas. The cumulative unproductive water use is higher in the PF than in the PC in each irrigation period, mainly due to the low vegetation fraction within the PF area. Based on these findings, the best time to reduce the unproductive water use in the orchard is at the beginning of the agricultural cycle, pushing the first water deliveries closer to the

budbreak time. By modifying the calendarization of the first irrigations, the farmers could help reduce salt concentrations in the soil profile and reduce unproductive water in the early season.

4.7 References

Ahadi, R., Samani, Z., & Skaggs, R. (2013). Evaluating on-farm irrigation efficiency across the watershed: A case study of New Mexico's Lower Rio Grande Basin. *Agricultural Water Management*, *124*, 52–57. https://doi.org/10.1016/J.AGWAT.2013.03.010

Allen, R. G., Pereira, L. S., Howell, T. A., & Jensen, M. E. (2011). Evapotranspiration information reporting: I. Factors governing measurement accuracy. *Agricultural Water Management*, *98*(6), 899–920. https://doi.org/10.1016/J.AGWAT.2010.12.015

Allen, R. G., Tasumi, M., & Trezza, R. (2007). Satellite-Based Energy Balance for Mapping Evapotranspiration with Internalized Calibration "METRIC…-Model. *Irrigation and Drainage Engineering*, *133*(4), 380–394. https://doi.org/10.1061/ASCE0733-94372007133:4380

Assadian, N. W., Fenn, L. B., Flores-Ortiz, M. A., & Ali, A. S. (1999). Spatial variability of solutes in a pecan orchard surface-irrigated with untreated effluents in the upper Rio Grande River basin. *Agricultural Water Management*, *42*(2), 143–156. https://doi.org/10.1016/S0378-3774(99)00037-2

Campos, I., Neale, C. M. U., Calera, A., Balbontín, C., & González-Piqueras, J. (2010). Assessing satellite-based basal crop coefficients for irrigated grapes (Vitis vinifera L.). *Agricultural Water Management*, *98*(1), 45–54. https://doi.org/10.1016/J.AGWAT.2010.07.011

de Oliveira Costa, J., José, J. V., Wolff, W., de Oliveira, N. P. R., Oliveira, R. C., Ribeiro, N. L., Coelho, R. D., da Silva, T. J. A., Bonfim-Silva, E. M., & Schlichting, A. F. (2020). Spatial

variability quantification of maize water consumption based on Google EEflux tool. *Agricultural Water Management*, *232*, 106037. https://doi.org/10.1016/J.AGWAT.2020.106037

Deb, S. K., Shukla, M. K., & Mexal, J. G. (2011). Numerical Modeling of Water Fluxes in the Root Zone of a Mature Pecan Orchard. *Soil Science Society of America Journal*, *75*(5), 1667–1680. https://doi.org/10.2136/SSSAJ2011.0086

Dimitrov, P., Kamenova, I., Roumenina, E., Filchev, L., Ilieva, I., Jelev, G., Gikov, A., Banov, M., Krasteva, V., Kolchakov, V., Kercheva, M., Dimitrov, E., & Miteva, N. (2019). Estimation of biophysical and biochemical variables of winter wheat through Sentinel-2 vegetation indices. *Bulgarian Journal of Agricultural Science*, *25*(5), 819–832.

Drusch, M., del Bello, U., Carlier, S., Colin, O., Fernandez, V., Gascon, F., Hoersch, B., Isola, C., Laberinti, P., Martimort, P., Meygret, A., Spoto, F., Sy, O., Marchese, F., & Bargellini, P. (2012). Sentinel-2: ESA's Optical High-Resolution Mission for GMES Operational Services. *Remote Sensing of Environment*, *120*, 25–36. https://doi.org/10.1016/J.RSE.2011.11.026

el Maayar, M., & Chen, J. M. (2006). Spatial scaling of evapotranspiration as affected by heterogeneities in vegetation, topography, and soil texture. *Remote Sensing of Environment*, *102*(1–2), 33–51. https://doi.org/10.1016/J.RSE.2006.01.017

Er-Raki, S., Chehbouni, A., Ezzahar, J., Khabba, S., Boulet, G., Hanich, L., & Williams, D. (2009). Evapotranspiration partitioning from sap flow and eddy covariance techniques for olive orchards in semi-arid region. *Acta Horticulturae*, *846*, 201–208. https://doi.org/10.17660/ACTAHORTIC.2009.846.21

Er-Raki, S., Profile, S., Chehbouni, A., Ezzahar, J., & Khabba, S. (2014). Evapotranspiration partitioning from sap flow and eddy covariance techniques for olive orchards in semi-arid region. *Acta Horticulturae* . https://doi.org/10.17660/ActaHortic.2009.846.21

Fang, B., Lei, H., Zhang, Y., Quan, Q., & Yang, D. (2020). Spatio-temporal patterns of evapotranspiration based on upscaling eddy covariance measurements in the dryland of the North China Plain. *Agricultural and Forest Meteorology*, *281*. https://doi.org/10.1016/j.agrformet.2019.107844

FAO. (2021). *AQUASTAT-FAO*. 2021. https://www.fao.org/aquastat/en/overview/methodology/water-use

Folhes, M. T., Rennó, C. D., & Soares, J. v. (2009). Remote sensing for irrigation water management in the semi-arid Northeast of Brazil. *Agricultural Water Management*, *96*(10), 1398–1408. https://doi.org/10.1016/J.AGWAT.2009.04.021

Glenn, E. P., Huete, A. R., Nagler, P. L., & Nelson, S. G. (2008). Relationship Between Remotely-sensed Vegetation Indices, Canopy Attributes and Plant Physiological Processes: What Vegetation Indices Can and Cannot Tell Us About the Landscape. *Sensors 2008, Vol. 8, Pages 2136-2160*, *8*(4), 2136–2160. https://doi.org/10.3390/S8042136

Gorelick, N., Hancher, M., Dixon, M., Ilyushchenko, S., Thau, D., & Moore, R. (2017). Google Earth Engine: Planetary-scale geospatial analysis for everyone. *Remote Sensing of Environment*, *202*, 18–27. https://doi.org/10.1016/J.RSE.2017.06.031

Hunsaker, D. J., Fitzgerald, G. J., French, A. N., Clarke, T. R., Ottman, M. J., & Jr., P. J. P. (2007). Wheat Irrigation Management Using Multispectral Crop Coefficients: I. Crop

Evapotranspiration Prediction. *Transactions of the ASABE*, *50*(6), 2017–2033. https://doi.org/10.13031/2013.24105

Hunsaker, D. J., Pinter, P. J., & Kimball, B. A. (2005). Wheat basal crop coefficients determined by normalized difference vegetation index. *Irrigation Science*, *24*(1), 1–14. https://doi.org/10.1007/S00271-005-0001-0/FIGURES/8

Ibraimo, N. A., Taylor, N. J., Steyn, J. M., Gush, M. B., & Annandale, J. G. (2016). Estimating water use of mature pecan orchards: A six stage crop growth curve approach. *Agricultural Water Management*, *177*, 359–368. https://doi.org/10.1016/J.AGWAT.2016.08.024

Jägermeyr, J., Gerten, D., Heinke, J., Schaphoff, S., Kummu, M., & Lucht, W. (2015). Water savings potentials of irrigation systems: global simulation of processes and linkages. *Hydrology and Earth System Sciences*, *19*(7), 3073–3091. https://doi.org/10.5194/hess-19-3073-2015

Jiménez, A. F., Cárdenas, P. F., & Jiménez, F. (2022). Intelligent IoT-multiagent precision irrigation approach for improving water use efficiency in irrigation systems at farm and district scales. *Computers and Electronics in Agriculture*, *192*, 106635. https://doi.org/10.1016/J.COMPAG.2021.106635

Jin, N., Ren, W., Tao, B., He, L., Ren, Q., Li, S., & Yu, Q. (2018). Effects of water stress on water use efficiency of irrigated and rainfed wheat in the Loess Plateau, China. *Science of The Total Environment*, *642*, 1–11. https://doi.org/10.1016/J.SCITOTENV.2018.06.028

Kang, S., Gu, B., Du, T., & Zhang, J. (2003). Crop coefficient and ratio of transpiration to evapotranspiration of winter wheat and maize in a semi-humid region. *Agricultural Water Management*, *59*(3), 239–254. https://doi.org/10.1016/S0378-3774(02)00150-6

Kerridge, B. L., Hornbuckle, J. W., Christen, E. W., & Faulkner, R. D. (2013). Using soil surface temperature to assess soil evaporation in a drip irrigated vineyard. *Agricultural Water Management*, *116*, 128–141. https://doi.org/10.1016/J.AGWAT.2012.07.001

Liu, G., Liu, Y., Hafeez, M., Xu, D., & Vote, C. (2012). Comparison of two methods to derive time series of actual evapotranspiration using eddy covariance measurements in the southeastern Australia. *Journal of Hydrology*, *454–455*, 1–6. https://doi.org/10.1016/J.JHYDROL.2012.05.011

Miyamoto, S. (1983). Consumptive Water Use of Irrigated Pecans. *Journal of the American Society for Horticultural Science*, *108*(5), 676–681.

Mokari, E., Samani, Z., Heerema, R., Dehghan-Niri, E., DuBois, D., Ward, F., & Pierce, C. (2022). Development of a new UAV-thermal imaging based model for estimating pecan evapotranspiration. *Computers and Electronics in Agriculture*, *194*, 106752. https://doi.org/10.1016/J.COMPAG.2022.106752

Mokari, E., Samani, Z., Heerema, R., & Ward, F. (2021). Evaluation of long-term climate change impact on the growing season and water use of mature pecan in Lower Rio Grande Valley. *Agricultural Water Management*, *252*, 106893. https://doi.org/10.1016/J.AGWAT.2021.106893

Montandon, L. M., & Small, E. E. (2008). The impact of soil reflectance on the quantification of the green vegetation fraction from NDVI. *Remote Sensing of Environment*, *112*(4), 1835–1845. https://doi.org/10.1016/j.rse.2007.09.007

Nagler, P. L., Scott, R. L., Westenburg, C., Cleverly, J. R., Glenn, E. P., & Huete, A. R. (2005). Evapotranspiration on western US rivers estimated using the Enhanced Vegetation Index from MODIS and data from eddy covariance and Bowen ratio flux towers. Remote Sensing of Environment, 97(3), 337–351.

Nagler, P. L., Morino, K., Murray, R. S., Osterberg, J., & Glenn, E. P. (2009). An empirical algorithm for estimating agricultural and riparian evapo- transpiration using MODIS enhanced vegetation index and ground measurements of ET. I. Description of method. Remote Sensing, 1, 1273–1297.

Nassar, A., Torres-Rua, A., Kustas, W., Nieto, H., McKee, M., Hipps, L., Stevens, D., Alfieri, J., Prueger, J., Alsina, M. M., McKee, L., Coopmans, C., Sanchez, L., & Dokoozlian, N. (2020). Influence of Model Grid Size on the Estimation of Surface Fluxes Using the Two Source Energy Balance Model and sUAS Imagery in Vineyards. *Remote Sensing 2020, Vol. 12, Page 342*, *12*(3), 342. https://doi.org/10.3390/RS12030342

Nazari, B., Liaghat, A., Akbari, M. R., & Keshavarz, M. (2018). Irrigation water management in Iran: Implications for water use efficiency improvement. *Agricultural Water Management*, *208*, 7–18. https://doi.org/10.1016/j.agwat.2018.06.003

Ortiz, A. C., & Jin, L. (2021). Chemical and hydrological controls on salt accumulation in irrigated soils of southwestern U.S. *Geoderma*, *391*. https://doi.org/10.1016/j.geoderma.2021.114976

Palmate, S. S., Kumar, S., Poulose, T., Ganjegunte, G. K., Chaganti, V. N., & Sheng, Z. (2022). Comparing the effect of different irrigation water scenarios on arid region pecan orchard using a system dynamics approach. *Agricultural Water Management*, *265*. https://doi.org/10.1016/j.agwat.2022.107547

Phogat, V., Šimůnek, J., Skewes, M. A., Cox, J. W., & McCarthy, M. G. (2016). Improving the estimation of evaporation by the FAO-56 dual crop coefficient approach under subsurface drip irrigation. *Agricultural Water Management*, *178*, 189–200. https://doi.org/10.1016/J.AGWAT.2016.09.022

Pôças, I., Calera, A., Campos, I., & Cunha, M. (2020). Remote sensing for estimating and mapping single and basal crop coefficientes: A review on spectral vegetation indices approaches. *Agricultural Water Management*, *233*, 106081. https://doi.org/10.1016/J.AGWAT.2020.106081

Qi, J., Marsett, R. C., Moran, M. S., Goodrich, D. C., Heilman, P., Kerr, Y. H., Dedieu, G., Chehbouni, A., & Zhang, X. X. (2000). Spatial and temporal dynamics of vegetation in the San Pedro River basin area. *Agricultural and Forest Meteorology*, *105*(1–3), 55–68. https://doi.org/10.1016/S0168-1923(00)00195-7

Reyes-González, A., Kjaersgaard, J., Trooien, T., Reta-Sánchez, D. G., Sánchez-Duarte, J. I., Preciado-Rangel, P., & Fortis-Hernández, M. (2019). Comparison of Leaf Area Index,

Surface Temperature, and Actual Evapotranspiration Estimated Using the METRIC Model and In Situ Measurements. *Sensors (Basel, Switzerland)*, *19*(8). https://doi.org/10.3390/S19081857

Roy, D. P., Wulder, M. A., Loveland, T. R., C.E., W., Allen, R. G., Anderson, M. C., Helder, D., Irons, J. R., Johnson, D. M., Kennedy, R., Scambos, T. A., Schaaf, C. B., Schott, J. R., Sheng, Y., Vermote, E. F., Belward, A. S., Bindschadler, R., Cohen, W. B., Gao, F., … Zhu, Z. (2014). Landsat-8: Science and product vision for terrestrial global change research. *Remote Sensing of Environment*, *145*, 154–172. https://doi.org/10.1016/J.RSE.2014.02.001

Sammis, T. W., Mexal, J. G., & Miller, D. (2004). Evapotranspiration of flood-irrigated pecans. *Agricultural Water Management*, *69*(3), 179–190. https://doi.org/10.1016/j.agwat.2004.05.005

Sánchez, J. M., López-Urrea, R., Valentín, F., Caselles, V., & Galve, J. M. (2019). Lysimeter assessment of the Simplified Two-Source Energy Balance model and eddy covariance system to estimate vineyard evapotranspiration. *Agricultural and Forest Meteorology*, *274*, 172–183. https://doi.org/10.1016/j.agrformet.2019.05.006

Sánchez, N., Martínez-Fernández, J., González-Piqueras, J., González-Dugo, M. P., Baroncini-Turrichia, G., Torres, E., Calera, A., & Pérez-Gutiérrez, C. (2012). Water balance at plot scale for soil moisture estimation using vegetation parameters. *Agricultural and Forest Meteorology*, *166–167*, 1–9. https://doi.org/10.1016/J.AGRFORMET.2012.07.005

Schüttemeyer, D., Schillings, C., Moene, A. F., & de Bruin, H. A. R. (2007). Satellite-Based Actual Evapotranspiration over Drying Semiarid Terrain in West Africa. *Journal of Applied Meteorology and Climatology*, *46*(1), 97–111. https://doi.org/10.1175/JAM2444.1

Sheng, Z., & Liu, Y. (2015). Evapotranspiration of flood-irrigated pecans under drought conditions in El Paso, TX. *Joint ASABE/IA Irrigation Symposium 2015: Emerging Technologies for Sustainable Irrigation*, 37–44. https://doi.org/10.13031/IRRIG.20152133782

Tenreiro, T. R., García-Vila, M., Gómez, J. A., Jiménez-Berni, J. A., & Fereres, E. (2021). Using NDVI for the assessment of canopy cover in agricultural crops within modelling research. *Computers and Electronics in Agriculture*, *182*, 106038. https://doi.org/10.1016/J.COMPAG.2021.106038

Wang, L., Liu, Z., Guo, J., Wang, Y., Ma, J., Yu, S., Yu, P., & Xu, L. (2021). Estimate canopy transpiration in larch plantations via the interactions among reference evapotranspiration, leaf area index, and soil moisture. *Forest Ecology and Management*, *481*, 118749. https://doi.org/10.1016/J.FORECO.2020.118749

Yu, L., Zhao, X., Gao, X., Jia, R., Yang, M., Yang, X., Wu, Y., & Siddique, K. H. M. (2021). Effect of natural factors and management practices on agricultural water use efficiency under drought: A meta-analysis of global drylands. *Journal of Hydrology*, *594*, 125977. https://doi.org/10.1016/J.JHYDROL.2021.125977

Chapter 5. Conclusion

Epilogue

In this thesis, a novel approach to partition evapotranspiration fluxes, adapted from the dual crop coefficient method and improved to provide daily values of the productive and unproductive water use of crops, was tested and applied in both annual and perennial crops of arid and semi-arid regions. The "Partitioning Evapotranspiration through Vegetation Indices" (*PETVI)* method can provide a viable alternative for estimating a crop's water-use trajectory during the growing cycle, yielding information on plants' water use in near-real-time (every 3 or 5 days). In combination with satellite-derived energy-balance-based ET_a, *PETVI* can produce images to detect when a crop's productive and unproductive water occurs. *PETVI* estimates of T_r and E_v showed good agreement in an annual crop, with those obtained through other methods using ground-based data, providing confidence in the method. *PETVI*'s proposed approach can aid in continuously monitoring evaporation (E_v) and transpiration (T_r) at different scales, depending on the spatial and temporal resolutions of the input variables, as exemplified with the use of high-resolution *UAV* imagery and moderate resolution (10m pixel) *S-2* scenes. The use of two different spatial resolutions (10m vs 5cm pixels) did not show significan differences between T_r estimates, although E_v did show larger values for lower-resolution data at the edges of the crop than those obtained with higher-resolution images.

The PETVI method was applied in corn fields of an intensive agricultural valley with an overexploited aquifer, to detect the productive and unproductive water use in plots equipped with three irrigation systems: furrow irrigated, sprinkler irrigated, and drip irrigated. We estimated the partitioning of productive and unproductive water and calculated the productive water use

efficiency as the ratio of transpiration over total water delivered in the plot. The results of the analyses obtained showed that the three irrigation systems had essentially the same water use efficiencies (varying < 4% among them). These low efficiencies are a result of deficient operation of the irrigation systems and well below the optimal efficiencies allowed by each system. A projection of the observed efficiencies at the basin scale, considering the areas cultivated and irrigated by each different system, indicated that by cutting the time intervals between pre-sowing irrigation events and sowing by 10 days, will relieve about ¼ of the total water usage in the basin in a year. That adjustment would decrease about 85.7% the excess water on the cultivated area and would be equivalent to close to 10 years of water usage by the people in the urban communities of the basin.

As exemplified previously, understanding productive and unproductive water and the periods in which it occurs allows us to identify water-saving alternatives under water scarcity and highly uncertain scenarios. In the third study case, the productive and unproductive water use in a pecan orchard with two soil textures, was evaluated. We found that the soil texture did have a large effect on the variability of the productive and unproductive water use of the trees. Moreover, and similar to observations in other sites, we found that most of the unproductive water use in the orchard occurs early in the season due to large irrigations for soil preparation for the following agricultural cycle. Applying the PETVI methodology to partition the ET_a fluxes using moderate spatial and temporal resolution (e.g.,10 m pixels and 3 to 5 days intervals between images) satellite data, we were able to estimate the productive and unproductive water use and its spatiotemporal variability within the orchard. Our estimates provide evidence that the soil texture induces changes in the dynamics of evaporation and transpiration due to their direct effect on tree growth and

canopy development during the growing cycle. Our analyses show that most of the unproductive water occurs in the irregular patches of fine-grained (i.e., clayr-rich) soil textures (PF) while in the areas with coarse-grained soils (PC) transpiration was a larger fraction of the total ET_a, and soil evaporation was considerably lower than in the PF soils. The cumulative unproductive water use after each irrigation period was larger in PF than in PC due to the low vegetation fraction within the PF area. Considering these findings, potential water savings to reduce the unproductive water use in the orchard can be obtained by reducing the irrigation amounts and or postponing irrigation to the beginning of the agricultural cycle (i.e., trees' resprouting) delivering the water close to the budbreak. Doing this has the additional advantage of reducing the salt concentrations from the evaporation of the first irrigation and reduced unproductive water in the early season.

Future work

To better understand the water balance dynamics at the plot scale, analyses made with PETVI can be complemented with field measurements of runoff, in the drainage channels of the plots using flumes equipped with pressure transducers to measure runoff at temporal high-frequency. Percolation of water past the root zone would also complement these analyses by providing a better estimate of the excess water from irrigation that does not become transferred into the atmosphere. This parameter can be monitored in the field using soil moisture sensors throughout the plot to detect the percolation patterns at different depths that exceed the root zone to detect the time and extent of percolation to better quantify irrigation water excesses. In areas with climatic conditions where crops are susceptible to hail damage, such as in the case of the Cuauhtémoc agricultural valley, where annual (corn fields) and a perennial crops (apple orchards)

grown are frequently hit by hail, farmers place anti-hail nets above the canopy of the trees to protect the crops. This represents a limitation for the PETVI method because the vegetation indices on which the method is based will yield erroneous data on vegetation activity due to the interference of the nets with the spectral reflectance of the canopies. This limitation, however, is not exclusive of satellite imagery, but also for high-resolution images obtained with UAVs since they will also capture an attenuated signal from the vegetation that will underestimate the K_{cb}. Therefore, this will produce lower values of T_r and an incorrect partition of the ET_a. Field observations with spectrometer data can be used to assess the effect of the hail mesh on the vegetation index, and a table with values for different types of nets and materials could be used to develop empirical coefficients to correct for those attenuations of the vegetation indices data.

Another potentially fruitful avenue of investigation with PETVI could be to assess the spatial and temporal T_r variability in response to vegetation stress. PETVI can provide near-daily T_r data, which can be combined with canopy temperature-derived indices of vegetation stress. In places like the pecan orchard in Tornillo, Texas, with shallow water tables, fluctuations in the levels of the shallow aquifer can be used to infer the water use by trees at sub-daily scale, which can indicate periods when trees can access groundwater. This information, together with field measurements of water balance that take percolation amounts into account, can shed light on the effects of shallow groundwater contribution to crop water use in arid riparian zones. Studies on soil evaporation using micro lysimeters in areas with different soil textures would also be advantageous to quantify E_v rates in the bare soil and soil under the shade of the canopy of trees. Additionally, to reduce the problem of edge effects in the estimation of T_r and E_v from using PETVI with moderate resolution scenes, high-resolution thermal and multispectral imagery from UAVs

can be complementary used; that high degree of detail that such information can produce will also allow to partition ET_a with sufficient definition to study changes in Tr at the tree canopy level for high precision agriculture.

PETVI has shown that it is able to capture the spatial variability of ET_a partitioning using remotely sensed imagery. However, to correctly estimate the required VIs and K_{cb}, expert evaluation of data quality needs to be performed to eliminate spurious data from clouds and shade effects. Automatization of these processes using machine learning algorithms that can detect and eliminate problematic data can help in processing large datasets for regional-scale analyses and reduce the need and cost of those analyses by reducing the time spent on visual verification by a person. Along this avenue of work, the implementation of the PETVI algorithm into application programming interfaces (APIs) using cloud computing and their evaluation and adoption by farmers and producers could open further areas of research on the use of these techniques to improve irrigation management at different scales (e.g. plot, districts and basins), and make this technology widely available to farmers and decision-makers in water irrigation districts.

Appendix

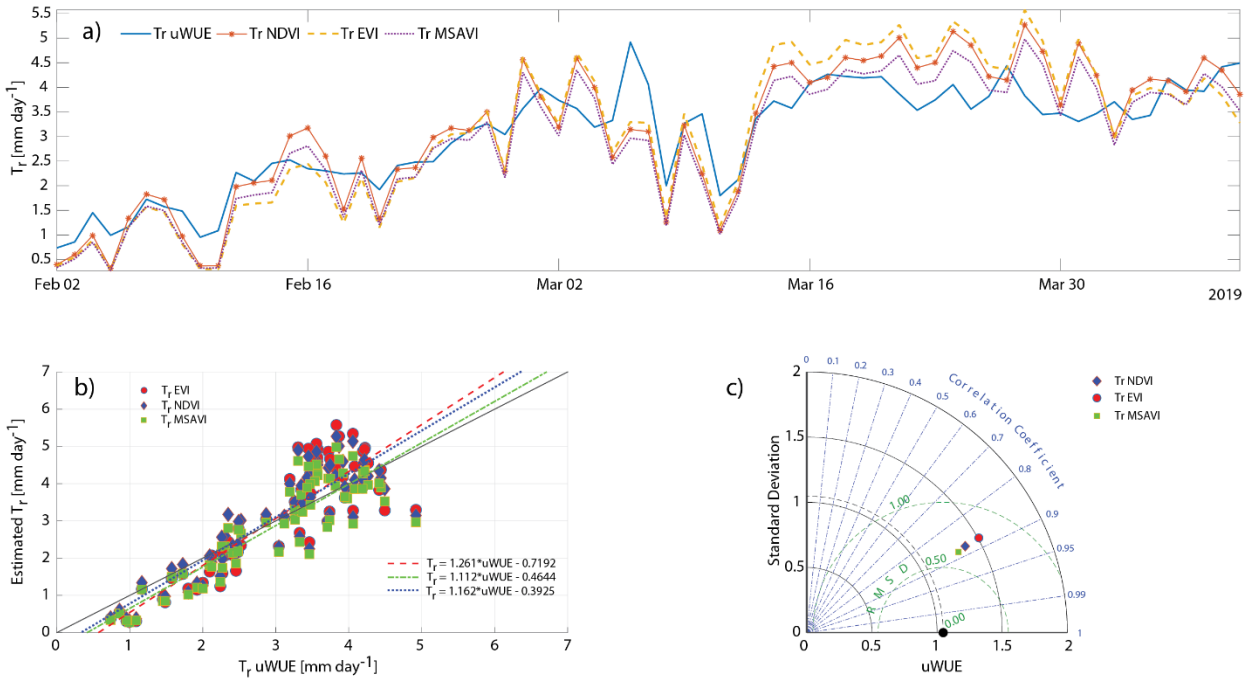

Figure 5.1 Transpiration (Tr) time series obtained with the underlying water use efficiency method (uWUE; blue line); red line represent the Tr calculated using NDVI, transpiration calculated using EVI, and the Tr using MSAVI; b) Scatter plot of the transpiration calculated with the uWUE method (x-axis) and $T_{r\ NDVI}$, $T_{r\ EVI}$ and $T_{r\ MSAVI}$ (y-axis); c) Taylor diagram displaying the correlation coefficient, standard deviation and root means square difference between the modeled transpirations ($T_{r\ NDVI}$ (blue diamond), $T_{r\ EVI}$ (red circle) and $T_{r\ MSAVI}$ (green square)) and the reference transpiration ($T_{r\ uWUE}$ (black circle)); green dashed lines represent the root mean square difference (RMSD) in mm.

Vita

Orlando Ramirez-Valle begun his academic formation completing a Bachelors in Engineering as an Agricultural Irrigation Engineer at the Universidad Autónoma Agrária Antonio Narro (2002-2006) in the state of Coahuila, Mexico, working with "Linear models for the evaluation of center pivot irrigation systems". He subsequently obtains a Master of Sciences degree in Natural Resources at the Sonoran Institute of Technology (2012-2014), with the Thesis work "Performance of the Irrigation Efficiency using Remote Sensing". From 2019 to November 2022, he was a Ph.D. candidate at the University of Texas at El Paso working on developing remote-sensing based methods to assess the water use efficiencies of irrigated croplands of arid and semiarid areas of northern Mexico and the U.S. southwest. His professional experience is related to irrigation scheduling, diagnosis of agricultural production, evaluation of irrigation systems and consumptive water use in croplands by means of field observations and remote sensing analyses.

Contact information: oramirezva@miners.utep.edu

ramirez.orlandoits@gmail.com